An EBSD study on mapping of small orientation differences in lattice mismatched heterostructures.

An EBSD Study on Mapping of Small Orientation Differences in Lattice Mismatched Heterostructures

by

Xiaodong Tao

Presented to the Graduate Research Committee
of Lehigh University
in Candidacy for the Degree of
Doctor of Philosophy

in

Materials Science and Engineering

Lehigh University

July 28, 2003

Certificate of Approval

Approved and recommended for acceptance as a dissertation in partial fulfillment of the requirements for the degree of Doctor of Philosophy

7/28/2003
Date

Dissertation Advisor

7/28/2003
Accepted Date

Committee Members:

Name of Committee Chair
Dr. J. A. Eades

Name of Committee Member
Dr. M. Treacy

Name of Committee Member
Dr. S. Cargill

Name of Committee Member
Dr. R. Pearson

Name of Committee Member
Dr. W. Misiolek

Acknowledgements

I would like to express my sincere gratitude to Dr. J.A.Eades for his guidance and support during my five years of study and research at Lehigh University. He showed me the wonder of electron diffraction (I thought it was just like clicking buttons, taking pictures and letting computer do the dummy indexing). It is a pleasure to work with a real gentleman. Thanks are due to Drs. Slade Cargill, Raymond Pearson, Wojtek Misiolek and Michael M.J.Treacy. I am fortunate to have them as my committee members.

I owe a lot to Dr. Slade Cargill's research group, especially Drs. Slade Cargill, Eva Campo and Alexey Nikiforov. In fact, I just walked into Dr. Slade Cargill's office directly and told him he should help me with samples since he is on my committee. He answered my request with a warm heart. His group provided me experimental samples and helped me with sample preparation as well as fruitful discussions. I also appreciate the help from Dr. Mark Wanlass of NIST for providing some of the test samples.

Special thanks are also due to Dr. Frederick Cosandey at Rutgers State University and Mr. David Von Rohr at Drexel University. Dr. Cosandey helped me to test the hydrocarbon contamination on their instruments and Mr. Von Rohr allowed me to test our "home made" software on their instrument and "babysat" me to very late at nights when I was doing experiment in his laboratory.

I am appreciative of the convenience provided by the people from TSL company (for allowing us to access their source code). Without their help, I would still be struggling with the software. Many thanks to the technical staff of Materials Science Department, like Willian Mushock, Arlan Benscotter, Dave Ackland, Mike Rex and Guy Faylor for all kinds of assistances, related and not directly related to this research.

Some fellow graduate students and Post-docs of Materials Science Department provided support during my studies here. Unfortunately some of them had left Lehigh University already and I couldn't thank them directly. These people include: Gang Chan, Rick Chromik, Gary Thompson and Chongming Wang.

I also would like to thank my parents for understanding, support and encouragement. Finally, special thanks to my wife, Chunyun Jiang, to whom I feel really guilty for all kinds of endurance she has to put up in the past five years.

Support from this research from DOE, under grant DE-FG02-00ER45819, is gratefully acknowledged.

Table of Contents

List of Figures

List of Tables

ABSTRACT

Electron back scatter diffraction (EBSD) on a Scanning Electron Microscope (SEM) has experienced rapid development in recent years. However, inadequate attention has been paid to the details of the method. Many of the algorithms in current use were chosen because they were the first ones that were found to work, not because they were optimum. The long term aim of this study is mainly concerned with extending EBSD to characterizing threading dislocations in semiconductor materials. In working toward this objective, a systematic study on the EBSD technique was performed.

The possibility of measuring small changes of orientation within grains by EBSD was explored. Conventional orientation maps (using EBSD) index the orientation of each position on the sample separately. This does not give accurate results for small differences of orientation. Therefore, methods of directly measuring small changes in orientation from one EBSD pattern to the others were examined. Previous workers have measured the change of position of zone axes in the EBSD pattern. A comparison between measuring changes of position of zone axes versus measuring the shift of the peaks in the Hough transform from one diffraction pattern to the next suggests that the latter method is superior. More over, it is possible, with a standard EBSD configuration, to measure the shift of the Kikuchi bands to a precision of about 0.1 pixels, which corresponds to a change of orientation of about 0.1 mrad. This method has been

successfully applied on a GaN/Sapphire structure. Based on this method, ways to perform high precision orientation mapping are proposed.

We have also shown that: 1) More than one method can successfully correct a sampling artifact, which is associated with the Hough transform; 2) There is an optimum binning ratio; 3) Gaussian filtering provides an alternative to "butterfly convolution"; 4) Better alternatives for mapping image quality than those in current use are available; 5) saving all the original patterns is practical and advantageous; And 6) Conventional usage of Monte-Carlo simulation for estimating the interaction volume of EBSD is flawed.

INTRODUCTION

"Epitaxially grown lattice mismatched heterostructures are of increasing importance for microelectronic and optoelectronic devices and circuits."[1] Examples of lattice mismatched heterostructures include blue-green lasers fabricated from II-VI semiconductors, and high electron mobility transistors made of III-V semiconductors [1]. With the in-plane lattice parameter matching that of the underlying material, the lattice mismatched layers are elastically strained in some structures, e.g., SiGe HBTs or III-V semiconductor lasers. When the strained layer exceeds a critical thickness, the strain is relieved by the introduction of the misfit dislocations. On the other hand, threading dislocations, which run perpendicular to the interface can also be generated as a by-product. Threading dislocations are harmful to the properties of the device since 1) the dislocations scatter the carriers and reduce mobility and 2) when the device is in use, scattering at the dislocations can generate additional defects, reducing the useful life of the device.

While it is easy to measure the mean density of misfit dislocations, it is not so easy to characterize the threading dislocations. Present methods include: Surface etching, TEM, EBIC and Atomic Force Microscopy (AFM). All of these techniques have inherent shortcomings, which severely limit their usage. For example, the specimen preparation process for TEM is tedious and destructive; the operation of TEM is complicated. Surface etching for optical microscopy is also destructive and the resolution ability is limited. The resolution of EBIC can only reach 1μ. NSOM (Near Field Scanning Optical

Microscopy) and SPM (scanning probe microscope) show great promise [3], but they still cannot characterize threading dislocations.

Scanning Electron Microscopy (SEM) is one of the most versatile materials characterization tools and nearly half of all new SEMs being bought directly or indirectly are used for semiconductor applications [4]. The typical usage of SEM includes superb image forming ability with either BSE (backscattered electrons) or SE (Secondary Electrons), fluorescence analysis, cathodoluminescence, magnetic contrast imaging, electron-beam induced current imaging (EBIC), voltage contrast imaging and electron diffraction. These techniques can be applied to bulk materials easily with little or no special specimen preparation required. Electron Back Scatter Diffraction (EBSD) is a SEM based diffraction technique. An EBSD pattern is often called EBSP, whose main features include criss-crossed Kikuchi bands overlaid on a noisy background. An EBSP has a reciprocal relationship with an Electron Channeling Pattern (ECP), which is another SEM based diffraction technique. ECP is the basis for Electron Channeling Contrast Imaging (ECCI), which can enable the imaging of near surface dislocations for bulk materials [5-8]. However, ECCI suffers from strict requirements on the electron optics.

The EBSD technique has gained wide attention in recent years and, until now, its main application is for texture analysis and phase identification. In this research, our main concern is to extend the functions of the EBSD technique and test the possibility of whether it can be used to characterize dislocations in bulk materials, especially the threading dislocations in the epitaxially grown lattice mismatched heterostructure semiconductors. We will approach this problem in two ways: 1) measuring the geometry shift of the Kikuchi bands and (or) Kikuchi zone axes to sub- pixel level and 2) monitoring the change of the intensity distribution of the Kikuchi bands, Kikuchi zone axes and even the whole patterns. This approach is easy to understand, since a single dislocation threading out of the surface of an epitaxially grown lattice mismatched heterostructure will bend some of the crystal planes near the surface. If the bent crystal planes are in the diffraction volume, it's very possible that the Kikuchi bands corresponding to these planes in the EBSD pattern will be shifted slightly, as shown in Figure 1.1. This shift is very small, at the scale of fractions of one pixel. Besides shifting the Kikuchi bands, the dislocation or its strain field can also change the intensity distribution in the diffraction pattern, especially the intensity distribution inside certain Kikuchi bands. As pointed out for ECP by Joy [5], the diffraction volume involves thousands of unit cells. And the effect of elastic deformation is averaged over thousands of superimposed slightly displaced patterns. So, the changing of the intensity distribution inside or around one to several bands contains information about the dislocation and its strain field.

Besides testing the possibility of imaging dislocations using EBSD, we also studied other practical issues related to improving present EBSD techniques.

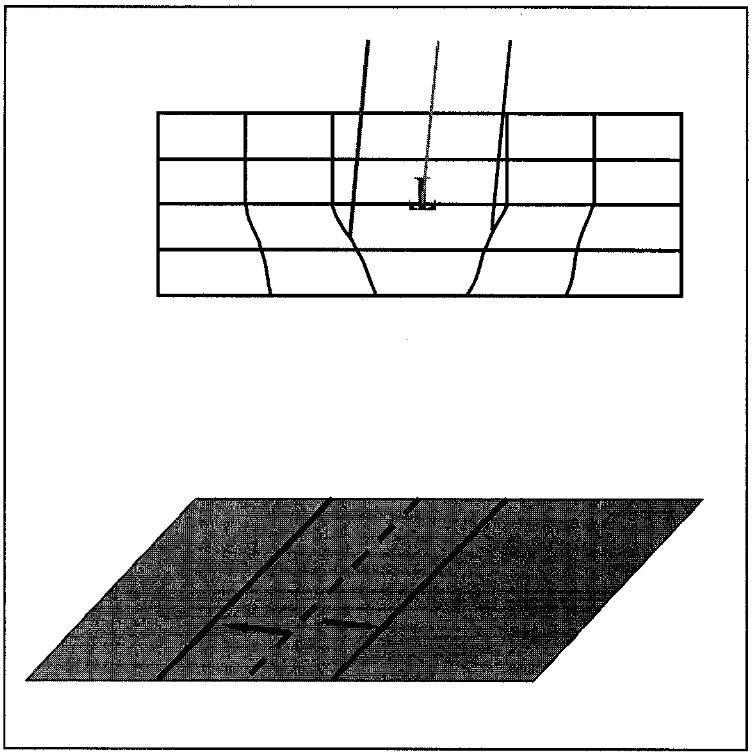

Figure 1.1. An edge dislocation is located at the center of this figure; the Kikuchi band is shifted because the dislocation bends the surrounding lattice.

2. BACKGROUND

2.1. OVERVIEW OF EBSD TECHNIQUE

2.1.1. Nomenclature and History

First invented by Alam and co-workers in 1954, further developed by Venables and co-workers in 1970's [9], the EBSD technique experienced rapid developments in both hardware and software in the past 10 years. An EBSD pattern is often called EBSP, (Electron Backscattering Pattern), Figure 2.1. EBSP is also known as BEKP (Backscattered Electron Kikuchi Patterns), and WAKP (Wide Angle Kikuchi Patterns). In some research, the term EBSD can be used interchangeably with EBSP.

Generally speaking, there were two kinds of commercial EBSD instruments emphasizing different application areas [10]. The first kind was mainly used for phase identification and usually chooses a slow scan peltier cooled CCD (charge coupled device) camera. In order to acquire a high quality pattern, the data acquisition time is usually long, at the scale of tens of seconds. Typical systems include: Noran's Phase ID and TSL's Delphi Phase ID system. In order to determine the phase of the sample, this kind of EBSD technique measures both the geometry relationship of the Kikuchi bands (relative angles) and the width of the Kikuchi bands. The second type is mostly used for orientation mapping. It detects the positions of the Kikuchi bands on the EBSD pattern and then uses their relative angles to index the orientation of the samples. This is the most common approach to materials analysis using the EBSD technique. For this kind of EBSD instrument, the electron beam is scanning across the surface of the sample at regularly spaced points; at each point an EBSD pattern is captured, indexed and the orientation and phase information is calculated and recorded in real time. The recorded orientation information (such as Euler angles and others) is later used to reconstruct the microstructure in the form of an orientation or a phase map [11]. Fully automated indexing of EBSD patterns became possible in the 1990's [9].

Usually, a low light SIT camera (Silicon Intensified Target) or CCD (charge coupled device) camera with short pattern acquisition time, at the scale of fractions of one second, has been used for this kind of system. TSL's OIM Data Collection system, Oxford's Opal, and HKL's Channel 5 systems are typical examples of this technique. With the wide usage of the on-chip integration CCD camera [12] to replace the low light SIT camera, the two different EBSD functions, Phase identification and orientation mapping, can be integrated into one EBSD system, at least at the hardware level. In addition, this new "on-chip" integration CCD camera (together with the Frame Grabber) allows the breakthrough of the limitation of the standard video format (30 frames every second). Through using a non-standard digital protocol, such as RS422 and LVDS, the EBSD mapping rates can be as high as more than 100 points per second [12]. Considering the fact that the light sensitive area on one CCD cell is small compared to the surrounding shift registers for an ordinary CCD camera and that a high signal-to-noise ratio is crucial for EBSD, another kind of CCD camera, the "Lens-on-chip" CCD camera which has much higher light sensitivity, could be a better alternative.

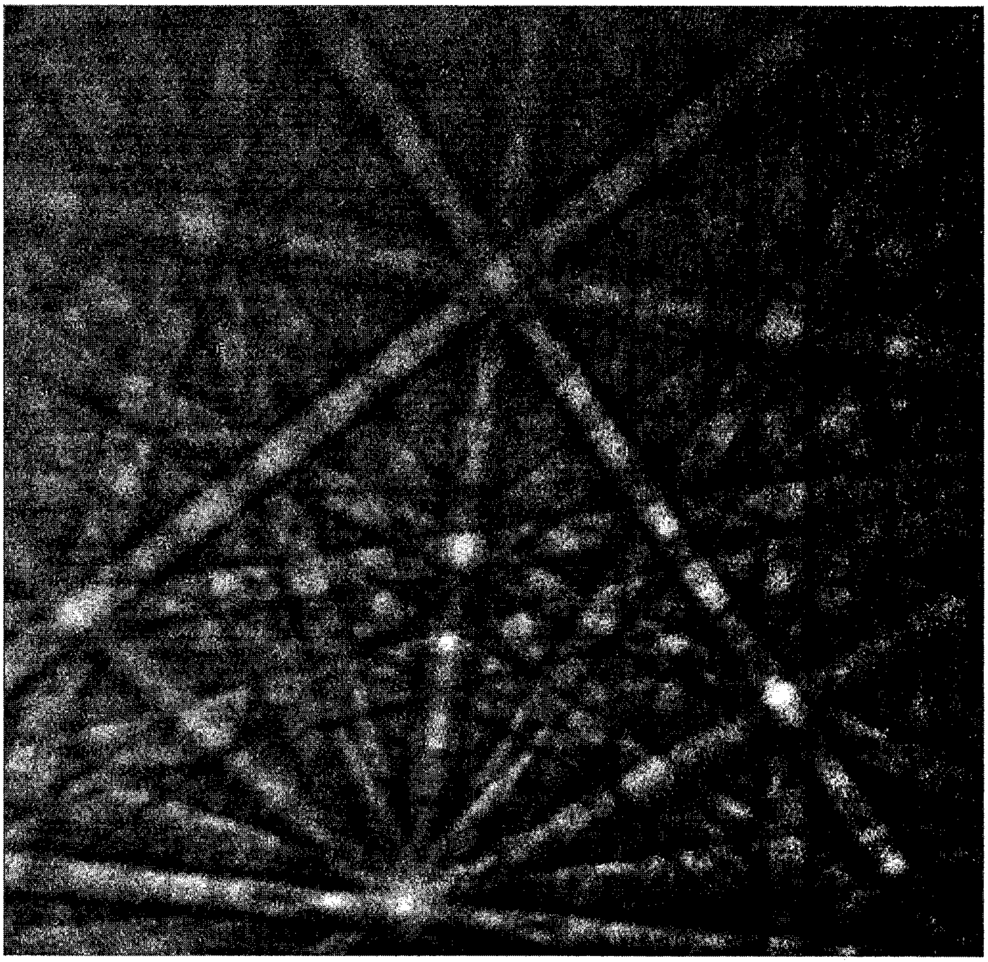

Figure 2.1 An EBSD pattern captured using Noran's Phase ID system, with background divided. 20 kV, 40s data collection time is used. The sample is an InAsP/InP heterostructure.

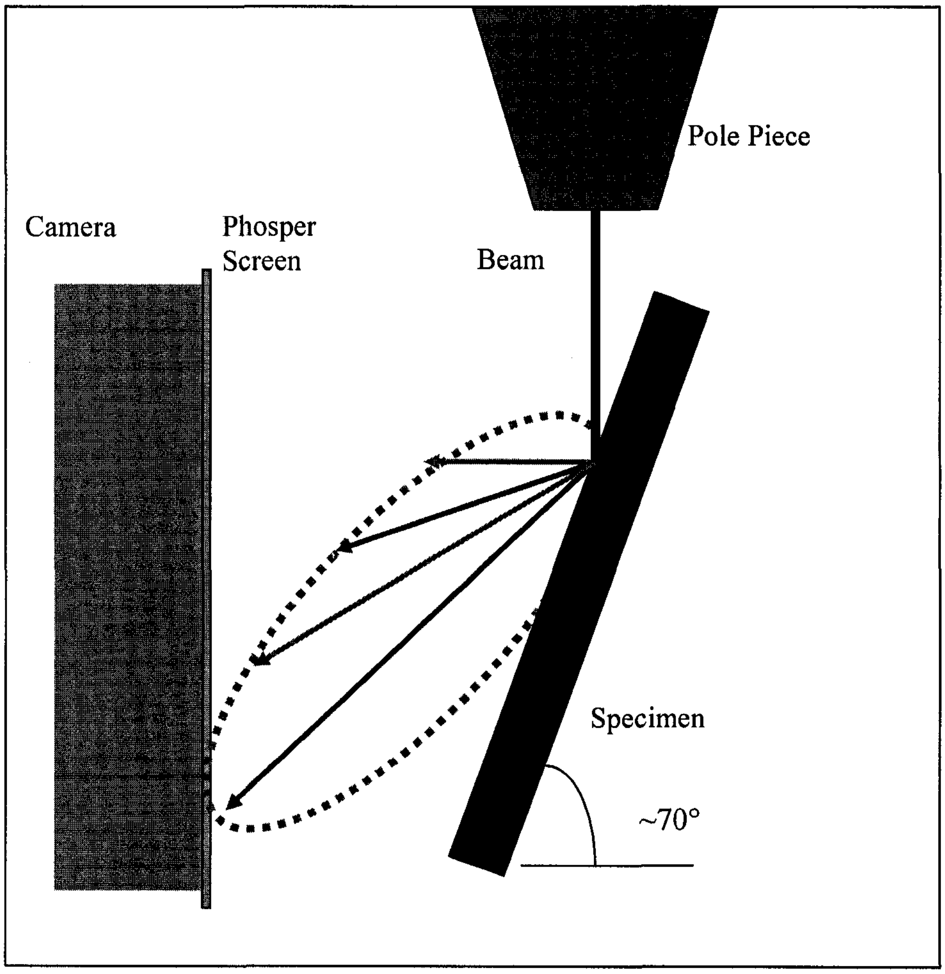

Figure 2.2. The principle and the configuration of the EBSD System. The asymmetrical spatial distribution of the BSEs, showed by the dotted line, causes the uneven background on the raw EBSD pattern.

2.1.2. Principle of EBSD

The working principle of the EBSD technique is quite simple and easy to understand, as illustrated in Figure 2.2. The focused electron beam from the SEM is held stationary on a highly tilted crystalline sample (typically 70 degrees) and the backscattered electrons are made to fall on a fluorescent screen that is observed by a low-light level camera, which is connected to a frame grabber (usually) on a personal computer (PC). To the first approximation, the Kikuchi bands, the main feature of an EBSD pattern, can be treated as the projection of the atomic planes to the phosphor screen directly and the width of the Kikuchi bands is inversely proportional to the corresponding d-spacing of the diffraction planes. Monte-Carlo simulation of the effect of a 20kV electron beam incident on 70 degree tilted Cu shows a divergent source of electrons within the specimen and scattered electrons will be traveling in all directions from this source [13]. So, the EBSD patterns are usually assumed to be formed by the elastic scattering of inelastically scattered electrons, like the Kikuchi bands observed in the TEM (Transmission Electron Microscopy). It is also believed that the low loss back scattered electrons (BSEs), or fast BSEs are mainly responsible for most features on the EBSD patterns and the low energy back scattered electrons (slow BSEs) mostly contribute to the background. Other features observed in the EBSD patterns, such as the High Order Laue Zone (HOLZ) rings are also observed in the convergent beam electron diffraction (CBED) patterns in TEM [14]. As will be covered in later chapters, EBSP has a reciprocal relationship with the ECP (Electron channeling pattern) - another SEM based diffraction technique. So, a thorough understanding of the EBSD phenomena should be put into the frame of dynamic electron diffraction theory and in the form of Bloch waves.

2.1.3. Spatial Resolution, Accuracy and Information Depth

"A spatial resolution of some 100nm (in the SEM) at an accuracy significantly better than 0.5° and about 1° can be routinely obtained for most materials and SEMs" [15]. It was also found that the best effective spatial resolution (60nm) for aluminum alloys in a tungsten-filament SEM was obtained for an intermediate probe current. "The field emission gun (FEG) SEM showed an improvement in spatial resolution by a factor of 2-3" [16]. According to Dingley [17], a lateral diameter of 22nm for a FEG and 50nm for a W filament SEM are the most optimistic estimation, since the specimen is highly tilted, the size of the vertical diameter is about three times of that of lateral diameter. These conclusions are based on the fact that, for a highly tilted sample, the backscattered electrons come from a large spatial range at the exit surface and thus this is assumed to be the determining factor which limits the spatial resolution of EBSD [18].

Some researchers [19, 20] scan electron beams across a grain boundary and acquire an EBSD map or several EBSD patterns from this area. Then, the distance that the overlapped patterns can be resolved by the software is measured and defined as the "spatial resolution". In this case, the measured spatial resolution tends to be very large on the scales of hundreds of nanometers even microns. We must point out the spatial resolution defined in this case has totally different physical meaning than in our research. The use of overlapped patterns relies on the indexing accuracy of the software. However, we are concerned with the small changes of the position of the Kikuchi bands (far less than 1°, for the measurement of the shift of Kikuchi bands) and the intensity distribution changes of BSE signals (for the monitoring of the intensity change).

It was found for a field-emission-gun SEM, the spatial resolution of EBSD improves with lowering the accelerating voltage and increasing the specimen atomic number [19]. Monte Carlo simulation of EBSD confirmed this conclusion [20].

The contrast of an EBSD pattern mainly comes from the low-loss back-scattered electrons, so a resolution depth far less than the depth of the interaction volume is expected. This resolution depth also depends on the atomic number of the sample. The larger the atomic number is the thinner the resolution depth is. Unfortunately, the resolution depth has never been experimentally determined [20]. Dingley [17] believed the diffraction information comes from a depth of 10nm, similar to that of low-loss BSEs image mode in conventional SEM [21], while some other researchers believe the signal comes from a depth of 20nm [22], similar to that of the information depth of the ECP (Electron channeling Pattern). The Monte Carlo simulation can only give a gross estimation that the information depth is less than 1μm [20].

The resolution and accuracy of EBSD technique depends on the choice of filament and the working conditions of SEM. Chemical composition, surface properties and other factors of the sample can strongly affect the experimental result. With the new emerging techniques, like in-lens thermal FEG SEM [23] which can emit even much more probe current than that of thermal FEG SEM, a better accuracy and spatial resolution can be expected.

2.1.4. Applications of EBSD

Nowadays, EBSD is a well-recognized and established technique. It is widely used to characterize metallurgy, ceramics and geology samples, and much effort is directed on extending its usage to semiconducting materials. Typically, the application of the EBSD technique can be categorized into following areas.

Orientation and Mis-orientation measurement:

Many materials have a preferred orientation after processing, which is also known as texture or fiber for geology samples [24]. Texture strongly affects the physical and mechanical properties of materials. EBSD can probe not only the proportions of each orientation component present in a specimen but also the distribution of these components in the microstructure [25]. Compared to X-ray diffraction, texture characterization using EBSD technique: 1) provides higher spatial resolution and 2) the measured texture information comes from a much thinner layer near the surface.

Phase Identification:

It is possible to identify the phase of a crystalline sample by measuring the angles between Kikuchi bands and the width of the Kikuchi bands. In principle, 27 of the 32 points groups can be distinguished if good quality EBSD patterns covering a sufficiently large solid angle can be obtained [26]. With the help of EDS, the process of Phase Identification can be greatly simplified. More over, Michael and Eades have suggested that the HOLZ rings, which are observed in some EBSD patterns, could also contribute to the identification of phases [14].

Grain size Measurement:

EBSD can be used to determine the true size of the grains and to characterize the grain boundaries. Traditional grain size measurement relies on etching of the sample and observation of grain boundaries in an image of the microstructure. In recent years, many studies have been carried out on using the diffraction contrast of the FIB (Focused Ion Beam) and digital image processing technique to measure grain sizes [27]. Unfortunately, some of the grain boundaries will not be revealed by these methods, especially for twins and low angle boundaries [25]. EBSD can not only give diffraction contrast between different grains (through IQ map or attached forward BSE detectors) but also provides automatic grain size measurement.

Determination of Local Strain:

For materials scientists and engineers, strain measurement is an important topic in both theory and practice. Reliable strain measurement proves to be a challenge for the EBSD technique.

Elastic Strain Measurement: The most direct way to measure the elastic strain is to measure the change of the width of the Kikuchi bands on the EBSD patterns, since Kikuchi bands are rigidly connected to the atomic planes. The precision of this method can only reach a few parts in 100 [28], since the Kikuchi bands of the EBSP are usually diffracted by low index planes and the edge of the Kikuchi bands are usually not very sharp on the EBSD patterns, and could extend to several pixels. Troost et al. were the first group to investigate the elastic strain in $Si_{1-x}Ge_x$ layers on Si(100) structures using EBSD technique and compared the result with X-ray methods [29]. By subtracting

EBSD patterns from single crystal Si from the EBSD patterns of a $Si_{1-x}Ge_x$ sample, the shift of certain Kikuchi zone axes in the EBSD pattern can be estimated and the accurate value is calculated using cross correlation. The strain level is then estimated from the shift of the Kikuchi bands. Wilkinson also investigated elastic strain in Si/SiGe structures using a similar approach [28]. The camera and phosphor screen were moved further out from the center of the stage, the distance between the camera and the sample is increased to 140 mm, about 4 times of that in a conventional EBSD configuration. Instead of measuring the shift of the Kikuchi bands, the shift of the zone axis is measured through calculating cross correlation functions. In this research, he claimed a strain sensitivity up to $\pm 2\times 10^{-4}$ [28] can be measured.

Plastic Strain Measurement. Plastic strain raises the dislocation density within the sample, and extensive local distortions of the lattice planes cause a reduction in the sharpness and contrast of the EBSD pattern [30]. Many efforts for quantifying the changing of the sharpness or 'Quality' of the EBSD patterns have been explored. Similar work has been previously done on ECP (Electron Channeling Patterns) [5]. An alternative approach to the problem of evaluating the residual plastic deformation was also proposed [31]. In this research, it is found that the density of low-angle misorientations correlates with plastic strain. Calibration curves relating misorientation density to known levels of strain in reference materials can subsequently be applied to estimate the levels of strain in samples.

2.1.5. Image Processing for EBSD Patterns

Procedures:

A raw EBSD pattern is often noisy and of inherently low contrast, especially for the fast scanning system that does orientation mapping (Figure 2.4), as a result of a low dose of probe current and a short pattern collection time. Also, the raw EBSD pattern tends to have an intensity-varying background as a result of the asymmetrical distribution of the backscattered electrons from a highly tilted sample (Figure 2.3). So, appropriate image processing procedures are usually a must before any meaningful indexing and measurement can be done. The overall image processing procedures for the fast scanning system is shown in simplified form in Figure 2.4 - Figure 2.9 [32, 33].

Through averaging over certain numbers of frames, the quality of the EBSD pattern can be enhanced greatly and the effect of the noise is alleviated effectively (Figure 2.5). Besides, a separate diffraction pattern is acquired over a large area for a polycrystalline sample by diffusing the electron beam. This pattern is an average over many grains, and reflects the asymmetrical distribution of the backscattered electrons but without noticeable crystal orientation information. Thus, it is used to approximate the background. This background is then divided or subtracted (depending on the choices of manufacturers) from the frame averaged EBSD patterns (Figure 2.6). Even though the quality of the EBSD pattern is improved evidently in this way, heavy noise on the EBSD pattern is not suppressed. By averaging the intensity over surrounding pixel blocks, say 5 $\times$ 5, we can get a much smaller image that is less noisy. This procedure is called binning

(Figure 2.7). Binning also decreases the calculation time needed for the following Hough transform [33-35], which is computing expensive.

The Hough transform has taken the place of the Burns algorithm [36] to become the standard band detection method in commercial EBSD systems. The Hough transform is simple, easy to implement and not sensitive to noise and missing parts of the signal. It is usually done on a circular area of the EBSD pattern for the convenience of displaying the Hough transformed image (Figure 2.7). Usually, the Hough peak tends to spread along the ρ direction (the vertical axis in Figure 2.8) and the spreading is proportional to the width of the Kikuchi band. Usually, the Hough peak has a "butterfly" shape on the raw Hough transform. In order to detect and enhance Hough peaks, the raw Hough transform is usually convoluted by a "butterfly mask" [33]. This step can also remove the uneven background on the raw Hough transform. Figure 2.8 is the raw Hough image of Figure 2.7. Figure 2.9 shows the result of convoluting a Hough image (Figure 2.7) with a 9×9 mask. After convolution, the software system starts to search for Hough peaks in the Hough space and further index the corresponding Kikuchi bands. The workflow of the band finding process is illustrated in Figure 2.11.

Introduction on Hough Transform

The principle of the Hough transform is illustrated in Figure 2.10. For EBSD patterns, the Hough transform changes linear features (Kikuchi bands) in the image space to bright or dark spots in the parameter space i.e. the Hough space. For the Hough transform, every pixel in the image space contributes to a *sinusoidal* curve in the Hough space. For example, points A , B, and C in Figure 2.10a correspond to curve a, b and c in Figure 2.10b separately. The intensity of this pixel will be added to all the points on the sinusoidal curve. All of the *sinusoidal* curves for one straight line have one common point in the Hough space and this common point in the Hough space is used to represent the straight line in the image space. Pseudo code for the Hough transform is listed in a Appendix 1. The intensity of one point in Hough space is the sum of the intensity of all the pixels on one straight line in image space.

The Hough transform of a Kikuchi band usually has the so-called butterfly shape after the convolution by the butterfly mask. Through Hough transformation, the problem of finding a linear feature in image space is changed to the problem of finding a peak in Hough space, which is quite simple for computer programming. A revised procedure based on the Hough transform for line detection has also been proposed and used. This method employs a special back mapping technique for generating two simplified Hough transforms, which separately focus on bright and dark lines in the images. This method is faster, more accurate and can provide accurate measurements of the location and width of typically 10-15 bands in a digitized EBSD pattern [37], while the ordinary Hough transform usually can find less than seven bands.

The Hough transform can also be treated as a special form of the Radon transform, which is widely used in computer tomography, such as CAT (computerized axial tomography, 1979 Nobel Prize).

Differences on Image Processing Procedures for the Two Systems

All the above procedures are done by a personal computer in fractions of a second with the exception of the background division, which is done by the hardware. For the phase identification system, the data processing speed is not the main concern compared with the needs of high accuracy in determining the d-spacing. As a result, their image processing procedures are slightly different: 1). Image binning for the Phase Identification system is not a necessary step anymore, since long pattern integration time is used and high accuracy on measuring d-spacing is required. 2). The sampling interval for the Hough transform is smaller for the Phase identification system, since calculation time is not a big concern here. 3). Software background subtraction is sometimes used for Phase Identification. This is also known as software flat fielding in some systems. On the source code level, this is equal to subtracting a large radius Gaussian blurred pattern. 4). Phase Identification systems must use appropriate algorithm(s) to determine the width of the Kikuchi bands.

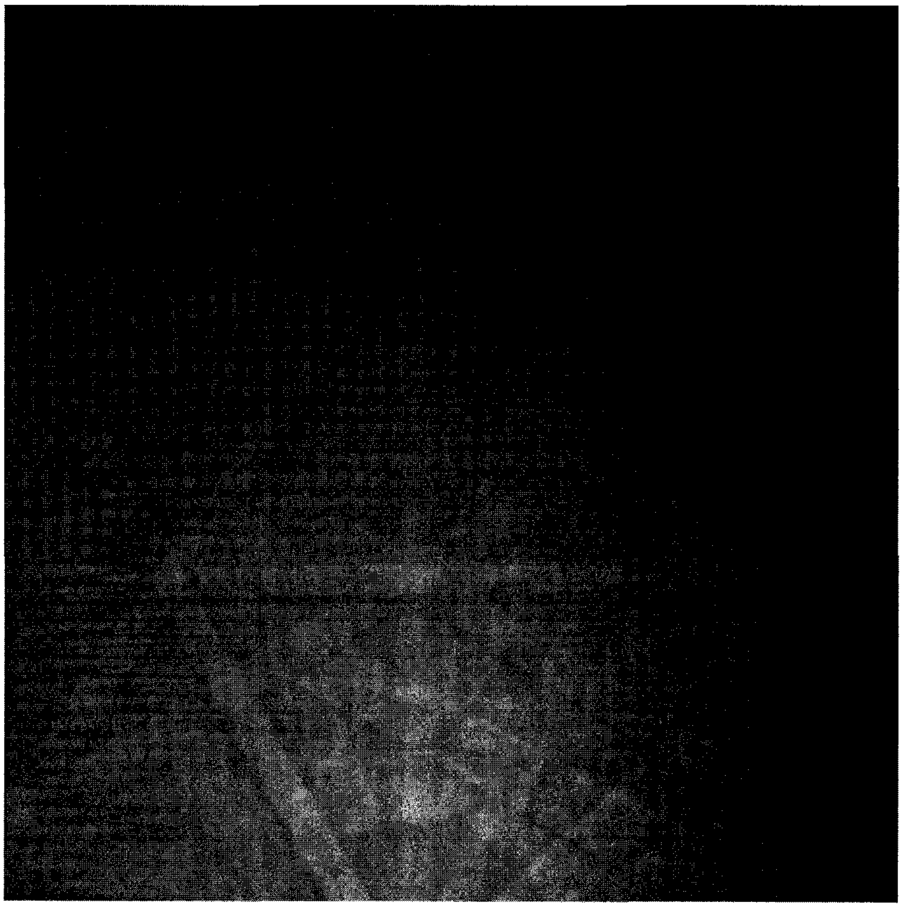

Figure 2.3. A raw EBSD pattern captured using Noran's Phase ID system, with background not corrected. 20 kV, 40s data collection time was used. The sample is a silicon wafer. The uneven background is caused by the asymmetrical distribution of the BSEs.

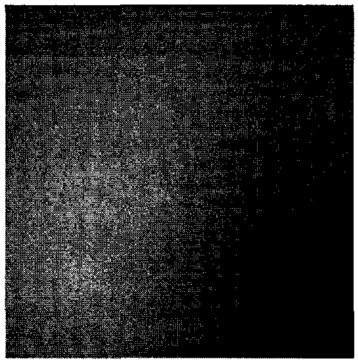

Figure 2. 4. A Single Frame Raw EBSD pattern.

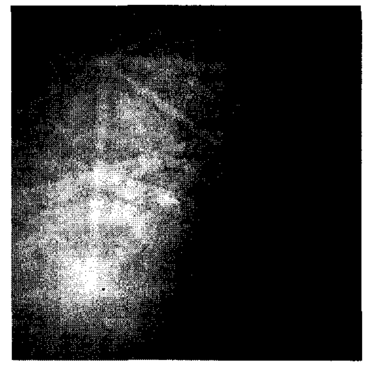

Figure 2.5. An EBSD pattern averaged over 128 Frames.

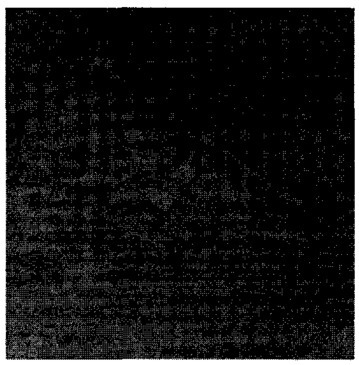

Figure 2.6. Figure 2.5 with background subtracted.

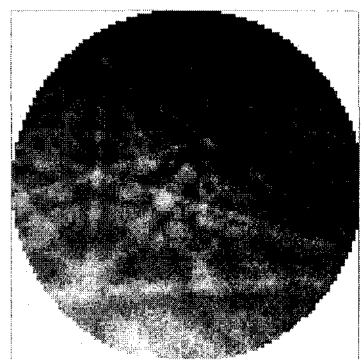

Figure 2.7. Binning figure 2.6 to a circular area. The binning ratio is 5:1.

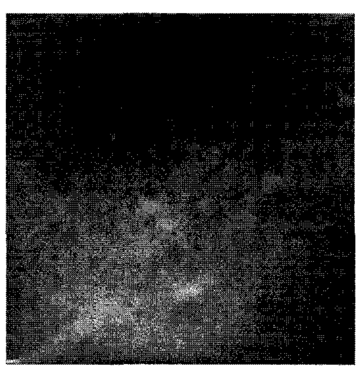

Figure 2.8. Raw Hough Transform of Figure 2.7.

Figure 2.9. Convoluting figure 2.8 with a butterfly. mask

Figures 2.4- 2.9 are adapted from the manual of OIM Data Collection software (TSL company) [32]

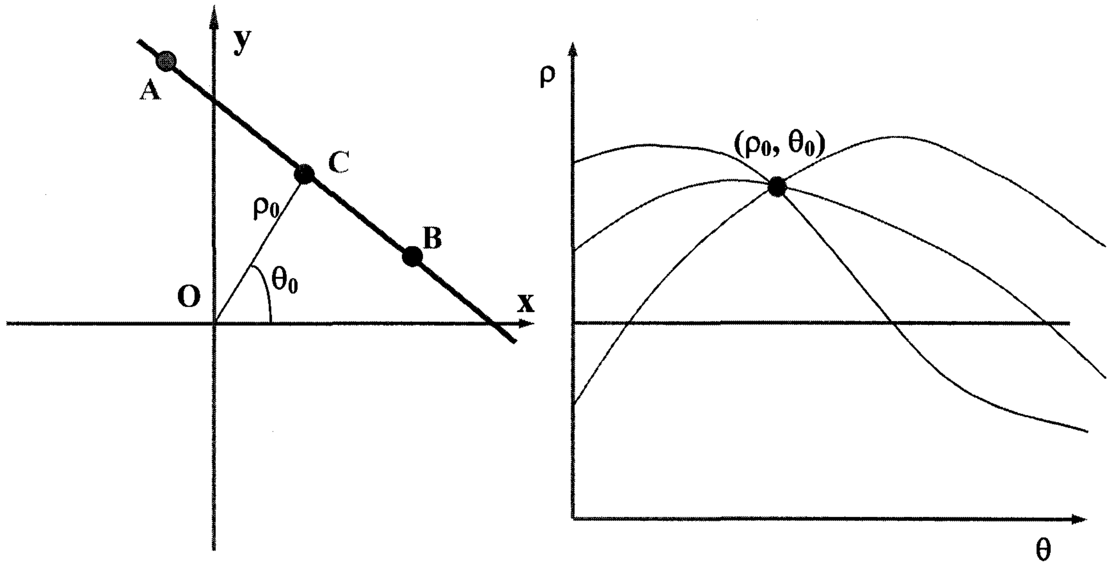

Image Space Figure 2.10a Hough Space Figure 2.10b

Figure 2.10. Principle of Hough Transform. Each point in the image space corresponds to one sinusoidal curve in the Hough Space, and the crossing point of the three curves in Hough Space (Figure 2.10b) represents the line AB in image Space (Figure 2.10a).

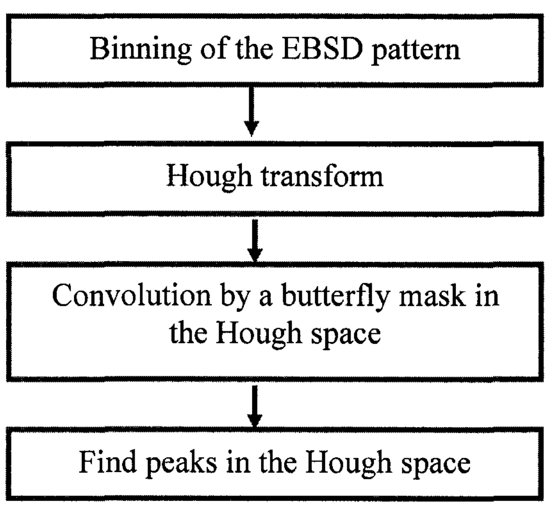

Figure 2.11. Illustration of the procedure to find Kikuchi bands for EBSD.

2.1.6. Pattern Indexing and Data Display

Indexing

In order to determine an orientation, two coordinate systems are necessary. For EBSD, one is the specimen coordinate system (S), defining the rolling direction (RD), the normal direction (ND) and the transverse direction (TD). The other coordinate system, the crystal coordinate system (C) is determined by the directions of the crystal. After these two references frames are built, a rotation matrix can be easily determined, relating the crystal orientation to the specimen coordinate. This can be written as Cc = **g**.Cs. This concept is most useful when understanding the pole figures and inverse pole figures [38].

Automatic indexing of the EBSD patterns is also implemented through matrix rotation. Usually, after three Kikuchi bands are found in Hough space, the angles between every triplet of Kikuchi bands are measured and used to compare with a look-up table, which contains pre-calculated angles between all possible bands. Then the system begins to find the best fits. Thus, this triplet is indexed. After at least two bands (not parallel to each other) are indexed and the pattern center (PC) is known, the orientation of the corresponding index of other Kikuchi bands and zone axis can be calculated using following steps. First, two coordinate systems are built. The first one is based on the position of the Kikuchi bands on the camera and the other one is based on the absolute crystal orientation of the sample. After the orientation coordinate system is defined their rotation matrix is determined, the automatic indexing can be fully implemented [39].

EBSD Data collection software calculates and records the three euler angles in real time from the indexing results of the EBSD patterns for each sampling point. Then the recorded Euler angles are later used to reconstruct the orientation maps, figures and charts. Among them, inverse pole figure, inverse pole figure map, pole figure, IQ (Image Quality) map, and the CI parameter are usually used and briefly explained below.

An inverse pole figure is usually plotted on a unit triangle. It shows the position of a sample direction relative to the crystal reference system. Drawing an inverse pole figure involves two coordinate systems, the orientation coordinate of the crystal and the coordinate of the sample axes (RD, TD and ND). Usually users are prompted to input a specific sample direction [uvw] to consider, the analysis software will generate an inverse pole figure, which shows the orientation of all the sampling points when they are aligned with the [uvw] direction of the reference system [24, 32]. The inverse pole figure map is a pseudo color map. First, three different colors are assigned to the three vertices of the unit triangle. Later, each point of the unit triangle is assigned a different color according to its distance to the three vertices. The color of each pixel in the inverse pole figure map is chosen in this unit triangle according to its orientation.

Pole Figures show the stereographic projection of the poles of the chosen family of planes. These planes are displayed with respect to the Rolling and Transverse directions on the sample. The sample 'normal' direction is represented by the center of the pole figure. Grain orientation data can, therefore, be plotted in terms of sample direction. This type of diagram can indicate whether there is preferred crystallographic orientation present [40].

IQ (image quality) for TSL's OIM system or PQ (pattern quality) for some other commercial systems is used to express the diffuseness of an EBSD pattern. It measures the sharpness of the Kikuchi band edges and thus it is sensitive to the strain level, grain boundary, and scratches on the surface to some extent. Mathematically, it is expressed as the average of the height of the peaks subtracting the height of the valleys for detected bands in the Hough space. The IQ map uses the intensity information from the EBSD pattern indirectly. It avoids the "voting process" for the indexing procedure and possibly could lead to better resolution than the map of inverse pole figure in some research.

CI (confidence index) is a parameter defined by TSL. It is calculated during the automatic indexing of the EBSD patterns. For one pattern, there could be several orientation choices caused by the noise, false peaks, and tolerance angle. TSL's Data Collection system ranks these orientation choices using a voting scheme. The confidence index is defined as $CI = (V_1-V_2)/V_{Total}$. V_1-V_2 are the votes for the first and the second choices and V_{Total} is the total votes number. The value of CI ranges from 0 to 1, the larger the better [40].

Post Filtering (Filtering for data display)

When EBSD is used to measure the grain size, the measurement could be affected by the "bad indexed points" in some conditions - Some patterns that are not correctly indexed being caused by the defects on the sample, fluctuation of the probe current, effect of noise etc. Some bad indexed points are isolated and much smaller than normal grain size. As a result, the software falsely believes those areas are small grains. Median filters can be used to overcome this factor. A median filter is a kind of non-linear filter; it tends to conserve the edge of an image but filter out those areas which are less than the half of the area of the filter.

Research on using the Kuwahara filter, a special form of median filter, to filter the orientation map shows positive results [41]. However, careful attention should be made on choosing appropriate mask size. Besides, the calculation time for using median filters is usually slower than using a linear filter.

2.1.7. EBSP .VS. ECP

Electron channeling patterns (ECP) record the changes in the BSE (or secondary electron) intensity that occurs as the parallel electron beam is rocked through a range of incident angles relative to the crystal planes in the sample [30]. ECP and EBSP are related by the theorem of reciprocity [42]; Figure 2.12 shows the geometry of the relationship between them [42].

Overview of channeling related technology

Electron channeling patterns were first observed by Coates [43], and qualitatively explained by Booker et al. using dynamic electron diffraction theory and Bloch waves [44]. For two beam conditions, when a high energy parallel electron beam is incident on a crystal and the beam is near the Bragg reflecting position, the electrons inside the crystal can be considered as the superposition of two Bloch waves. The type 1 wave has antinodes located at the atoms of the reflecting planes, and the type 2 wave has the antinodes located between the atoms of the reflecting planes. If the beam is exactly on the Bragg condition ($\theta = \theta_B$), two Bloch waves are excited equally. If s, the deviation parameter, is slightly negative ($\theta < \theta_B$), the type 1 wave is preferentially excited, the total backscattered electron intensity will be large, while if s is slightly positive ($\theta > \theta_B$), the type 2 wave is preferentially excited, and the total backscattered electron intensity will be small. Consequently, we get bright bands bordered by dark lines superimposed on the noisy background.

Besides using electron channeling patterns directly, channeling contrast can also be utilized to image the specimen. This technique is named ECI or ECCI (Electron Channeling Contrast Imaging). With appropriate settings, the SEM can be used to image and characterize near surface defects such as dislocations and twins in bulk specimens using the ECCI technique. Since the defects distort the surrounding lattice orientation and this distortion causes a small difference in the absorption of Bloch waves, the back scattering coefficient (η) is changed slightly. If using a FEG (Field Emission Gun) SEM, characterizing single dislocations near the surface of bulk specimens is possible [5-7]. Groups of dislocations found relatively far below the surface can be imaged using thermionic emitters, which could provide high beam currents compared to cold FEGs [45].

The beam rocking method has been most often used to generate ECPs [5]. The diffraction volume is limited by the rocking angle and the spherical aberration coefficient of the objective lens. Usually, the diameter for the selected area can be up to tens of micrometers. Some calculations indicate that the channeling signals generated using

20kV electrons originate within the first 100nm of material, the majority part coming from the upper 50nm [46]. In order to image individual defects close to the surface of a crystal, it is necessary to use a small beam diameter (<10nm), a small beam divergence (<10mrad) and a high beam current (>1nA) [30].

The ECCI technique is still being used for characterizing bulk semiconductor materials and dislocation structures in deformed metals [8, 30].

Similarity and Differences Between EBSP and ECP

Even though EBSP and ECP are similar in some aspects, such as the pattern features (Kikuchi bands) and principles, they are quite different in many areas.

Spatial resolution: The spatial resolution of EBSP is better than that of ECP. In ECP, the minimum selected size is usually several micrometers while the estimated spatial resolution for EBSD can reach tens of nm for an FEG SEM, even though the exact value is still unknown.

Configuration: The EBSD sample is usually highly tilted (~70 degrees) and a video camera is used to capture the diffraction pattern. However, an ECP is usually acquired when the sample is only slightly tilted and no video camera is needed. In order to get an ECP, the beam must rock about one point on the specimen; to get an EBSD pattern, the beam stays stationary. Besides, ECP needs a small objective aperture in order to get a nearly parallel beam, and the EBSP needs a large objective aperture in order to get a large probe current and in-coherency.

Information: Usually, an EBSP pattern contains Kikuchi bands formed by low index atomic planes, while an ECP pattern also contains Kikuchi bands formed by relatively high index atomic planes [30]. Typically, an ECP is limited to an angular width of 6° to 10° in the stereographic triangle, while EBSPs may cover an angular width as wide as 60°. The wider "field of view" means that the identification of crystallographic orientation is relatively easier for EBSP comparing to ECP [46].

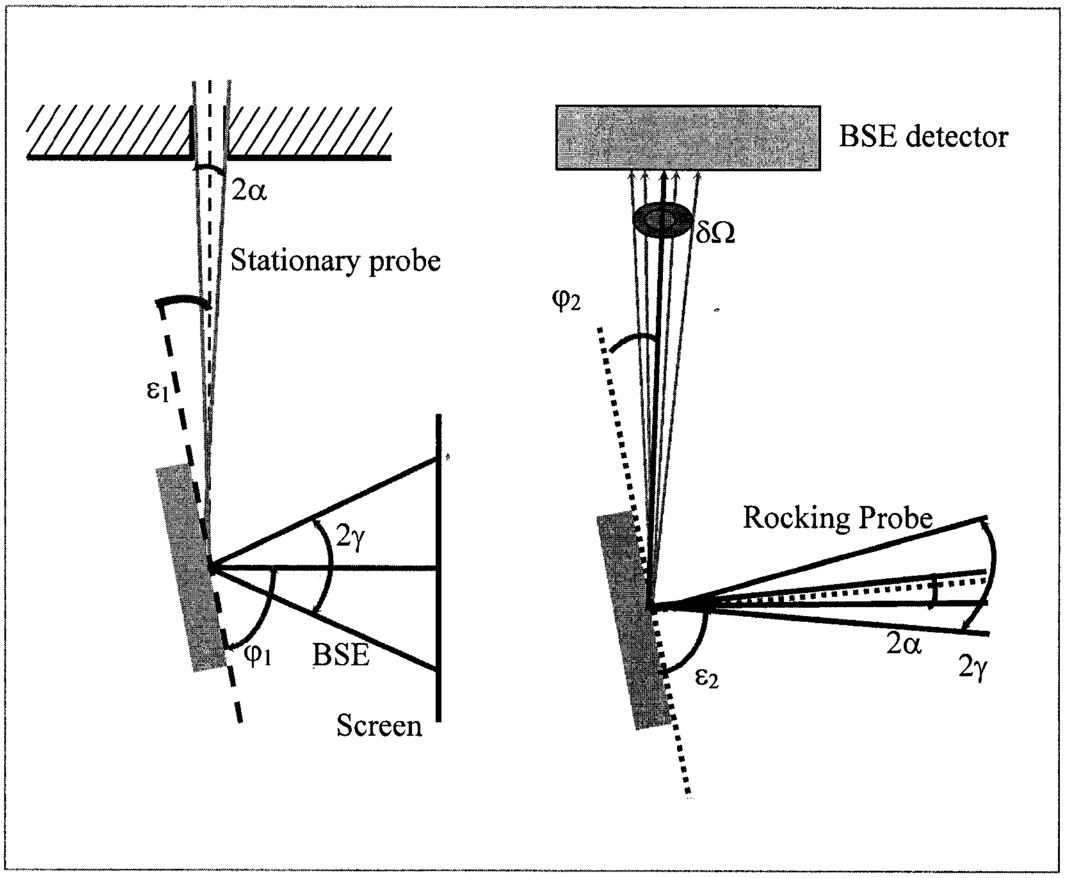

Figure 2.12. Illustration of the Reciprocal relationship between ECP and EBSP.

2.2. IMAGE MATCHING TECHNIQUE

Detecting the shift of a digital image or certain features in a series of images is an important and well studied topic [47]. A wide variety of methods can be found in the literature to solve this fundamental problem. This kind of problem is often called image matching, image registering or template matching. The matching problem is also referred as the correspondence problem and it is not only limited to images, the dataset can also represent other things like, maps, texts and even multi-dimension objects. Image matching is well known as an ill-conditioned problem, since ambiguous solutions may occur. This kind of problem is usually computing intensive.

Among all of the methods, cross correlation (or cross correlation coefficient) and phase correlation [48, 49, 50] are conventionally used as criteria for image registration. With the usage of appropriate interpolating schemes, both of them can reach an accuracy of sub-pixel.

2.2.1. Cross Correlation Coefficient

The cross correlation coefficient, equation 2.1, and cross correlation, equation 2.2, are the most commonly used criteria for image matching. The physical meanings of cross correlation and cross correlation coefficient are shown in Figure 2.13.

The definition of the cross correlation coefficient can be found in any statistics book. It can be understood as the normalized cross correlation; it can eliminate the effect of the background and the effect of the gain to some extent. Its value ranges from –1 to 1. The larger the value, the better the match. The cross correlation coefficient can be calculated directly or indirectly (through a Fourier transform). The direct method is fast for small sets of data (equation 2.1), while the Fourier method is more effective if the dataset is large (equation 2.2). Besides, the Fourier method assumes the image repeats itself indefinitely.

$$r(x,y) = \frac{\sum_{i,j}\{[f(i,j)-\overline{f}(i,j)]\times[g(i-x,j-y)-\overline{g}(i-x,j-y)]\}}{\sqrt{\sum_{i,j}[f(i,j)-\overline{f}(i,j)]^2}\sqrt{\sum_{i,j}[g(i-x,j-y)-\overline{g}(i-x,j-y)]^2}} \qquad 2.1)$$

f(i,j) is one image (represented by the solid frame in Figure 2.13a) and g(i,j) is the other image (represented by open rectangle in Figure 2.13b). x ,y is the relative displacement of the two images. $\overline{f}(i,j)$ and $\overline{g}(i-x,j-y)$ are the mean values over the solid rectangles in Figure 2.13a) and Figure 2.13b). The core idea is that the two images are displaced, step-by-step, with respect to each other. For each step, r(x,y) is evaluated. The best fit of the patterns occurs when r(x,y) takes its maximum value.

The cross correlation can be shown to be:

$$R(x,y) = F^{-1}\{F^*(u,v).G(u,v)\} \qquad 2.2)$$

$F^*(u,v)$ is the conjugate of the Fourier transform of f(i,j), G(u,v) is the Fourier transform of g(i,j) and $F^{-1}\{\}$ stands for the inverse Fourier transform. This result is related to the convolution theorem.

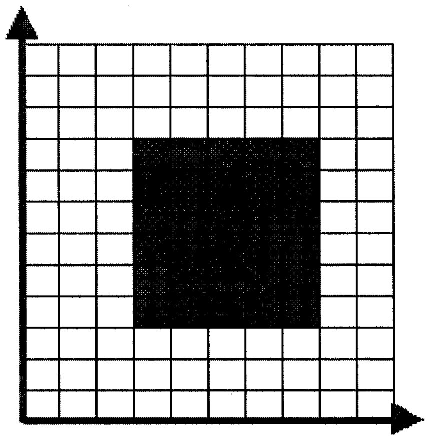

Figure 2.13a. The solid square stands for the template window f(x,y).

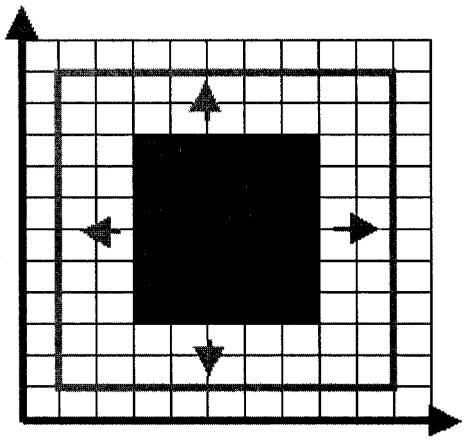

Figure 2.13b. The solid square is g(x,y).

Figure 2.13. Illustration of the process of template window fitting. The solid rectangle in Figure 2.13b has the same size as that in Figure 2.13a and it is moved one pixel by one pixel inside the open square in Figure 2.13b. At each position, the cross correlation coefficient is calculated. The larger the value, the better the match.

With the Fourier transform, if careful attention is paid to normalizing the Fourier transform coefficient, the cross correlation R(x,y) is normalized to match the cross correlation coefficient, r(x,y).

If choosing to calculate the cross correlation coefficient directly, the template window ***f(i,j)*** and image ***g(i,j)*** in the equation have exactly the same sizes . However, we must also provide some margin on the target images, (the outer frame in the Figure 2.13b). If choosing to calculate Cross Correlation Coefficient using the Fourier transform, the ***f(i,j)*** and ***g(i,j)*** must have exactly the same size and no margin is needed. However, the Fourier transform method assumes the ***g(i,j)*** repeats itself indefinitely at the edges.

2.2.2. Phase Correlation:

Phase correlation uses the shift property of the Fourier transform; that is a shift in the spatial domain is equivalent to a phase shift in the frequency domain.

Let, f2(x, y) = f1(x-xo, y-yo) 2.3)

The Fourier transform of f2(x,y) and f1(x,y) has following relationship:

F2(u, v) = F1(u, v) exp(-i (uxo + vyo)) 2.4)

Rearranging the components, we get:

$$\frac{F_2(u,v).F_1(u,v)^*}{|F_1(u,v).F_1(u.v)^*|} = \exp(-i(ux_0 + vy_0)) \qquad 2.5)$$

The right side of the equation 2.5) is the normalized cross power spectrum:

$F_1(u,v)^*$ is the complex conjugate of function $F_1(u,v)$.

Doing an inverse Fourier transform on equation 2.5, the right part of the equation becomes a Dirac Delta function centered at (x0, y0), i.e. $\delta(x-xo, y-yo)$.

In this way, the shifting distance (x0, y0) can be easily determined. The phase correlation method is notably robust to noise and other false effects and it provides a distinct sharp peak at the point of registration whereas the standard cross correlation yields broad peaks [49]. However, equation 2.5 is valid only if the shift vector (xo, yo) is of integer values in the discrete case. Research in recent years shows that phase correlation algorithm can be extended to sub-pixel resolution effectively [49, 50]. Experiments show the accuracy for artificial images with heavy noise using this method can reach 1/20th pixels [49, 50] with no difficulty.

3. NUMERICAL METHODS AND EXPERIMENT

3.1. OUTLINE

For this research, the TSL OIM Data Collection software was modified. In its standard form, at each point the captured EBSD pattern is indexed and only the orientation data is stored. With our modification, it is also possible to store the complete EBSD pattern for each pixel. In this way, the same complete data set for a scan could be analyzed (off-line, after the scan) by several different procedures, for comparison of the methods. In theory, all of the methods we used in this research can also be implemented in real time, however, due to the consideration of the calculation time and comparison of different methods, storing all of the patterns for offline analysis seems a better choice. Besides revising the TSL Data Collection system in several ways, we also wrote several stand-alone Win32 GUI programs to test different experimental methods. A special computer file format (.dan) is also defined for all those offline mapping processes, since the standard image formats lack flexibility. This generated map file (.dan) can be tweaked and converted to a .bmp (Bitmap) file using a program **DataAnalyzer** written for this research. A complete explanation of all the written programs, changes made on the OIM Data Collection software and the data structure of the mapping file format (.dan) are listed in Appendix 3.

One major task of this research is to measure and further map the shift of the Kikuchi bands (or zone axes) as accurately as possible. In order to image a single dislocation, a precision up to sub-pixel is necessary. We choose to measure the shift of the bands in the Hough space and the shift of the zone axes in image space. The latter, measuring the shift of the zone axes in image space, is similar to the method used by Wilkinson on measuring elastic strains [28, 30]. In our research, mapping of the shift in both Hough space and image space is also available (offline scan).

To achieve the goal of measuring and mapping the shift of Kikuchi bands in Hough space accurately, we looked into the algorithm for the Hough transform and found that the standard Hough transform will inevitably introduce artifacts. The origin of the artifacts and two remedies to remove them are given in the next chapter. One of the remedies is mainly used for the measuring the shift of the Kikuchi bands in Hough space, the other method is designed to replace the standard Hough transform used in OIM.

Besides shifting Kikuchi bands, dislocations and near surface defects can cause the blurring of certain Kikuchi bands, or the whole EBSD patterns. So, our second task is to map the changing of the intensity distribution of the EBSD patterns.

From another point of view, both measuring the shift of the Kikuchi bands and mapping the intensity changing of certain Kikuchi bands can be thought as "reciprocal operations" of ECCI (electron channeling contrast imaging). However, this operation is not reciprocal in the strictest sense.

We also studied the interaction volume of the EBSD. This part of the research involves discussion of the errors associated with the incautious using of Monte-Carlo simulation. In addition, this research also systematically studies some practical problems associated with EBSD technique, like the optimum binning ratio, pre-filtering of the patterns and saving all of the diffraction patterns.

3.2. SAMPLES AND INSTRUMENT

This research is mostly devoted to designing new experimental methods and systematic study of the EBSD technique. In principle, the methods we adopted are not limited to semiconductor samples only; they can also be extended to other crystalline samples without or with little adaptation. So, some of our testing, especially the early work is mostly done on metallic samples, such as 304 stainless steel and polycrystalline nickel, since metallic samples are easy to access and easy to clean.

Based on the same reason, we used a single crystal silicon wafer to test our designed image processing procedure. Through shifting electron beams to known distances and acquiring EBSD patterns from these points, we can measure the shift of the zone axis (in image space) and Kikuchi bands (in Hough space) and compare them with the calculated shifts.

Finally, we applied all of our methods on a sample of GaN/Sapphire heterostructure. This sample was grown by Dr. Milan Pophirstic at Emcore Inc. and was generously provided to us by Dr. Slade Cargill and Dr. Eva Campo. The sample is lateral epitaxial growth (LEO) of GaN on sapphire through using MOCVD the method. The growth temperature was 1000°C and growth pressure was 100 torr. First, a 2 μm thick GaN buffer layer was grown on the sapphire substrate (0001), and a 100nm thick SiN_x mask is planted on the buffer layer. GaN was then grown in the window regions with lateral overgrowth over adjacent regions of the mask. The window stripes are along the $[1\bar{1}00]$ direction. A SEM image of the sample is shown in Figure 3.1.

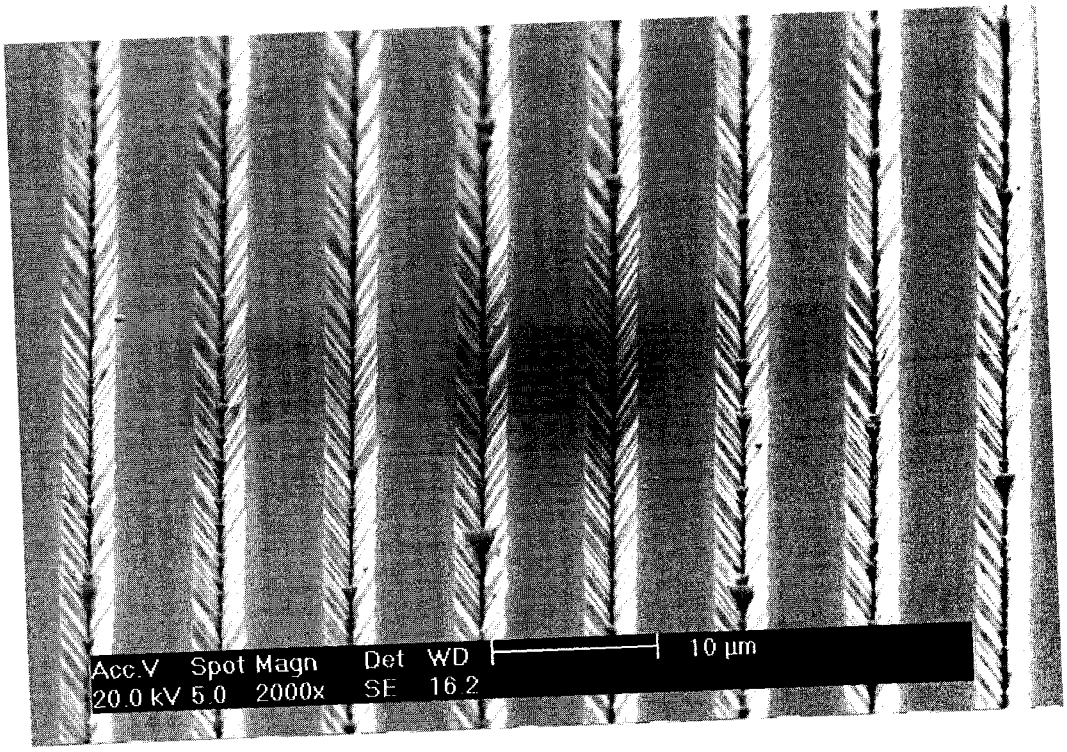

Figure 3.1. Secondary electron image of a GaN/Sapphire heterostructure, FEI XL30 ESEM was used. The vertical stripes are overgrown GaN.

Similar to our choices on testing samples, we also used several different EBSD/SEM configurations to do the test, including: 1). TSL's OIM system (Both SIT camera and CCD camera) installed on a FEI XL30 ESEM with a W filament. 2). Noran's Phase ID system with a CCD camera installed on a JEOL JSM 6300 field emission SEM. 3). TSL's OIM system (CCD camera) installed on a FEI XL30 ESEM with a Schottkey field emission gun (Special thanks to Mr. Dave Von Rohr of Drexel University). We also did some tests on an OPAL system (Oxford) installed on a Gemini 982 (LEO) Schottkey field emission gun SEM. (We are grateful to the help of Dr. Frederick Cosandey at Rutgers state university).

3.3. INTERACTION VOLUME OF EBSD

3.3.1. Monte-Carlo simulation

The interaction process of an electron beam with a specimen is very complex and Monte-Carlo simulation [53] is often used to study what happened inside the interaction area (on the scale of microns). The exact trajectory of one electron inside the specimen can be quite unpredictable, however, collectively, scattering events do obey some statistical distribution. Through sampling random numbers according to the distribution, the interaction process of the electron and the sample can be simulated to some extent. Most of the Monte-Carlo programs adopt the so-called "single scattering model". i.e. Inelastic scattering events cause electrons to lose energy continuously along the trajectories (obeying the Bethe equation), and elastic scattering events change the directions of the electrons. Conventional usage of Monte-Carlo simulation involves drawing a fairly large number of the trajectories of electrons into a two-dimensional graph, as showed in Figure 3.2 [54].

Research on the interaction volume and the spatial resolution of the EBSD technique using Monte-Carlo simulation has been reported [20]. This research claimed that the size of the interaction volume extends from +950nm (forward) to –700nm (backward) along the longitudinal direction and ranges from –800nm to +800 nm in the transverse direction for bulk copper sample at 20 kV accelerating voltage, Figure 3.2.

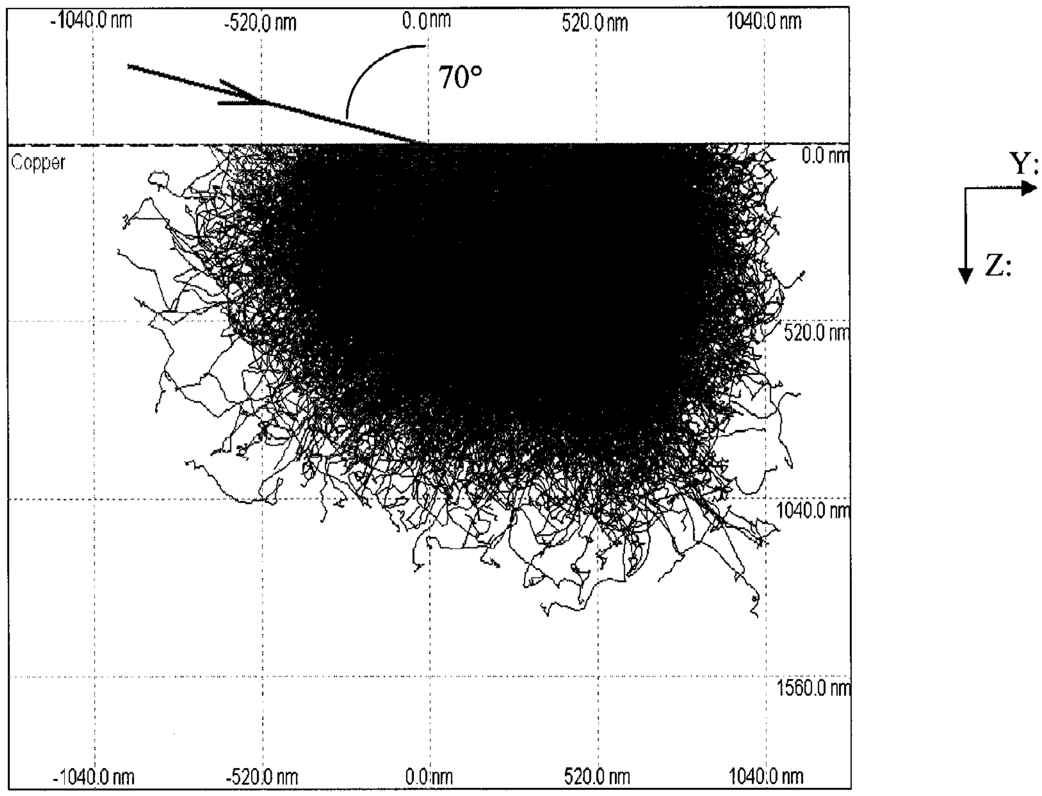

Figure 3.2. Monte-Carlo simulation of the interaction volume of Cu. 20 kV voltage, 0.5 keVcutoff energy. Red segments stand for the trajectories of the electrons scattered out of the sample.

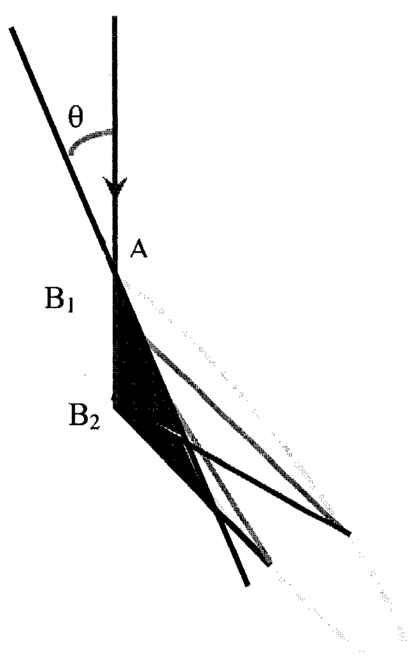

Figure 3.3 Illustration of Wells' Model. A small angle scattering event has a larger probability than a large angle scattering event, and the probability of one large scattering event is larger than two small angle scattering events. The distribution of the low-loss BSEs tends to have a lobe for a tilted sample.

The shaded area illustrated the interaction volume of EBSD.

This is not inconsistent with Monte-Carlo simulation.

3.3.2. Wells' Model

According to Oliver Wells' model on low-loss BSEs [55], the primary electrons lose energy progressively along a straight line, and one single collision event (Rutherford scattering) scatters the electrons out of the sample and most of the low-loss BSEs come from a depth of 10nm. As a result, the interaction volume of the EBSD should be more like the shaded area in Figure 3.3. Obviously, this is inconsistent with the result of Monte-Carlo simulation.

3.3.3. SurfaceMonitor- A Special Monte-Carlo simulation Program

In order to understand the reason for the inconsistency between the Monte-Carlo simulation and Wells' model, we wrote a Monte-Carlo program ourselves, the **SurfaceMonitor**. Instead of drawing all of those beautiful trajectories made by the primary electron beam, **SurfaceMonitor** outputs the positions (x,y) of all BSEs at the moment when they exit the surface of the sample. Instead of limiting the numbers of incoming electrons, we put the limitation on the number of the BSEs whose energy is larger than the cutoff value. Not satisfied with the infamous Pseudo Random number generator provided by Microsoft (the compiler of Visual C++), we used the acclaimed best algorithm in generating random numbers [56]. In order to test the validity of the Wells' model, we also tracked those electrons that experienced exactly one scattering event. Their last positions (x,y) on the exit surface and energies are recorded.

We did a series of studies on the interaction volume of copper, silicon and aluminum samples for different accelerating voltages using **SurfaceMonitor**. The comparison between the calculation using **SurfaceMonitor** and conventional Monte-Carlo method for copper sample is shown in next chapter.

3.4. HOUGH TRANSFORM

Two forms of Hough transform are usually used to detect linear features in digital images. 1) "Slope-Intercep form": The equation of a straight line is written as: $y = k.x+b$ in the Cartesian coordinate system, k is the slope and b is the intercept of the line. Thus, this line is expressed as one point H(k,b) in the parameter space (Hough space). In order to avoid the mathematical discontinuity for lines that are parallel to the Y-axis, the computer implementation for this form is quite complex. 2) "Polar coordinates form". In polar coordinates, the straight line is expressed as $\rho = x.\cos\theta + y.\sin\theta$, θ is in the range of [0, 180), ρ is the distance from the origin to the line. So, a straight line in the image space is represented as one point $H(\theta,\rho)$ in the parameter space (Hough space). This form is quite elegant and is usually adopted for the EBSD technique. Pseudo codes can be found in appendix 1. The Hough transform in this thesis always refers to the "Polar coordinates" form.

3.4.1. Hough transform of Kikuchi Bands

The Kikuchi bands in EBSD patterns have a width that is typically a significant fraction of the image field. The Hough transform of a Kikuchi band tends to have a characteristic shape. If not using a convolution mask, the Hough transform of a Kikuchi band usually has a rhombus shape, illustrated in Figure 3.5 and Figure 3.6. From the simple drawing illustrated in Figure 3.4, we know that the edges of the Hough peak can be described by sinusoidal curves. After applying a convolution mask, which usually has a "butterfly" shape, Figure 3.7 [33], the Hough transform of a Kikuchi band is assumed to have the so-called "butterfly" shape – A bright blob bordered by two dark region along the ρ direction.

For convenience, the Hough transform is usually carried out on an image field that is circular. The result of this is that the edge of the band that is closer to the center of the field is significantly longer than the edge of the band that is further out. This gives rise to one source of asymmetry in the peaks in the Hough transform. The "center of mass" of the Hough peak does not coincide with the midline of the Kikuchi band, illustrated in Figure 3.4 and Figure 3.5. Their difference (The distance from DD'to EE') is shown in equation 3.1

$$\Delta d = (\rho_2 - \rho_1)(\frac{\sqrt{R^2 - \rho_1^2}}{\sqrt{R^2 - \rho_1^2} + \sqrt{R^2 - \rho_2^2}} - 0.5) \qquad 3.1)$$

Equation 3.1. Δd is the distance from DD' to EE', ρ_2 is the distance from the origin to BB', ρ_1 is distance from origin to AA' , and R is the radius of the circle in figure 3.4.

If a Kikuchi band is displaced by a strain field, the peak in the Hough transform is not simply displaced but also changes shape. Specifically, if the band is displaced radially, that is if it moves further from the center of the pattern, the peak changes shape. This change can be seen to arise from the change of angle of the lines AB′ and A′B in Figure 3.5. A rotation of a Kikuchi band (that is a change of its orientation, while it stays at the same distance from the center of the pattern) will move the peak in the Hough Transform but not change its shape, not for this reason at least.

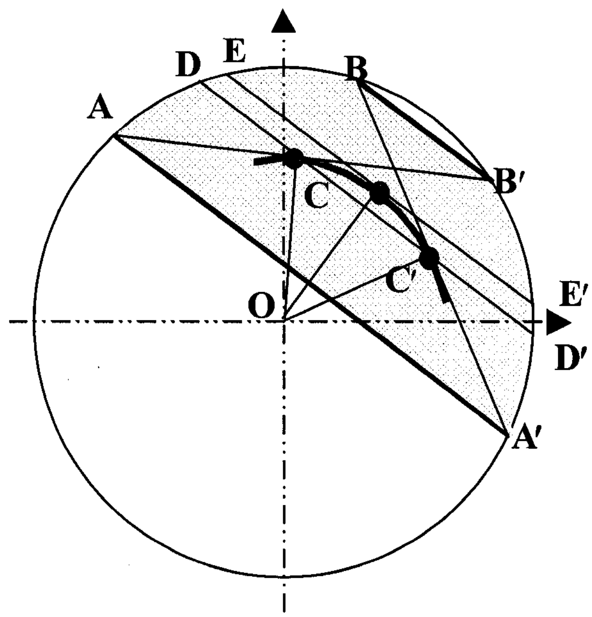

Figure 3.4. Schematic drawing of an EBSD pattern. A Kikuchi band is represented by the shaded area AA′BB′. DD′ is the midline of the Kikuchi band. EE′ is the line corresponding to the widest part (cc′) of the Hough peak (see next fihure).

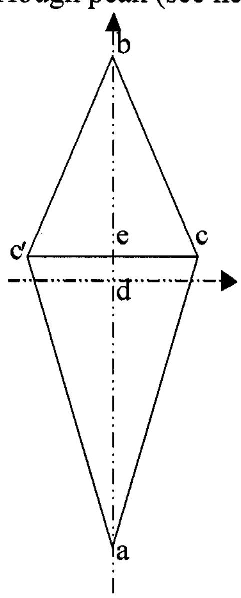

Figure 3.5. Schematic diagram of the peak in the Hough transform corresponding to the band in figure 3.4. The quadrilateral represents the area of lines lying wholly within the Kikuchi band. d is the midpoint of ab. Edges of this Hough peak, bc', bc, ac' and ac, can be described by sinusoidal curves.

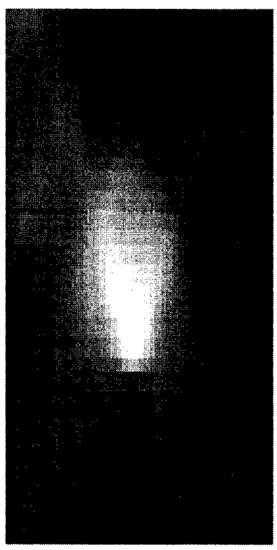

Figure 3.6. The Hough transform of a Kikuchi band.

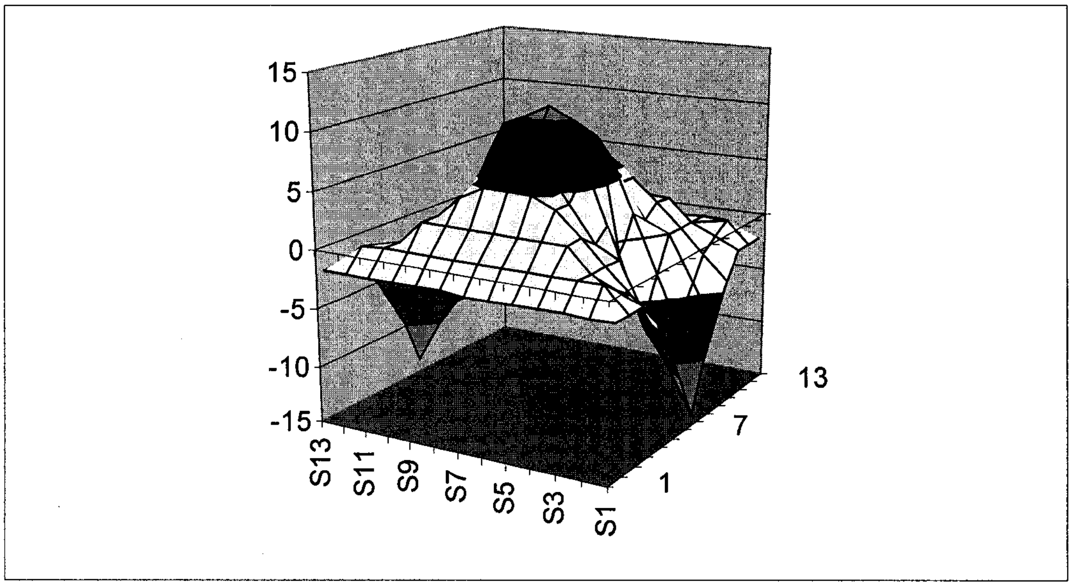

Figure 3.7. The “butterfly” mask, according to N.C.Krieger Lassen [33].

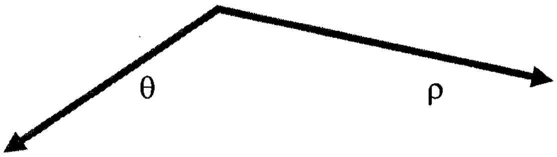

3.4.2. Artifacts introduced by the Hough transform

Figure 3.8 is an EBSD pattern from 304-austenite stainless steel. Figure 3.9a is the Hough transform (performed in the normal way) of Figure 3.8 without using any convolution mask. Figure 3.9b is an enlarged view of the area of the rectangular box in Figure 3.9a. The intensity discontinuities, which are obvious in Figure 3.9b are artifacts produced by the standard Hough transform. This type of artifact is most obvious when θ is equal to 45° or 135°. Unfortunately, performing a convolution with a butterfly mask does not guarantee the elimination of such discontinuities all the time. The peak detection process could easily be cheated into believing that there is a peak which corresponds to a false band in the EBSD pattern. We have found the reasons for these artifacts and provide two remedies to avoid them. The first remedy (form 1) is used to replace the conventional Hough transform and the second remedy (form 2) is mostly used to measure the shift of the Kikuchi bands in the Hough space

3.5. MEASURING THE SHIFT OF KIKUCHI BANDS AND ZONE AXES

We designed an image processing routine that can enable us to detect the shift of Kikuchi bands in EBSP to sub-pixel resolution. This routine is performed in Hough space. Accurate measurement of the shift of a zone axis in the EBSD pattern can also be used to estimate the elastic strains in the diffraction volume of crystalline materials [28]. We implemented this function too. In this thesis, sometimes we use the term "effective pixel size". For TSL's OIM Data collection system at least, since the CCD chip is coupled to the phosphor screen through a lens, the effective pixel size is defined as the effective size of the phosphor screen (diameter) divided by the actually used pixels of the camera.

3.5.1. Needed Resolution

The distortion of the atomic plane 30nm away from the core of a single dislocation is usually at the scale of 10^{-3} rad (α) [46]. For the case of an edge dislocation in silicon sample, the lattice bending changes from 10^{-2} rad (α) at 10nm from the dislocation core to 2×10^{-3} at 50nm from the dislocation core [5]. Thus, the shift of the Kikuchi band can be up to **D** multiplied by the distortion angle (α). **D** is the distance from the diffraction volume to the projection screen, which ranges from 20 to 40mm for most systems. So, at the extreme conditions, the shifted distance is about tens of microns - at the scale of fractions of one pixel to even more than one pixel, if the electron beam is small enough. However, this is a very gross estimation.

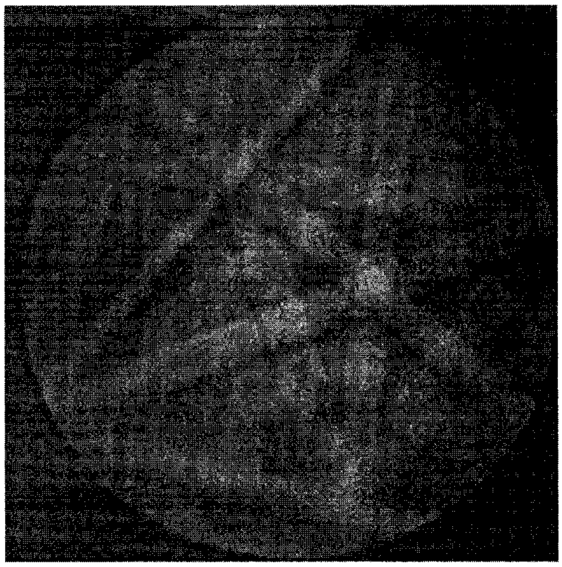

Figure 3.8 An EBSD pattern captured from 304 stainless steel. A TSL OIM system on a FEI XL30.

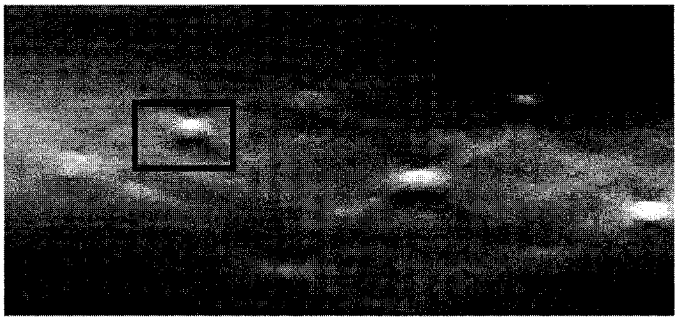

Figure 3.9a. Hough transform of figure 3.8, using no convolution mask.

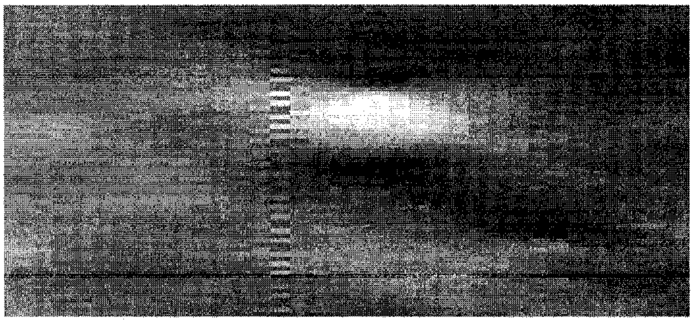

Figure 3.9b. Enlarged view of the box in figure 3.9a.

The dislocations threading out of the sample surface can be edge, screw or mixed dislocations. For reasons of simplicity, we used screw dislocations to estimate the effects of threading dislocations.

Since the Kikuchi bands are rigidly connected to the atomic planes and can be treated as the projection of diffraction planes, we set up the following coordinates, Figure 3.10.

Set the diffraction point as the Coordinate origin **O** and ***w*** is the normal to the set of planes in question, ***u*** is drawn from the origin towards the Kikuchi band in the diffraction pattern on the screen and is perpendicular to it. From ***w*** and ***u***, ***v*** can be determined automatically through building a right hand coordinate set. So, the unit vector perpendicular to the diffraction plane is (0,0,1). If a dislocation is introduced, the diffraction plane is slightly deformed to (δu, δv,1). δu is the quantity that will determine the shift of the Kikuchi band and δv is the quantity that determines the rotation. In more detail, the shift of the bands will be D.δu, D is the distance between the sample and the Kikuchi band on the phosphor screen. For the convenience of calculation, we always define another set of coordinates for the dislocation (x, y, z). For a screw dislocation, the direction of the dislocation will be on the z-axis. The displacement field of the dislocation **U**(***r***) can be written out easily.

These two sets of coordinates can be transformed to each other through a matrix **M**. So, in the ***u***,***v***,***w*** coordinates, δu and δv can be calculated. Thus, D.δu can be known.

Estimation following this method is in accordance with the first estimation. A more strict treatment of this method must include averaging over all the interaction volume, which makes the computation very complex.

Besides shifting the Kikuchi bands, dislocations can also rotate the diffraction bands slightly. However, detecting the rotation of the Kikuchi band is more difficult than measuring the shift, since one pixel difference between two lines only corresponds to 1/8 degrees (480×480 pixels) change. Experiment also shows for the EBSD patterns captured from the same point, the uncertainty of detected rotation can be worse than ¼ degree sometimes.

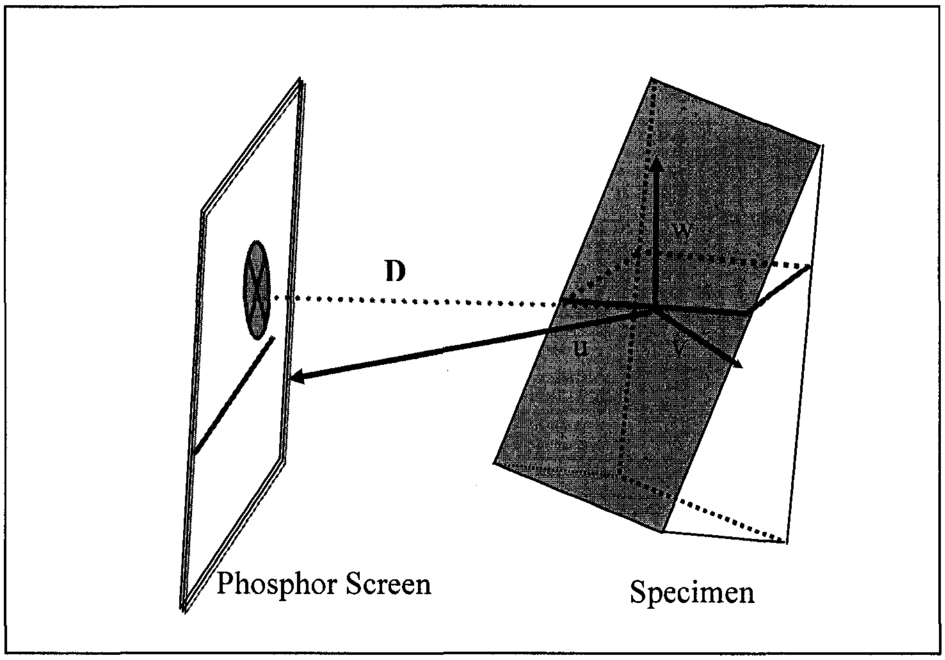

Figure 3.10. Setting up (u,v,w) coordinates to calculate the shift and rotation of Kikuchi bands under the strain field of a dislocation.

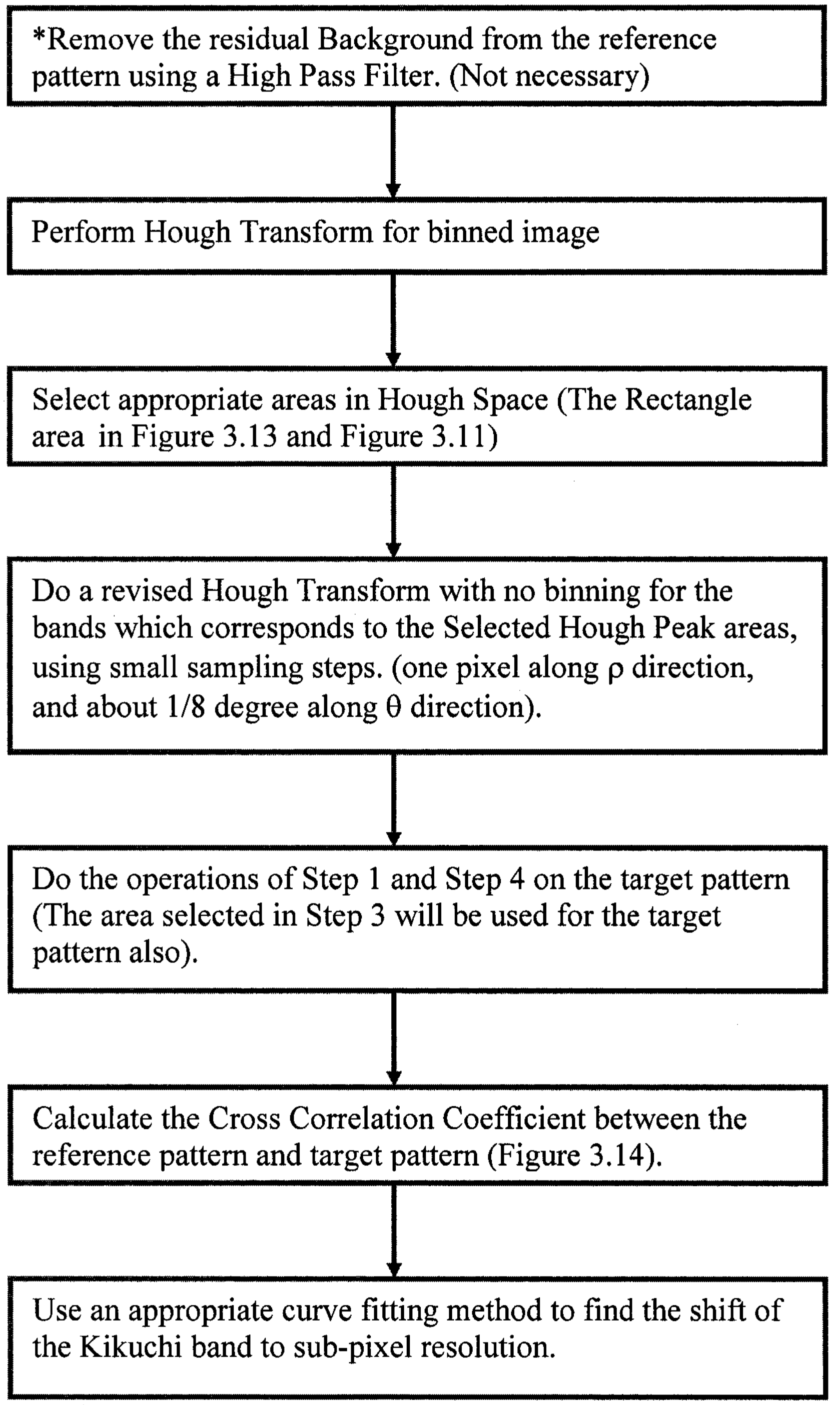

Figure 3.11. Shift detection routine for Kikuchi bands.

3.5.2. Shift Detection in the Hough Space

The band shift detection routine has been added to the OIM Data Collection Software. The routine is represented in a simplified way by the flow chart in Figure 3.11. It consists of following steps:

1). Choose a reference point in the specimen and get a good quality EBSD pattern from this point. This pattern works as the reference pattern (Figure 3.12).

2). Blur* this reference pattern using a large radius Gaussian filter and then subtract it from the original pattern and perform a standard Hough transform.

3). Select an appropriate bright peak in the Hough space as shown in Figure 3.13 and Figure 3.14. This peak corresponds to one Kikuchi band in the EBSD pattern.

4). Perform a revised Hough transform (no binning, small step size) on the band corresponding to the selected Hough peak only, and save the calculated data of this area as a "template". The revised Hough transform used is one in which the contribution of the image pixels to the Hough-space pixels is weighted according to their distance from the sampling lines. Careful explanation of the revised Hough transform can be found in next chapter.

5). Shift the beam to a different position and get another EBSD pattern, the target pattern.

6). **Blur this pattern using a large radius Gaussian filter and then subtract the blurred pattern from the original pattern and perform a revised Hough transform for the same area as the reference pattern. In this step, we also used our revised Hough transform with no binning of the EBSD pattern and small sampling step size.

7). Calculate the cross correlation coefficient for these two Hough peaks, as illustrated in Figure 3.15.

8). Using curve-fitting method to find the best fit to sub-pixel precision. In our experiment, we chose to use a least square fitting to a parabola. This operation is done on the cross correlation coefficient peak and its four nearest points along ρ direction.

9). Steps 5 to 8 are then repeated for other points on the sample.

**We found that step 2 is not necessary for many EBSD patterns.*

*** Blurring a pattern using a Gaussian filter and then subtracting the blurred pattern from the original one is mathematically equal to a Gaussian-deblur function.*

Band A

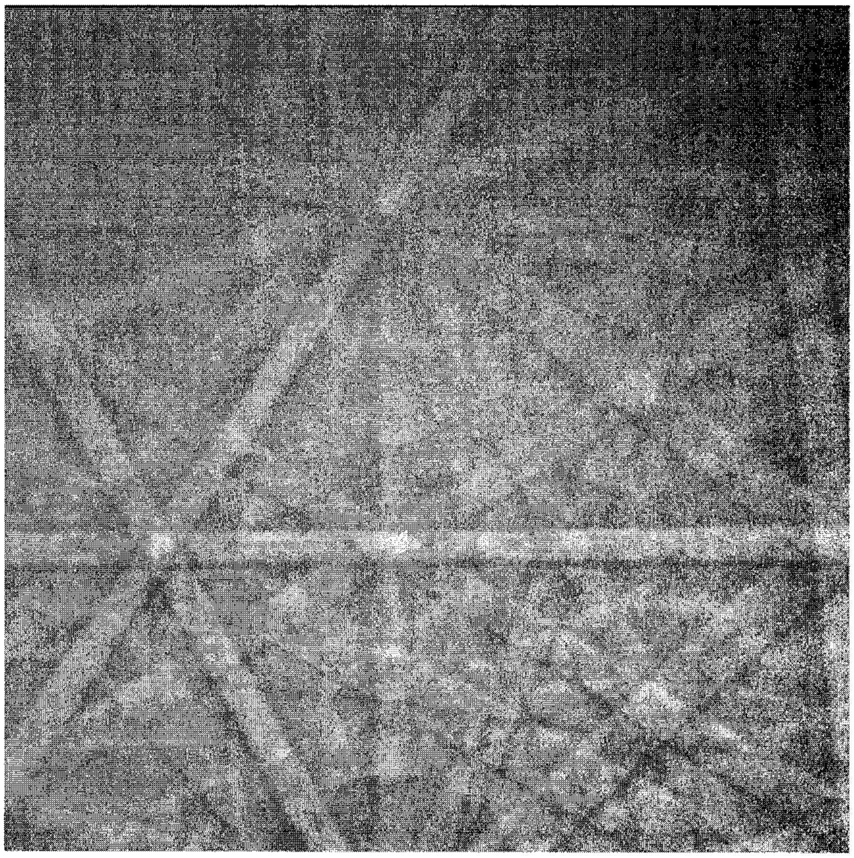

Figure 3.12. This EBSD pattern, captured from a Si wafer using Noran's Phase ID system, is used as a reference pattern. After Gaussian deblurring, the Hough transform of this pattern is shown in Figure 3.13. The Hough transform of Band A is inside the green frame in figure 3.13 and figure 3.14.

Figure 3.13. Select a small area in the Hough space of a reference pattern. This area corresponds to Kikuchi band A in Figure 3.10. Save the dataset of this small area as a template.

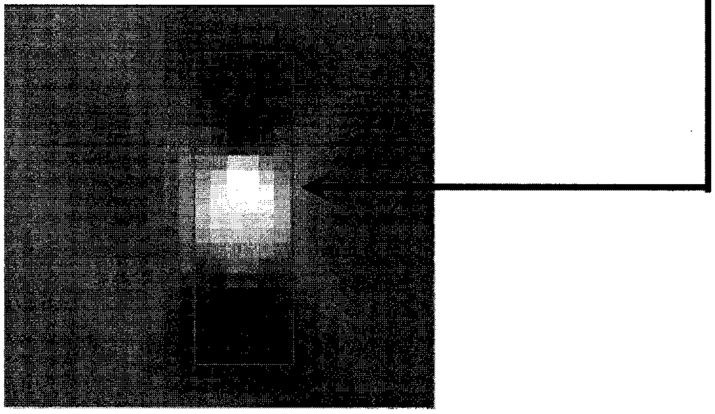

Figure 3.14. An enlarged view of a Hough Peak in Hough Space (Figure 3.13). The corresponding EBSD pattern is still binned. In our program, we will do a more careful Hough Transform for the uncompressed image. We will use the original floating point data calculated from the Hough Transform to do the cross correlation coefficient calculation.

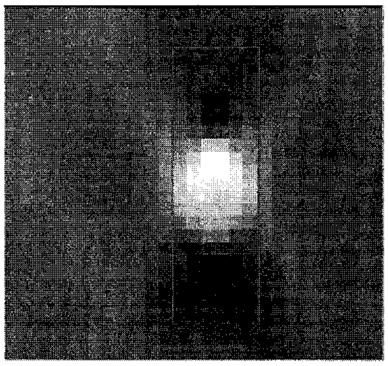

Figure 3.15a.

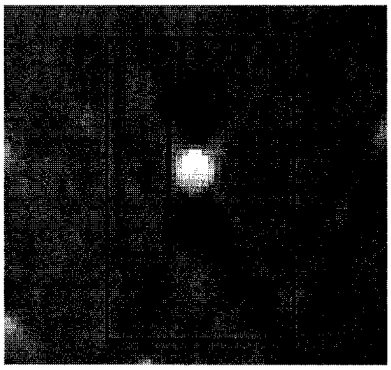

Figure 3.15 b

Figure 3.15. Calculation of the cross correlation coefficient in Hough space. The bright blob in the center of Figure 3.15a is the Hough transform of one Kikuchi band in the reference pattern. The outer frame in Figure 3.15a corresponds to the inner frame in Figure 3.15b. For Figure 3.15b, the inner frame is shifted one pixel by one pixel inside the outer frame. At each position, the cross correlation coefficient is calculated and the largest value corresponds to the best match.

3.5.3. Shift Detection in the Image Space

We wrote a program, **ShiftDetector,** to measure the shift of the zone axis in image space. This program is written using Visual C++® and works under Windows® 95/98/2000/XP. Phase Correlation and cross correlation coefficients are used as criteria. This program can calculate the cross correlation coefficient directly or through a Fourier transform. In order to improve the accuracy of the measurement to sub-pixel level, interpolation is used. For the phase correlation method, we used the interpolation method recommended by H.Foroosh [49].

This program allows the user to select a rectangular area of interest from one reference pattern and then measure the shift of this area with reference to the same area on another pattern, the target pattern. By using OpenGL, the calculated values (Cross Correlation coefficient or Phase Correlation) can be shown in 3-d form.

This program uses FFTW library [57] to do the Fourier transform. FFTW is a free, fast, easy to use for Fortran and C/C++ programmers. It doesn't need the size of the dataset to be a power of two.

3.5.4. Testing Methods:

We tested and compared these two shift detection methods, measuring the shift of Kikuchi bands in Hough space and measuring the shift of zone axis in image space, using a single silicon wafer, which can be assumed defect free. Through shifting the electron beams to some known distances and capturing EBSD patterns from these points, we can compare the calculated results and measured results from these two methods.

3.6. INTENSITY MAPPING OF THE EBSD PATTERNS

Conventional EBSD technique uses only the geometrical information from the diffraction patterns. The geometrical information is extracted from the intensity information through the Hough transform. On the other hand, IQ (Image quality) maps use intensity information indirectly and IQ maps show better resolution and more details than inverse pole figure maps. In this research, we propose to map the intensity information of the EBSD patterns directly. This method has the potential to provide more information than IQ mapping. Comparing to the detection of the shift of the Kikuchi bands, measurement of the intensity distribution for diffraction patterns is easy to calculate and the mapping process can be implemented conveniently.

3.6.1. Image Quality, Mean, Entropy and Standard Deviation of the EBSP

The mean, standard deviation and entropy are important quantities for describing images. The physical meaning of mean and standard deviation are self-explanatory and the definition of the entropy for an image is similar to that defined in thermodynamics, shown in equation 3.2. N is the grayness scale of the image and P_i is the probability for each grayness scale. Obviously, if an image covers all the grayness scale with equal probability, the entropy reaches the maximum value.

$$H = -\sum_{i=0}^{N-1} P_i \ln P_i \qquad 3.2)$$

In this research, we introduced these concepts into EBSD mapping to describe the quality and blurriness of the pattern in the EBSD patterns. In our revised TSL Data

Collection system, the maps of these factors can be generated in real time. We also wrote a stand-alone program (**DataMapping**), which can map these factors offline.

3.6.2. Intensity Distribution of Selected Areas in the EBSD patterns

Mapping of the intensity distribution of the EBSD pattern is implemented in two programs. Mapping of the intensity of the bands is implemented in the revised OIM Data Collection Program, and mapping of the intensity of the zone axis is in a standalone program. (Appendix 3)

We defined several parameters, such as the mean of the intensity of one Kikuchi band, the mean of the intensity of one zone axis, the mean of the intensity of one zone axis divided by the mean of the intensity of the pattern, and the standard deviation of the intensity of one band or one zone axis. We hope maps of these parameters could also reveal diffraction contrast caused by near surface dislocations.

3.7. APPLICATION ON GaN/SAPPHIRE STRUCTURE

In this experiment, we examined a GaN/sapphire heterostructure using both the shift mapping method and the intensity mapping method. An FEI XL30 ESEM with a Schottkey field emission gun SEM was used. The EBSD system was TSL's OIM system installed with a CCD Camera. First, The GaN/Sapphire sample was cleaned carefully using TCE/methanol/IPA for about 1.5 hours followed by de-ionized water rinsing, then we used a plasma cleaner to clean it for about thirty minutes before it was moved to Drexel University and put into the chamber of SEM. Four experiment sessions were performed.

3.8. OTHER ISSUES

3.8.1. Binning Ratio

Binning is used to suppress noise in EBSD patterns and to decrease the calculation time for Hough transforms and it is especially useful for the fast orientation mapping system. However, the selection of the binning ratio should not be arbitrary. Under-binning of the EBSD pattern is not enough to suppress the noise, and over-binning of the EBSD pattern is similar to the under-sampling phenomena in signal processing, which can cause the information to be lost and the resolution is decreased. As a result, there could exist an optimum-binning ratio for one set of experiments and experimental determination of this best binning ratio has practical meaning.

3.8.2. Gaussian Filter

EBSD patterns usually still have a background of varying intensity even after the frame integration and background correction. The residual background could affect the accuracy of the peak detection and further affect the accuracy of orientation determination.

Using an appropriate filter to pre-filter the EBSD patterns has the potential to overcome the effect of residual background, suppress noise and improve the band detection accuracy. Typically, two kinds of filters have been used in EBSD. 1) Average filter 2) Gaussian filter. Both of these filters have been used successfully to reduce the residual background of the EBSD patterns. Through heavily blurring the EBSD patterns with a large radius filter and then subtracting or dividing the blurred pattern from the original one, the residual background can be heavily reduced.

Comparing to the average filter, the Gaussian filter is more advantageous: 1). A large radius average filter can bring in the so-called ringing effect and then cause contrast reversal for some details, while this is not the case for the Gaussian filter. 2). A Gaussian filter can be very fast. Some commercial EBSD software uses a fixed large radius Gaussian filter (r =20) to blur a raw EBSD pattern and then divide it from the raw pattern. It is named "soft" flat fielding [4]. However, implementing a large radius Gaussian filter is not trivial.

In this research, we tested a Gaussian filter to further subtract the residual background from batches of EBSD patterns after background correction using hardware. We wrote a program that implemented variable radius Gaussian filter using two methods, through Fourier transform and through recursive filtering [7].

3.8.3. Testing Method

The test was done on a 304-austenite stainless steel sample. In fact the sample is a TEM sample. After electro-polishing, the sample is cleaned by methanol and is put into the SEM chamber directly in order to decrease the adsorption.

The experiments were done on an ESEM (FEI, XL30) with a W filament and TSL's OIM Data Collection system (CCD camera with on-chip integration). The chosen accelerating voltage was 25 kV. The whole set of the EBSD patterns was recorded and analyzed offline.

4. RESULTS AND DISCUSSION

4.1. INTERACTION VOLUME OF EBSD

4.1.1. SurfaceMonitor .vs. Projection

Figure 4.1 shows the interaction area of a pure copper sample using a conventional Monte-Carlo simulation program [54]. The sample is tilted 70 degrees, the accelerating voltage is 20 kV and the chosen cutoff energy is 18 keV. The colorful trajectories are drawn to illustrate the interaction area. In order to achieve statistical accuracy, a large number of electrons (20,000) are used. As a comparison, Figure 4.2 is the result of a calculation from **SurfaceMonitor** - the Monte-Carlo simulation program of our own, which records the position of the BSEs the moment they exit the surface of the sample. Figure 4.3 is similar to Figure 4.2. It also records the last position left on the surface of the sample by the back-scattered electrons, which experienced exactly one single scattering event. i.e. the Wells' model . These two Figures show that when the BSEs leave the sample surface, nearly all of them are in the forward direction. Those BSEs scattered into the backward direction can be simply neglected. Furthermore, the spatial distribution of the BSEs on the exit surface looks like a wedge, rather than an elliptical area, as usually supposed. The area near the electron beam has a higher BSE intensity. The center of this wedge has a certain distance from the impinging point of the primary electron beam.

The difference between the results of the conventional Monte-Carlo simulation and **SurfaceMonitor** can be easily understood: Usually, the calculation of the Monte-Carlo simulation is done in three dimensions [53], that is, the position of all of the electrons are tracked in 3d space (x,y,z). However, the trajectory graphs are only drawn in 2d space, most often it is in (y,z) plane. This means that the trajectories shown in Figure 4.1 are the projections of the trajectories. Interpreting drawings of the Monte-Carlo trajectories drawings without realizing this fact could lead to error and this error can be quite huge, especially, when the sample is highly tilted, as in the EBSD technique.

The reason for the formation of this particular shape of the distribution of BSEs on the sample surface is easy to understand. First, we assume the electron beam slightly broadened for the first several nm distances when it is inside the sample (Figure 4.4) and the total number of electrons in the electron beam slightly decreased, considering that some electrons are scattered out and some being absorbed by the sample. In fact, we can also simply neglect this broadening effect and suppose all the scattering effect happened along one line, as that described in Wells' Model [55]. We further suppose those electrons being scattered out of the sample were scattered by one "averaged" low angle scattering event with an optimum angle $\theta(E)$. If an electron experienced multiple scattering events, this assumption simply averaged the total scattering effect to one "averaged scattering event". So, there must exist a cone with a half center angle θ, Figure 4.6, and this angle is far less than 90° in most cases. On the conical surface, the electrons can be scattered with equal probability to any direction. However, due to the limitation of the geometry of the sample, only electrons on a very small part of this cone have the possibility to leave the sample, as shown in Figure 4.5. The intersection of the cones with the sample is roughly related to the distribution of the BSEs on the surface of the sample (Figure 4.6). From the top to the bottom of the broadened electron beam, the numbers of electrons decreased but the size of the area increased and the scattering length increased, thus the cones corresponding to area B are very scattered comparing to the cones corresponding to area A in the Figure 4.6. As a result, the BSEs corresponding to area B are scattered further away from the impinging point comparing to area A. In addition, the density of the electrons corresponding to area B is less than that of area A. Basically, this is similar to Wells' model. However, we extended it to 3 dimensions, considered the effect of beam broadening and used "averaged scattering event" to replace the single scattering event, which is not very precise.

This model also suggested that if we were able to observe the interaction area from the (x,z) plane, the interaction volume should look more like that shown in Figure 4.7. Besides, according to above analysis, the one single event model (Wells' Model) is not precise and not complete.

Even though there is a general agreement on the fact that EBSD patterns are formed by low loss BSEs, it is still not clear what is the range for the cut-off energy. In addition, the interaction volume has a strange shape. So, the problem of spatial resolution of EBSD is very complex and it is beyond the scope of this research.

The Monte-Carlo simulation treats the sample as if it is homogeneous along every direction, which is not true for a crystal. Channeling contrast, which dominates the EBSD patterns, is totally missed in the Monte-Carlo simulation. So, the Monte-Carlo simulation can give us only a general picture of what happened inside the interaction volume.

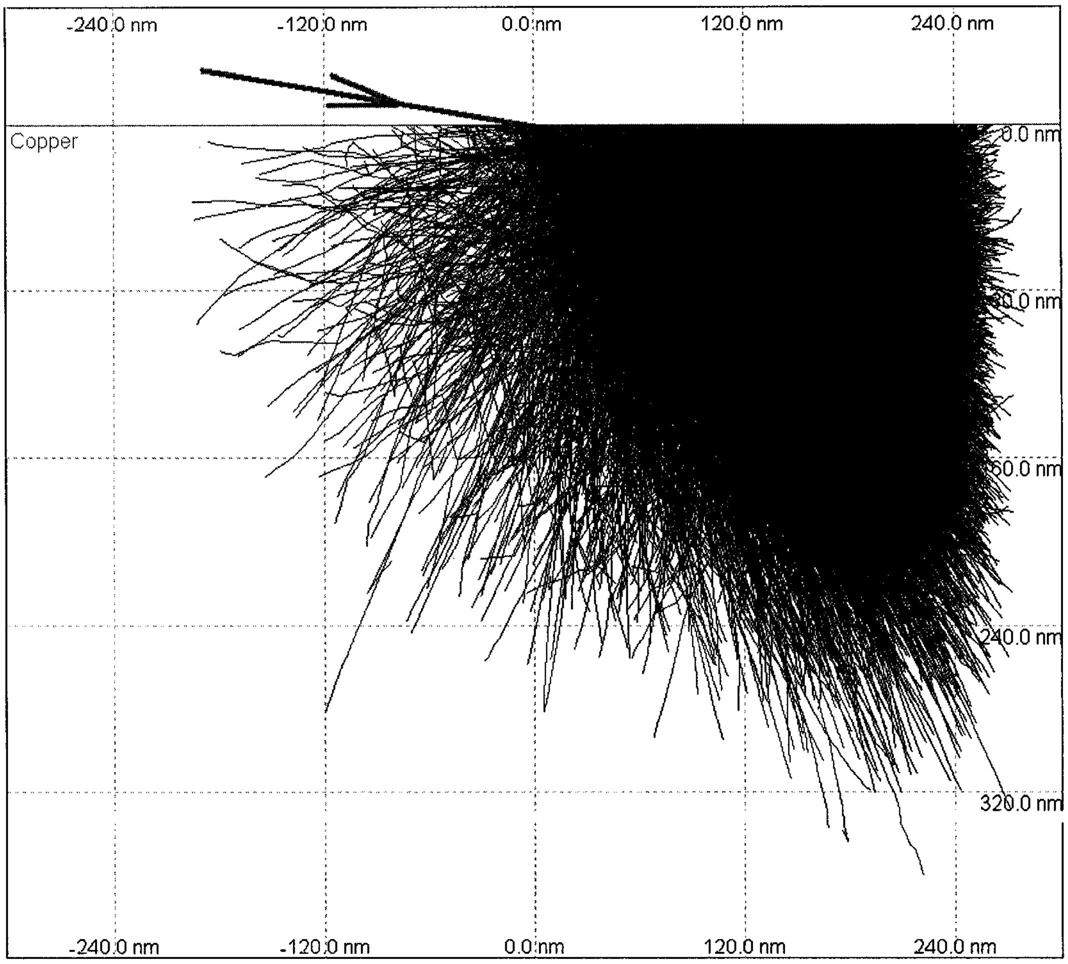

Figure 4.1. Monte-Carlo simulation of the interaction volume of copper. The accelerating voltage is 20kV, and the cutoff energy is 18kev. The trajectories of light color are made by those electrons exit from the sample. The "trajectories" shown in this map are the projections of the real trajectories of electrons in the sample. Compare this with Figure 4.2.

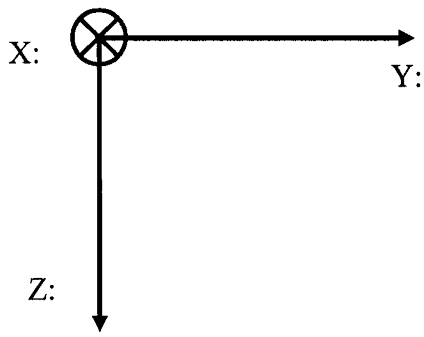

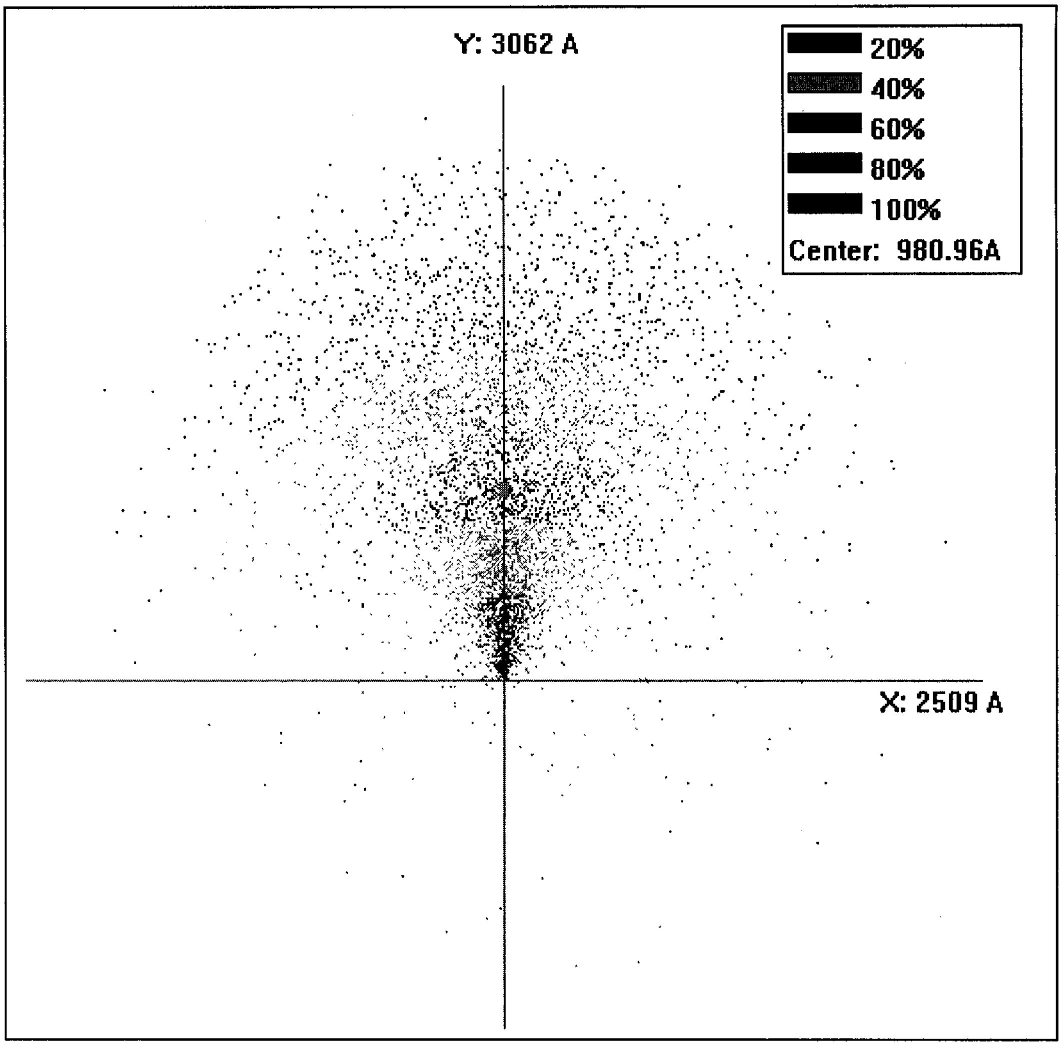

Figure 4.2. Calculation result from **SurfaceMonitor** for a copper sample. The accelerating voltage is 20kV, and the cutoff energy is 18kev. This Figure shows the position of the BSEs the moment they left the surface of the sample. The BSEs are assigned different greyness according to their distance to the impinging point. Compare this with Figure 4.1.

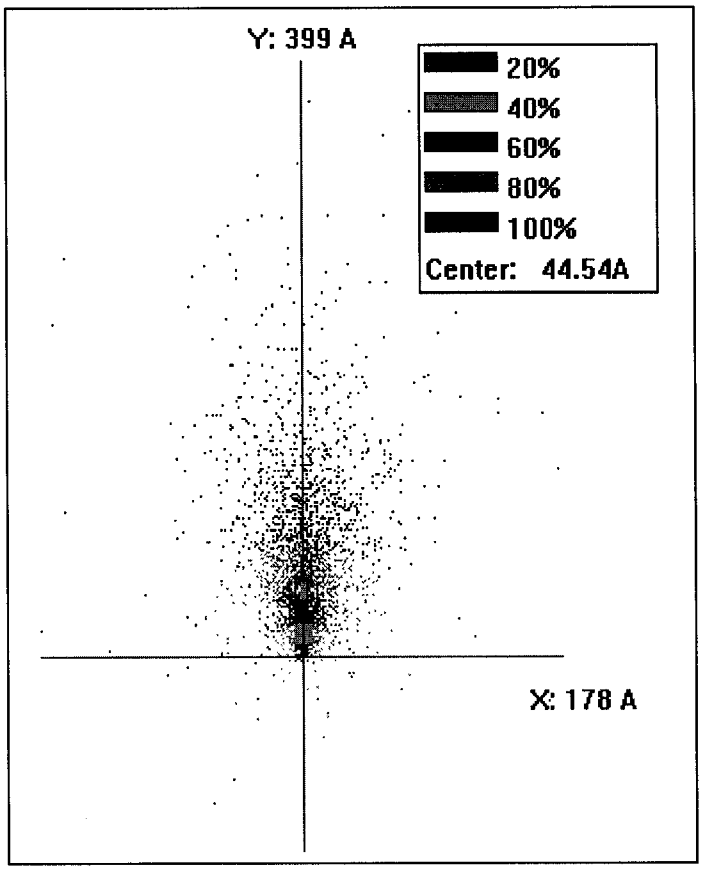

Figure 4.3. Calculation result from **SurfaceMonitor** for a copper sample. The accelerating voltage is 20kV. This Figure shows the position of the BSEs the moment they left the surface of the sample. Only those BSEs that experienced just one scattering event are recorded. The BSEs are assigned different grayness according to their distance to the impinging point. Compare this figure with Figure 4.1.

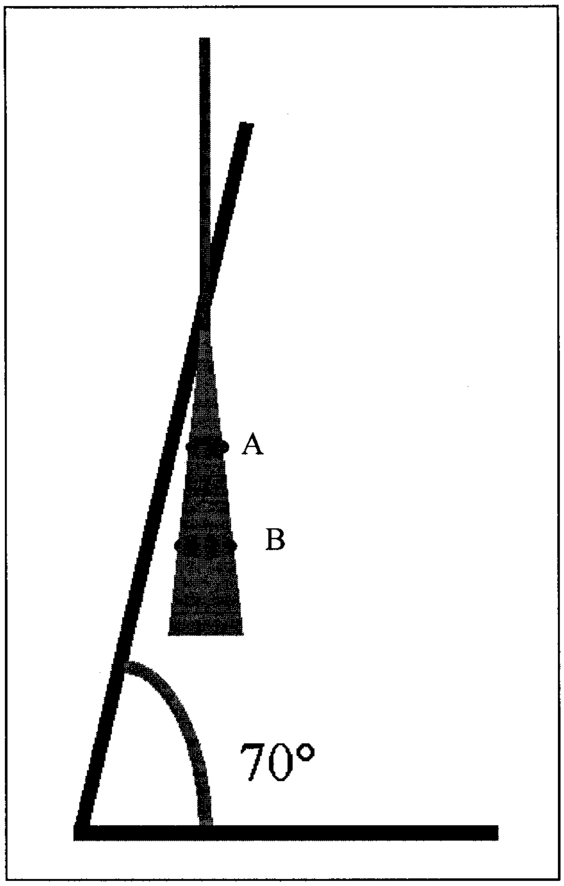

Figure 4.4. For the first tens of nm inside the sample, we can assume the electron beam slightly broadens. The number of electrons passed from area B is less than the electrons passed from area A

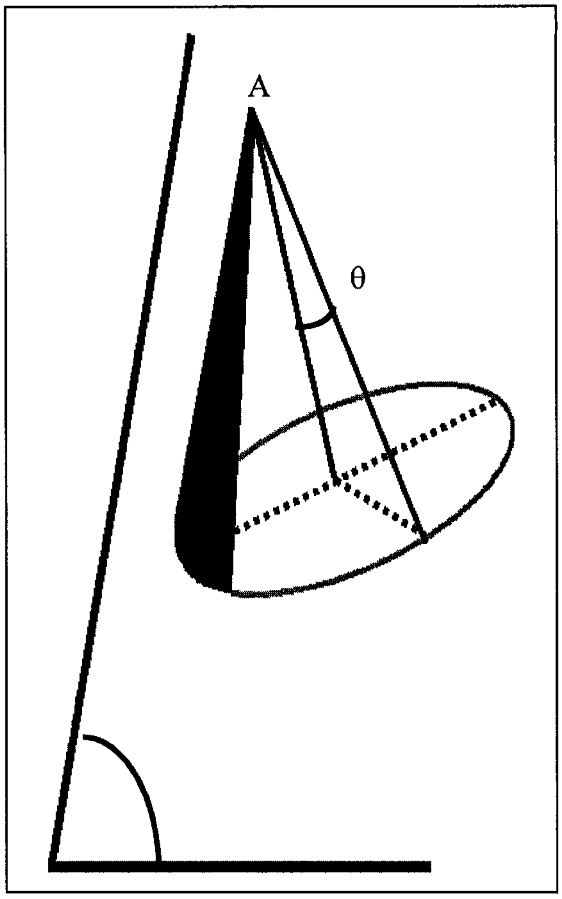

Figure 4.5. For electrons at place A, there exists a cone with half top angle θ. On the conical surface, electrons have equal opportunity to be scattered out along any direction. However, only those electrons falling into the shaded area has the possibility to leave the sample.

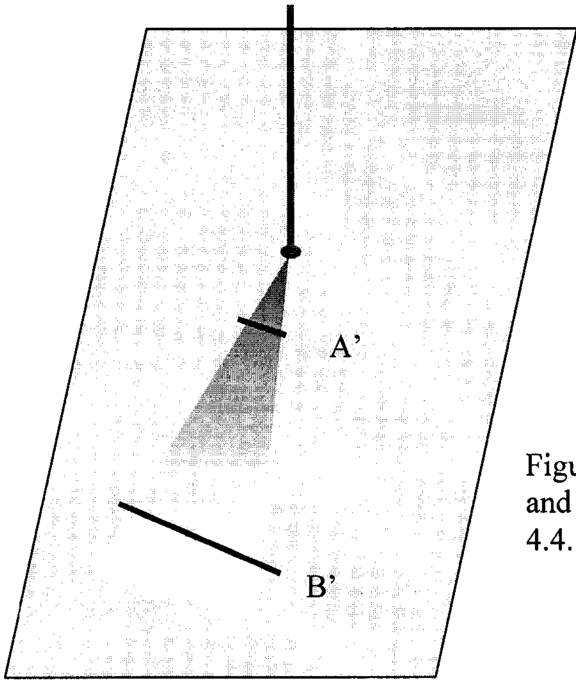

Figure 4.6. Area A' corresponds to A and B' corresponds to area B in Figure 4.4.

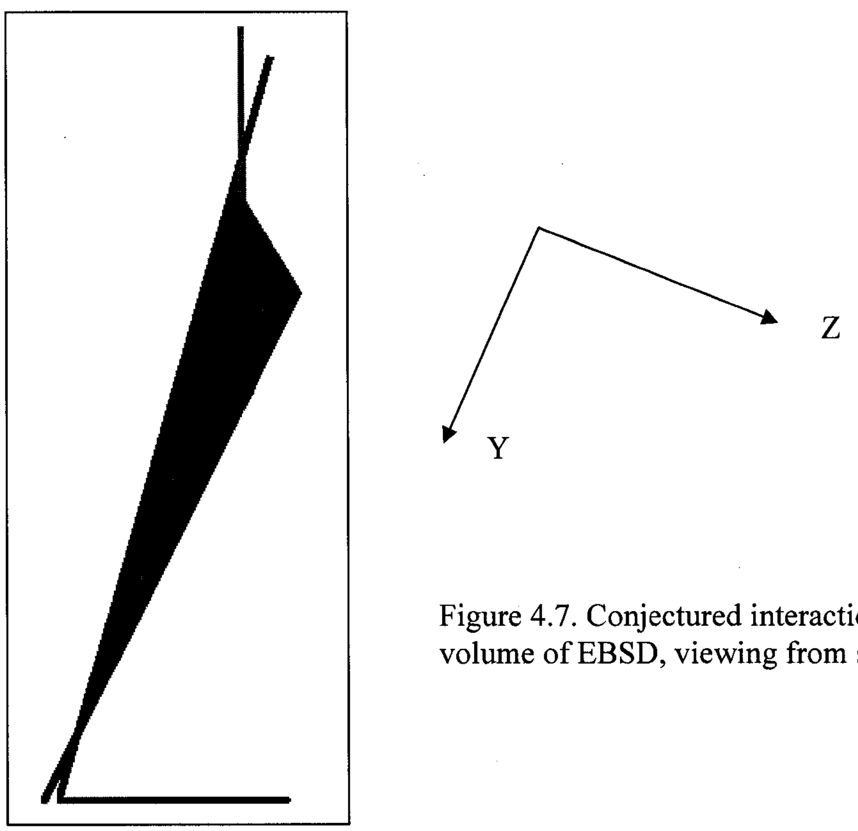

Figure 4.7. Conjectured interaction volume of EBSD, viewing from side.

4.1.2. Summary of This Section:

This section (Ch 4.1) discussed the interaction volume of the EBSD. Conventional studies using a Monte-Carlo simulation program to estimate the interaction volume and resolution could lead to over-estimation, if not paying attention to the projection problem. We wrote a special Monte-Carlo simulation program ourselves, this program records the position of the BSEs the moment they left the surface of the sample. Our simulation shows the interaction area of the EBSD technique has a strange shape on the sample surface. We further conjectured the shape of the interaction volume, which is different from conventional belief.

4.2. REVISED HOUGH TRANSFORM

4.2.1. Origin of the Sampling Artifacts

The principle of the Hough transform is that the intensity at a point in the Hough space represents the intensity along a line in the original image. The coordinates in Hough space are usually taken as θ and ρ. Thus a point θ,ρ in the Hough transform represents a line at an angle θ and at a distance ρ from the center of the original pattern. There are many lines that go through each pixel in the original image, so the intensity in each pixel in the image contributes to the intensity at many points in the Hough transform (depending on the step size along θ direction, $180/\Delta\theta$).

The standard way to perform the Hough transform is to calculate its value on a uniform grid. That is to say it is evaluated for equal steps in angle and equal steps in ρ. The choice of equal steps in ρ corresponds to evaluating the intensity along lines that have the same spacing (generally the spacing of the pixels in the pattern) independent of the angle of the line. Pixels in the image are assigned to the lines by rounding ρ to an integer. Since the spacing of the pixels perpendicular to a particular line is not (in general) commensurate with the integer spacing of the lines, different lines (of the same parallel set) sample different numbers of pixels in the pattern. The effect is particularly dramatic at 45^0 (and 135^0) since, as shown in Figures 4.8 and 4.9, some of the lines sample two rows of pixels whereas others sample only one. This is the origin of the artifacts shown in Figure 3.9a and Figure 3.9b. The principle of the Hough transform and a pseudo code implementation of it are given in the appendix 1.

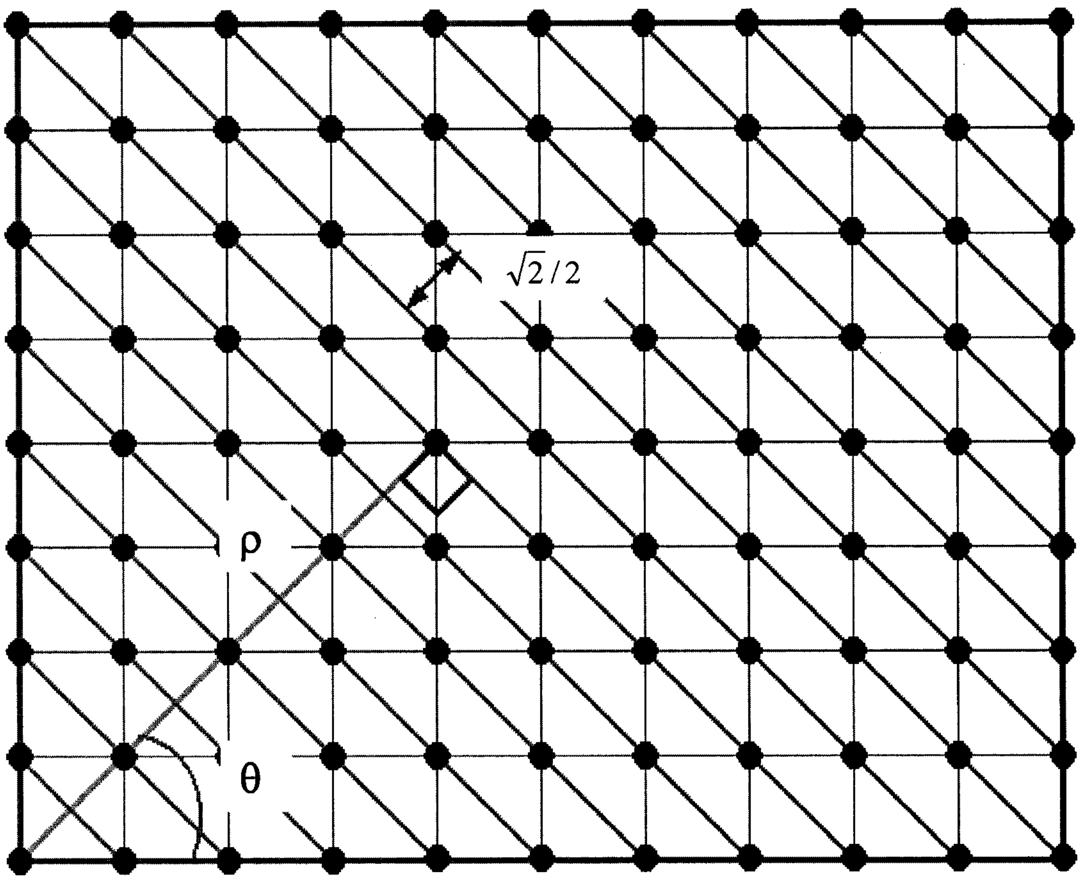

Figure 4.8. When θ is equal to 45°(135°), the distance between two nearest lines is $\sqrt{2}/2$ pixel, instead of 1.

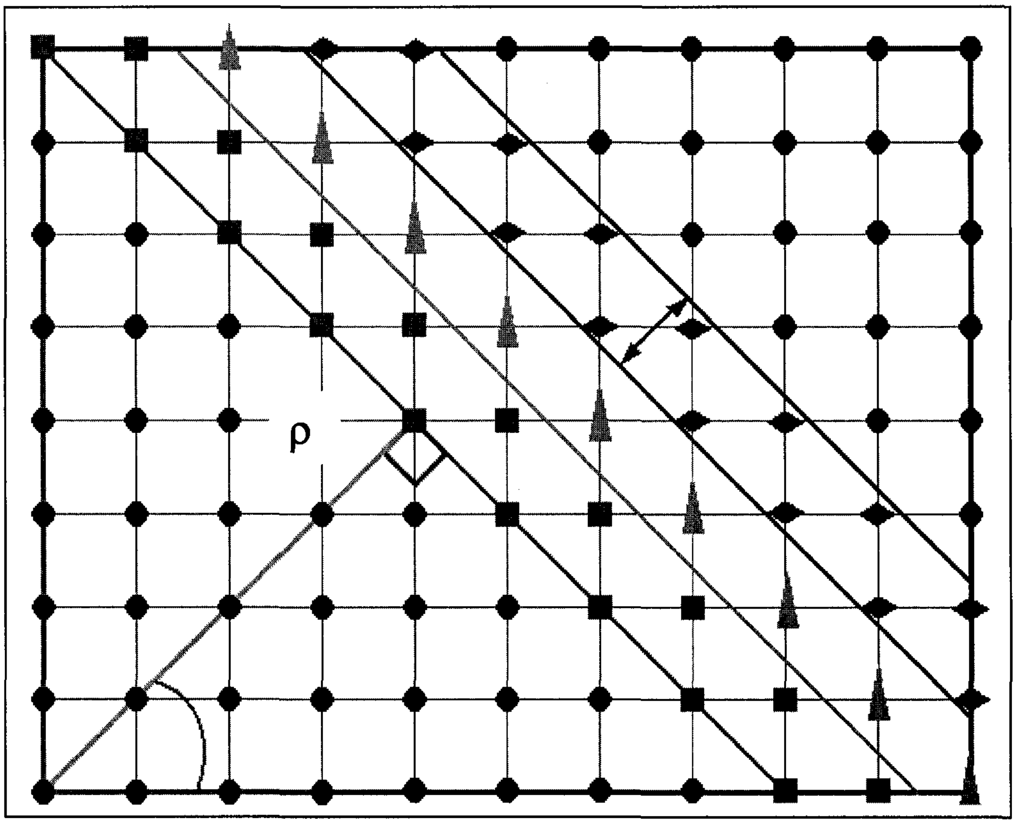

Figure 4.9. The distance between two lines is exactly 1 pixel. The Standard Hough transform samples the image space using equal steps of 1 pixel. As a result, some lines sample twice as many pixels as others.

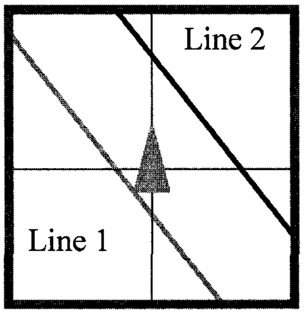

Figure 4.10. Illustration of the "Weighting the points" method. The intensity of the pixel marked by a triangle on the left figure is distributed more to line 1 than to line 2, according to its distance from the lines.

4.2.2. Revised Hough transform

There are several things that might be done to avoid these artifacts appeared in the Figure 3.7. The first is rather simple. If instead of adding the intensities of the pixels along the line to get the intensity at the point in Hough space the intensities are averaged, the artifact that arises from the difference between the spacing of the pixels and the spacing of the lines will be eliminated. Averaging is desirable anyway since it also eliminates the effect that Hough intensities fall near the top and bottom of the Hough plot (where ρ is close to its maximum or minimum value) because the chord is shorter there. However it is not ideal since the pattern pixels do not contribute in the right way to the Hough and because the noise will vary from pixel to pixel in Hough space.

We are aware of three other approaches to improving the way the Hough data is calculated.

1 "Nearest to the line". The principle of this method can be illustrated with reference to Figures 4.8 and 4.9, for the 45^0 case. Some of the lines have twice as many pixels contributing to them as other lines. One way to correct the problem is simply to count the pixels that lie closest to the line and discard the pixels that are further away. This will remove the artifacts but does so at the expense of discarding data. This method has been implemented and shown to work (pseudo code is given in appendix 1).

2 "Weighting the points". The pixels given as triangles in Figure 4.10 lie between two of the 45^0 lines. In this method the intensities of these pixels will be added – with a suitable weighting factor – to *both* lines. The weighting will be larger the closer the pixel is to the line. Pixels that lie exactly on a line contribute to that line only. This method

has the advantage that it uses all the data but still gives values in the Hough plot that correctly represent the intensities in the lines in the pattern. This method has also been implemented and shown to work (pseudo code is given in appendix 1).

3 "Slope-Intercept Hough". The most common form of the Hough, as described here, is to parameterize the Hough plot as a function of θ and ρ. However, instead the Hough can be plotted as a function of the slope and intercept of the lines. The equation for a line is given as $y = kx+b$ [51], instead of $\rho = x\cos\theta + y\sin\theta$. This form of the Hough turns out to avoid the artifacts because it is the intercept that steps uniformly not the spacing between the lines. We have not tested this method.

Our experiments showed that both the "nearest method" and "weighting method" could eliminate the artifacts successfully. There are advantages to each of them. The "nearest" method is simple and is readily compatible with the current commercial software. It is quite suitable for normal orientation mapping. However, careful attention must be paid on organizing data reasonably when programming. Experiment shows that, if implemented carefully, this method is slightly slower than the standard method (around 30%-40%). This speed difference is trivial for a modern PC and can be easily overcome by Moore's law. However, if the data for the Hough transform, such the order of the array dimensions, is not organized carefully during programming, this method is dramatically slow (8-10 times slower!). Sometimes, even a computer can be sensitive!

The "weighting" method should give, we feel, better results in the sense of giving the most exact position of the Kikuchi bands. Since part of our work involves detecting very small shifts in the bands, this is the method we adopted. We expect it to give the most accurate location of the peak in the Hough transform [2].

Using the slope-intercept form of Hough transform is also a good choice. However, this implementation is not as elegant as the polar form of the Hough transform [51].

4.2.3. Summary of this Section

This section (Ch 4.2) is focused on the Hough transform. The algorithm of conventional Hough transform used in the EBSD technique is flawed. It brings in artifacts, which is most obvious when no convolution mask is used.

We found and explained the origin of the artifacts and gave two remedies to remove them. The "Nearest to the line" method is simple and is readily compatible with the current commercial software. Its performance is slightly slower than standard algorithm and it is quite suitable for normal orientation mapping. The "Weighting the points" method should give better results in the sense of giving the most exact position of the Kikuchi bands. The "weighting" method is the basis for our method of detecting the shift of Kikuchi band, which will be covered in next section.

4.3. MEASURING THE SHIFT OF KIKUCHI BANDS AND ZONE AXIS

First, we tested the integrity of the program (**ShiftDetector**) and our revised OIM Data Collection software. We choose an EBSD pattern, Figure 4.11, as the reference and then displaced this pattern a known amount (one pixel left and one pixel down) and saved it as a target pattern. Both methods (programs), measuring the shift of Kikuchi bands in Hough space and measuring the shift of zone axis in image space, can measure the displacement accurately to sub-pixel; no matter whether the cross correlation coefficient or phase correlation is used as the criterion. The Kikuchi bands used for the test are marked by arrows and the testing zone axes are marked by frames, showed in Figure 4.11.

Table 4.1 lists the results of the "band detection" method. In this experiment, the cross correlation coefficient is used as criterion, each selected "Hough peak", which is used to do the cross correlation, has an angular width of several degrees. The θ value for the centerline of the Kikuchi band, *θ*, is listed on the second row in table 4.1. To the first approximation, the displacement of the Kikuchi band along ρ direction can be calculated using equation 4.1:

$$\Delta\rho = -(Y_{shift}*\sin\theta + X_{Shift}*\cos\theta).\ Y_{shift} = 1;\ X_{Shift} = 1. \qquad 4.1)$$

The results of the shift measurement of the zone axes are listed in Table 4.2. Both the cross correlation coefficient and phase correlation are used as criteria; we omitted the interpolation for the calculation of the cross correlation coefficient.

We further repeated this test especially for the band shift detection method on a pattern with heavy noise, Figure 4.12. The calculation results, which are listed in table 4.3, are still very reliable. Theses calculations proved there are no serious problems associated with the two programs.

The two shift measurement methods listed above have been further checked and compared by doing the following set of experiments.

A piece of single crystal silicon wafer was used as the sample. The wafer can be assumed to be defect free and to have the same orientation everywhere. The electron beam was moved to known distances and, at each position of the beam, two independent EBSD patterns were obtained from the same point on the sample and analyzed. In this way, we could test whether the shift of the Kikuchi bands detected by the program is in accordance with the shift predicted from the known beam shift. The experiments were done on a W filament SEM (FEI, XL30) with TSL's OIM Data Collection system, which uses a CCD camera. A 20kVaccelerating voltage was used in the experiment and the beam shifting procedure is shown in Figure 4.14. At each point, two separate EBSD patterns were captured at different times. All together, we acquired a set of 14 EBSD patterns from 7 points and they were named from **Pattern1a** to **Pattern7b** sequentially. Each EBSD pattern has 987×987 pixels and the data collection time was about 21.25s/pattern.

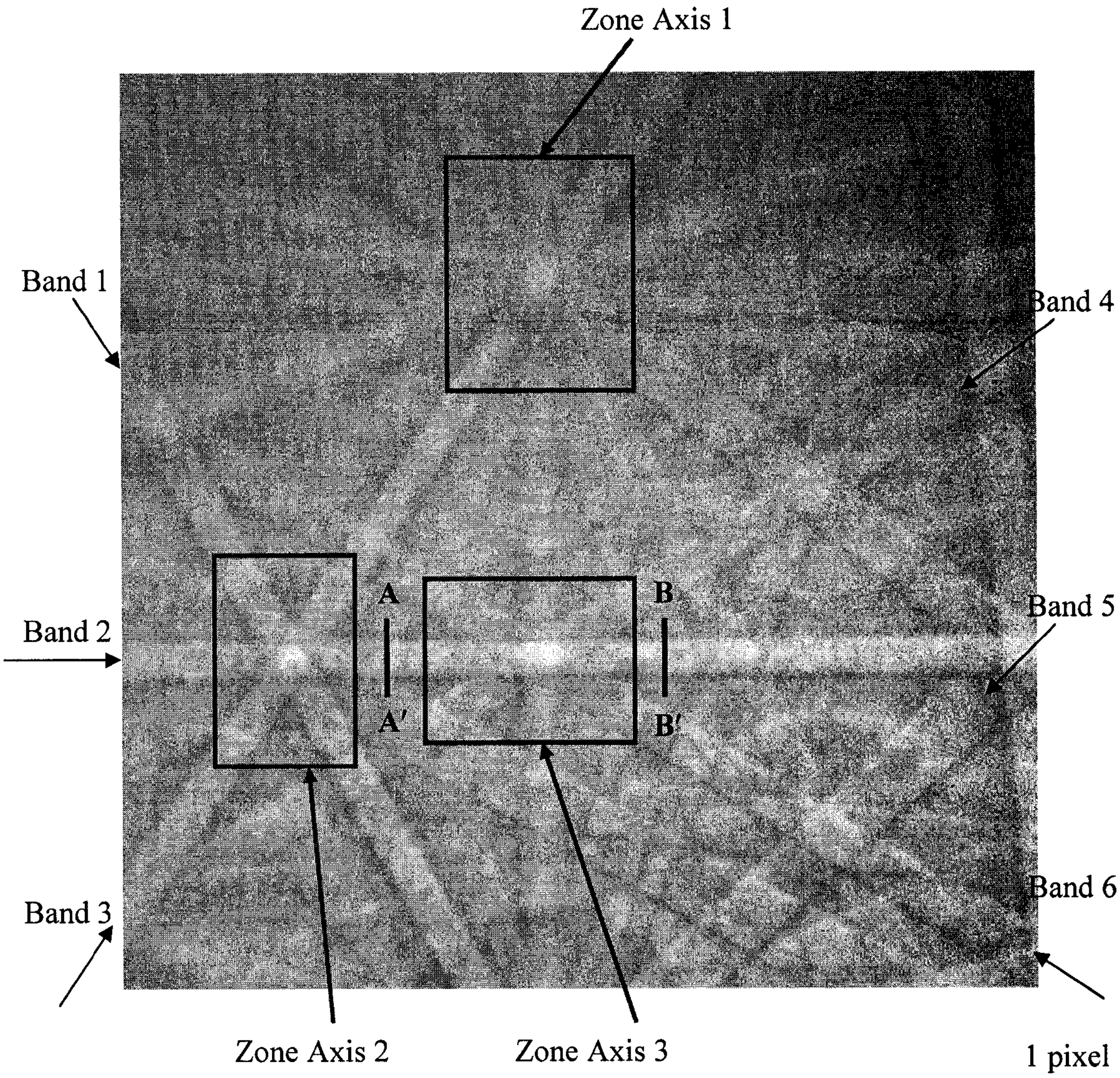

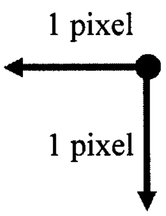

Figure 4.11. This EBSD pattern is used as a reference to test the integrity of the calculation. Shift this pattern one pixel left and one pixel down to get the target pattern. The original pattern has 512×512 pixels.

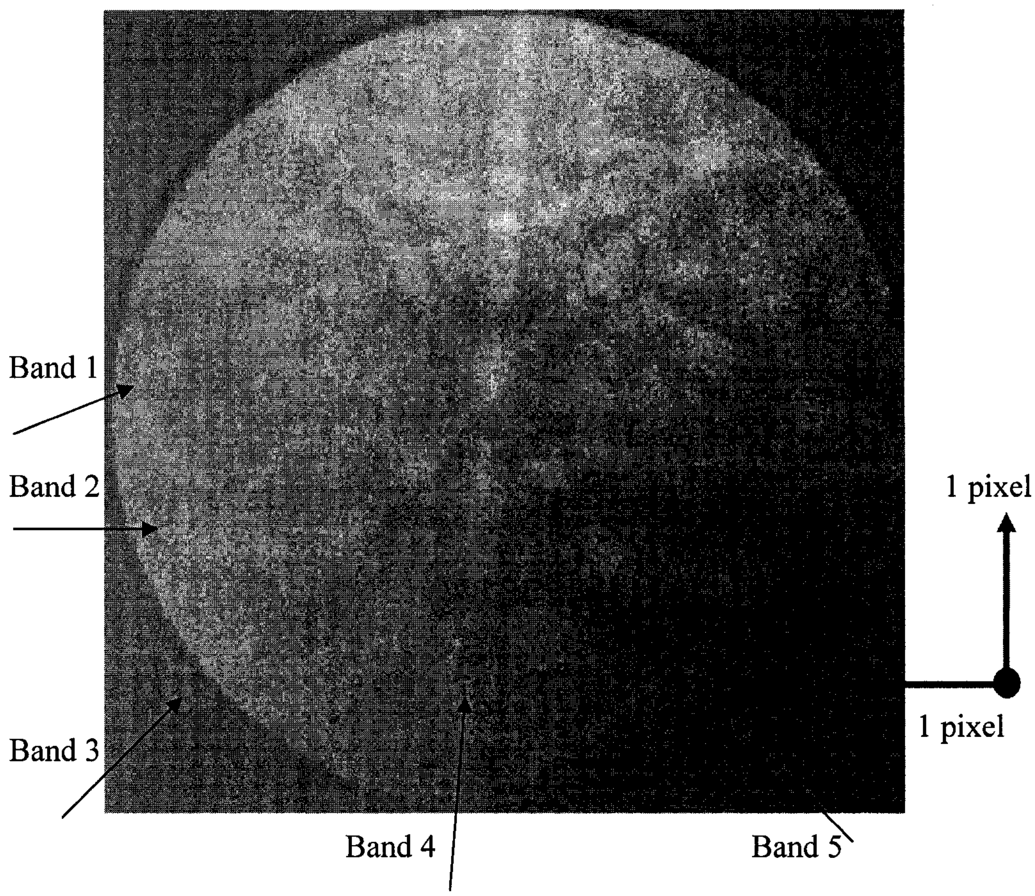

Figure 4.12. This EBSD pattern is also used as a reference to test the integrity of the calculation. Shift this pattern one pixel left and one pixel up to get the target pattern. The original pattern has 454×454 pixels. We chose a noisy EBSD pattern deliberately.

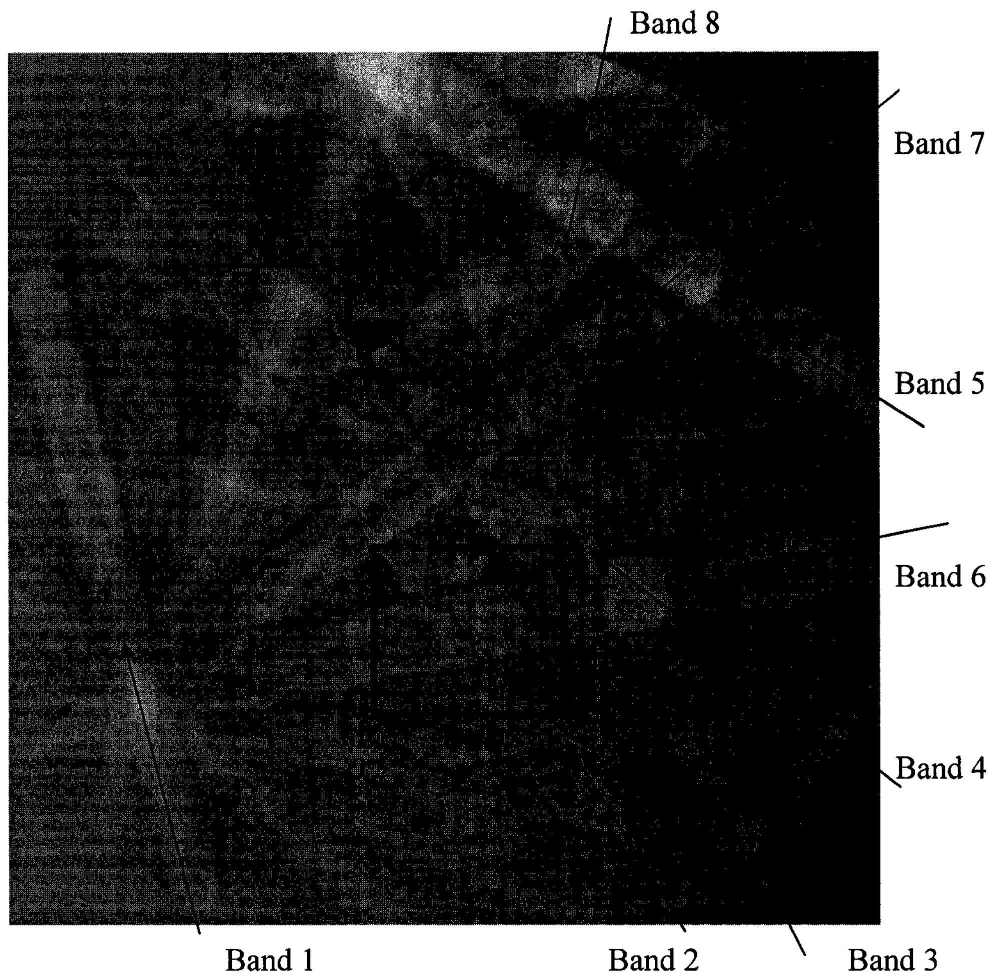

Figure 4.13. An EBSD pattern captured from a silicon wafer. This pattern has 987×987 pixels and the effective pixel size is about 35 μ. Through shifting the electron beam to known distances (Figure 4.15) and then measuring the shift of zone axes and Kikuchi bands (marked by arrows), we can test the validity of the algorithm. The shift of the zone axis marked by the red rectangle is also measured.

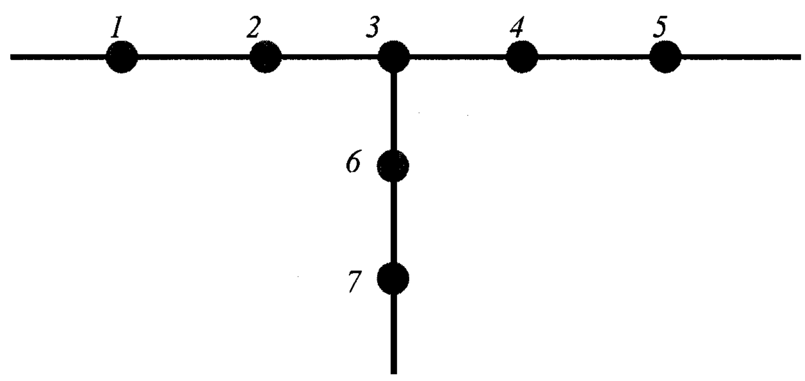

Figure 4.14. Beam shifting procedure (with reference to Figure 4.14) used to test the validity of the software. The distances between adjacent points are about 11 μ.

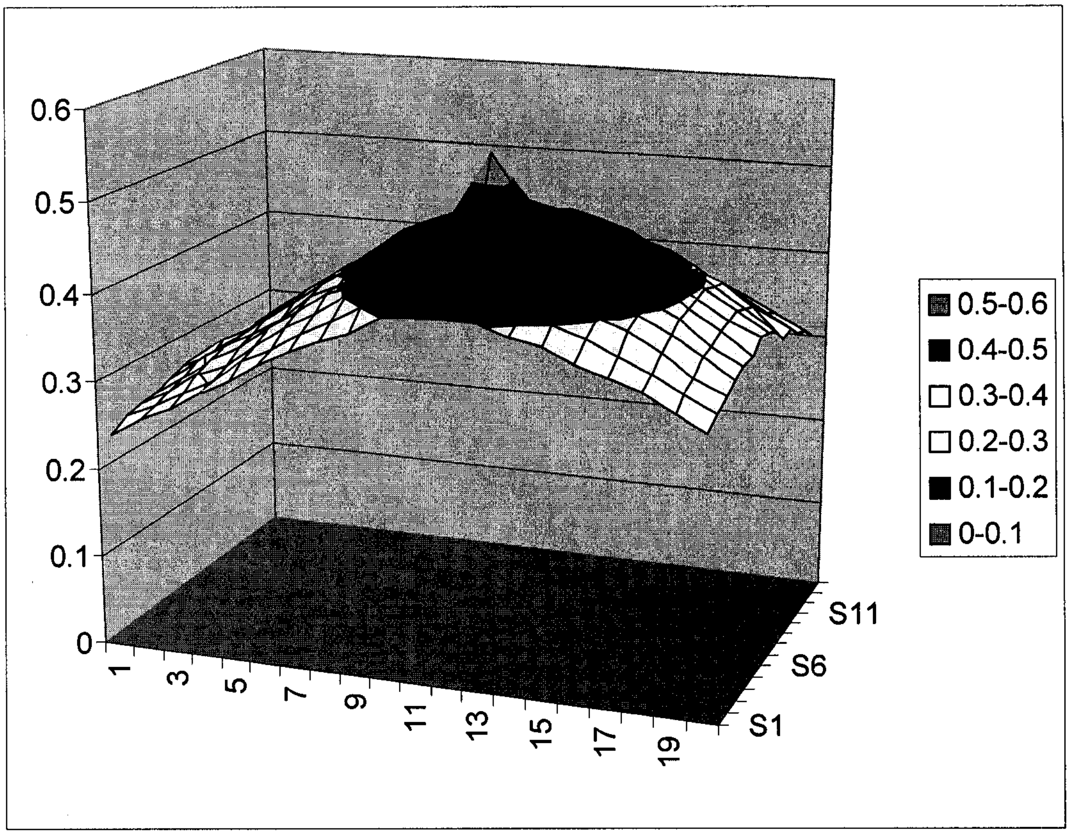

Figure 4.15. Measuring the shift of the zone axis (in image space) cannot detect the shift of a zone axis accurately. The calculated shift value should be about (1.4, 0). However, the measured value is (0,0) when choosing not to use interpolation and the value is meaningless when using interpolation.

Table 4.1. Result of the integrity test for Revised OIM Data Collection Software. The cross correlation coefficient is used as criterion.

	Band 1	Band 2	Band 3	Band 4	Band 5	Band 6
θ	*29°*	*90°*	*146°*	*122°*	*133°*	*58°*
Calculated Shift (Pixel)	-1.3594	-1.0000	0.2698	-0.3181	-0.0494	-1.3780
Measured Shift (Pixel)	-1.391	-0.998	0.282	-0.279	-0.037	-1.362

Table 4.2. Result of the integrity test for **ShiftDetector.**

	Zone Axis 1	Zone Axis 2	Zone Axis 3
Nominal Shift (x,y)	1,1	1,1	1,1
*Detected Shift (Cross Correlation)	1,1	1,1	1,1
Detected Shift (Phase Correlation)	1.005, 0.994	1.007, 0.993	0.992, 0.999

* Interpolation method was not used here.

Table 4.3. Result of the integrity test for Revised OIM Data Collection Software on a noisy EBSD pattern (Figure 4.12).

	Band 1	Band 2	Band 3	Band 4	Band 5
θ	*110°*	*86°*	*136°*	*175°*	*34°*
Calculated Shift (Pixel)	1.2817	0.9278	1.4140	1.0834	-0.2698
Measured Shift (Pixel)	1.208	0.953	1.401	1.060	-0.239

//Equation: $Y_{shift}*\sin\theta - X_{Shift}*\cos\theta$). $Y_{shift} = 1$; $X_{Shift} = 1$.

4.3.1. Measurement in the Image Space

Figure 4.13 is an EBSD pattern captured from the Si wafer sample mentioned above. The Kikuchi bands chosen to have their shifts measured are marked on the pattern and so is the chosen zone axis. The preliminary results showed that neither the cross correlation nor the phase correlation method can detect the shift of the Kikuchi zone axis correctly in most cases. Usually, the shift is invariantly **0** in both x and y directions when no interpolation method is used and the measurement tends to be meaningless if choosing to use interpolation. This is in contradiction to the results of Wilkinson [28]. The plot of the cross correlation coefficient as a function of displacement shows there is a relatively large peak at exactly the (0,0) position, shown in Figure 4.15. This chart also shows that the value of the cross correlation coefficient is relatively small even for the maximum value. i.e. the best fit, so is the phase correlation. This means the similarity between the selected areas in the two patterns used for comparison is quite low.

After checking the calculation for another experiment (zone axis two in Figure 4.11), in which the electron beam is shifted several pixels from the reference point, we found that, on the plot of cross correlation coefficient, there is a high plateau corresponding to (0,0) shift and a second peak corresponding to the shift of the selected area basically, shown in Figure 4.17 and Figure 4.18. The 3-d display of the Phase correlation image also showed these two peaks, the larger peak corresponding to the (0,0) shift and a very small second peak corresponding to the shift of the selected zone axis. The second peak usually has a very small phase correlation value and a relatively small cross correlation coefficient. Figure 4.16 shows an image formed by the cross correlation coefficient. The bright single pixel corresponds to the center of the image, while it has an offset from the center of the bright blobs.

If the distance between the first peak and the second peak is too small, as in Figure 4.15 shows, the interpolation to sub-pixel level for the second peak is usually meaningless. Since both the value of cross correlation coefficient and phase correlation are small and the cross correlation and phase correlation dataset is noisy, the accuracy of the interpolation could also be affected.

We are not sure the exact reason for the formation of this (0,0) shift peak. One possible explanation is the residual background. Since the cross correlation coefficient is a "statistical factor", all the pixels in the chosen area are features and their effects are counted. The residual background on the EBSD pattern works as a "feature", this causes the large peak at (0,0) place. However, we don't know the exact reason why this center peak is so sharp. In Wilkinson's research, the distance between the camera and the sample is large and the EBSD pattern covers a small solid angle, so the width of the Kikuchi bands is large and the chosen zone axis covered more features and less background. He also used very long exposure time to suppress the effect of noise. As a result, the (0,0) peak is not reported in his research. Although he acknowledges seeing such a peak and discarding it as an artifact (private communication).

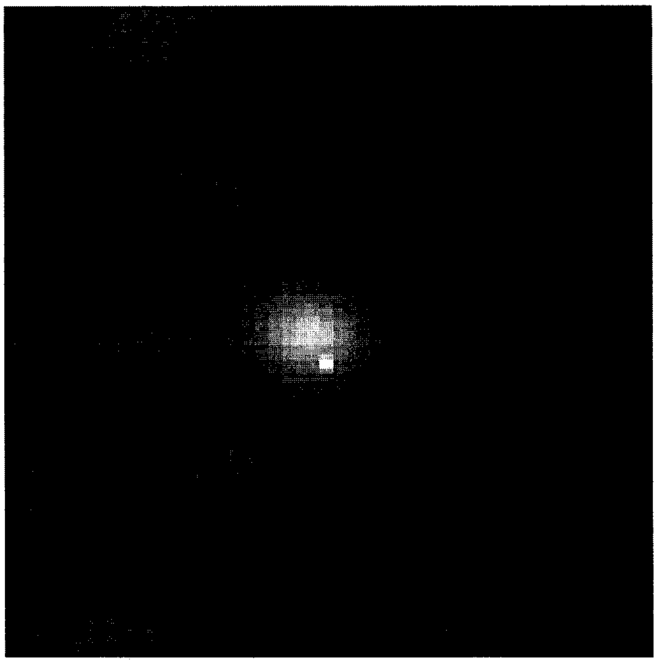

Figure 4.16. Map of the cross correlation coefficient for detecting the shift of a zone axis. The very small, very bright point in this Figure corresponds to the (0, 0) peak, which is different from the center of the broad blob. The center of the broad blob corresponds to the shift of the zone axis.

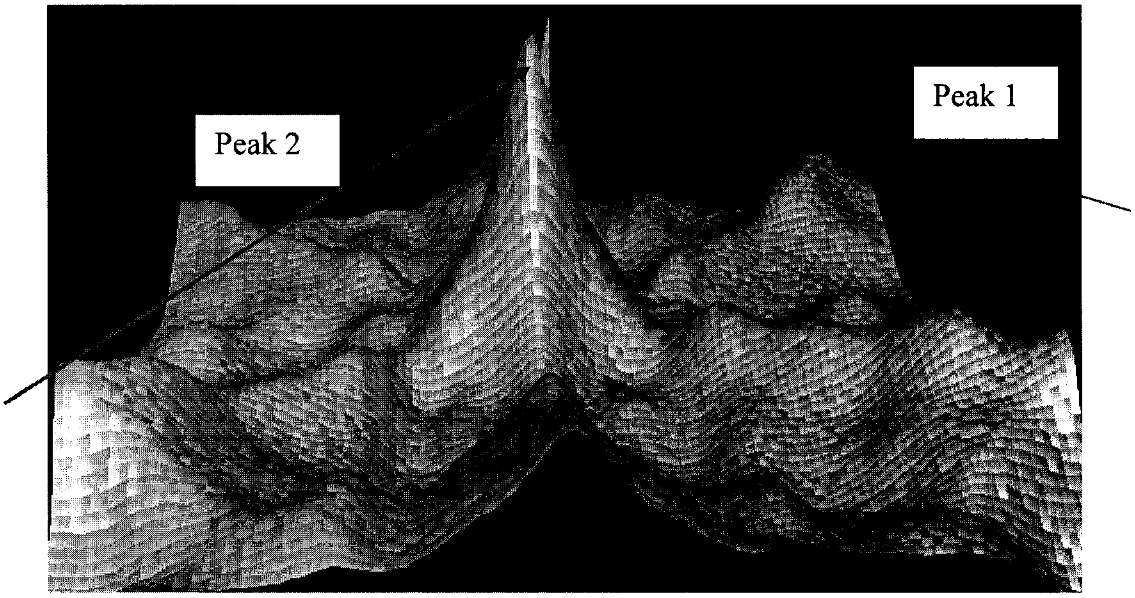

Figure 4.17. The highest peak (peak 1) corresponds to the (0,0) shift. The second peak (peak 2) corresponds to the shift of the zone axis. Both peak 1 and peak 2 have a relatively low cross correlation coefficient.

Our experiment shows calculating the cross correlation coefficient directly (without using the Fourier transform) cannot eliminate the center peak. This excludes the reason that the sharp (0,0) peak is introduced through the Fourier transform. Thus, most possibly, the bright center peak is caused by the residual background. Since the calculation of the cross correlation coefficient is also a statistical process, all the pixels in the chosen area are considered as the feature, including the zone axis, noise and background. Besides, using a Gaussian de-blur filter or a high pass filter can not eliminate the zero shift peak for the experiment setup in our research. However, the radius of the filter can affect the relative height between the first peak and the second peak.

The EBSD patterns are usually very noisy and have low contrast even after long pattern integration time. So, the value of the phase correlation and cross correlation coefficient is relatively low.

Considering these facts, interpolation of the measured shift to sub-pixel level and further mapping of the shift of the zone axis is meaningless.

4.3.2. Shift Measurement in the Hough Space

For the hardware configuration in this research, the CCD chip is lens coupled to the Phosphor screen, so the actual CCD pixel size is different from the "effective" one. The phosphor screen in this experiment setup has a diameter about 3.8cm (estimation), and we choose not to bin the diffraction pattern on both the hardware and software level.

As a result, one EBSD pattern has 987×987 pixels and the pattern covers about 90% of the phosphor screen. So, the effective pixel size is about 35μ.

Using the procedure described in the previous section, we measured the shift of eight Kikuchi bands, marked by the arrows in Figure 4.13. For each target point, we acquired two EBSD patterns, thus we have two sets of measurement data. For the horizontal points in Figure 4.14, **Pattern1a** is used as the reference and the results are listed in Table 4.4. The largest difference between the values measured from the two patterns captured at the same point is 0.17 pixels, and the average difference is 0.063 pixels.

In this experiment, each selected "Hough peak", which is used to do the cross correlation, has an angular width (θ) ranging from 10 to 20 degrees. The θ value for the centerline of the Kikuchi band, θ, is listed on the second row in table 4.4.

Because we could not devise a good way to calibrate the actual pixel size in the EBSD pattern, the shifts were measured only in relative terms by assuming that the correct value was obtained for the largest shift. It was later shown that the value was in good agreement with the estimated pixel size, obtained by measuring the diameter of the phosphor screen. The point is that we can obtain the angular size of one pixel from the pattern calibration, but shifting the beam produces a displacement of the pattern whose size in pixels depends on the (unknown) magnification of the lens coupling from the phosphor screen to the camera.

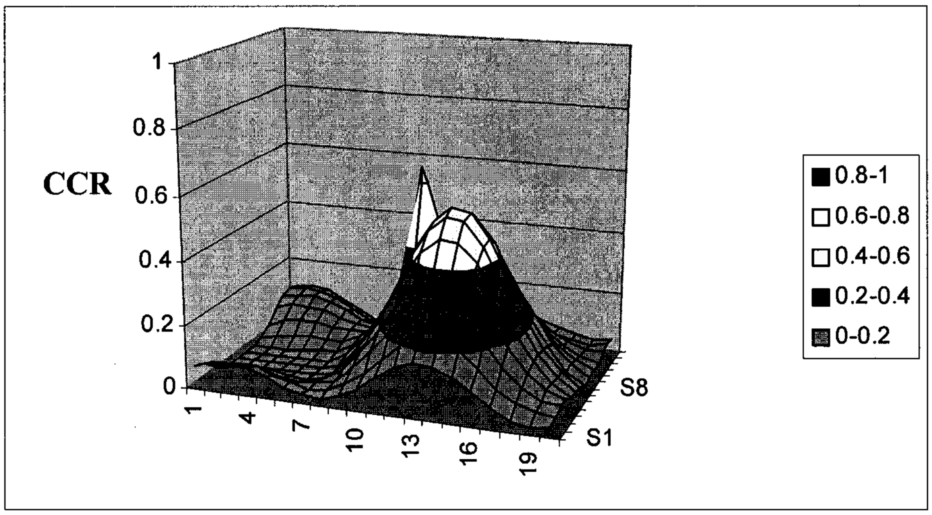

Figure 4.18. Measuring the shift of a zone axis in image space. The second peak corresponds to the shift of the zone axis. It has a relatively low cross correlation coefficient.

Approximately, for horizontally shifting the electron beam, the displacement of the beam (in units of pixels) can be calculated by dividing the shift of the band by $cos\theta$. The measured shift of band 1 and band 8 at point 5 are used to calculate the largest horizontal beam shift.

Horizontal Beam Shift = $0.5\times(\text{Band1}/cos\theta_1 + \text{Band8}/cos\theta_8)$. 6)

After the largest beam shift (horizontally) is known, which is 1.38 pixels in this case, we further calculated the shift of the Kikuchi band for each point and compare it with the measured one (averaged over two measurements). The results are listed in Table 4.5 and Figure 4.19 shows the comparison. The x-axis on this Figure stands for the measured shift, while the y-axis is the calculated shift. Every point on the reference line has the same distance to both x and y axes. This Figure shows that the measured shifts are in good agreement with the calibrated value, since nearly all the points are clustered around the reference line. The largest discrepancy is 0.145 pixels and the average discrepancy is 0.06 pixels.

The results of this experiment (Table 4.5 and Figure 4.19) proved: 1). The measured pixel size (32μ) is quite similar to our estimated effective pixel size (35μ). 2). For the same points, the measurement for the patterns captured at different times shows good consistency and their difference is less than 0.1 pixel. 3) Our image processing routine could reach sub-pixel resolution when being used to detect the shift of the Kikuchi bands in an EBSD pattern. Our estimate is that an accuracy up to 0.2 pixels can be reached for most bands, which corresponds to angular difference about 0.02 degree. However, it is difficult to give an absolute value on the detection limit of this method, since the results depend on materials, hardware set up, background elimination and some other factors.

However, the measurement for the vertical shift of the electron beam is not as good as that of horizontal shift of electron beam. Table 4.6 lists the measurement of the shift of the eight Kikuchi bands marked by arrow on Figure 4.13, for the vertical points in Figure 4.14. In this measurement, Point3a is chosen as the reference pattern. The shift of the Kikuchi bands, in units of pixels, is calculated using the shift of the beam, the θ value of the Kikuchi band and the measured effective pixel size (32μ). Table 4.7 lists the average of the two measurements and the results of calculation. Figure 4.20 shows the comparison between the measurement and the calculation. It is clear that the errors are relatively large between the measurement and calculation and the measurement is systematically smaller than the calculated values. Possible reasons include:

1) The experiment was done under low magnifications, and the sample is highly tilted. So, a shift of the electron beam along the y scanning direction corresponds to a large value of out of focus. As a result, the diffraction volume for Point 6 is quite a lot larger than that of Point 3 and the Kikuchi bands on the EBSD patterns from Point 6 are relatively blurry and wider than those from Point 3. This could be the main reason for the measurement errors.

2) In some cases we observed that the contamination patch was not rectangular indicating an error in the angle of the scan. This could also lead to larger errors for the measurement of the vertical shifting than that for the horizontal shifting.

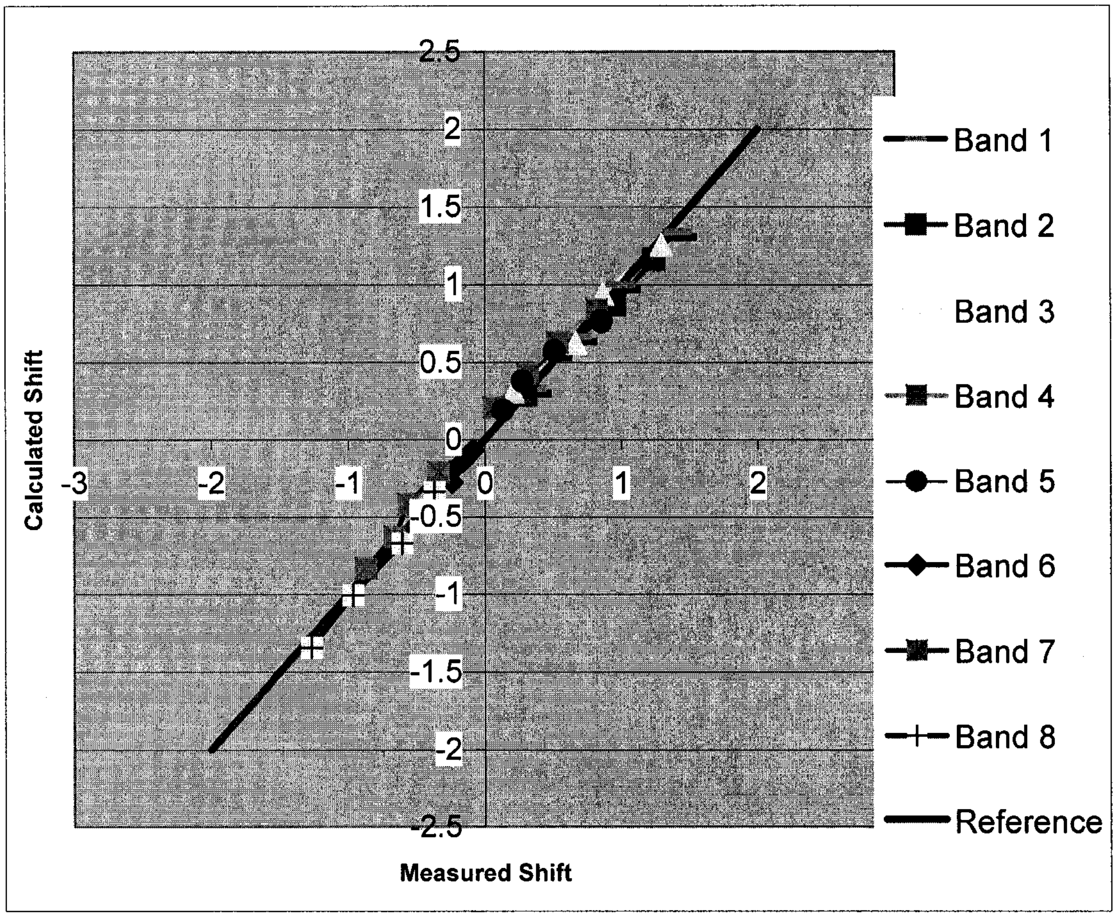

Figure 4.19. This Figure shows, for horizontal shifting of the electron beam, that the measured shift of the electron beam using our proposed method is in good agreement with the calibrated shift. All of the units are in pixels.

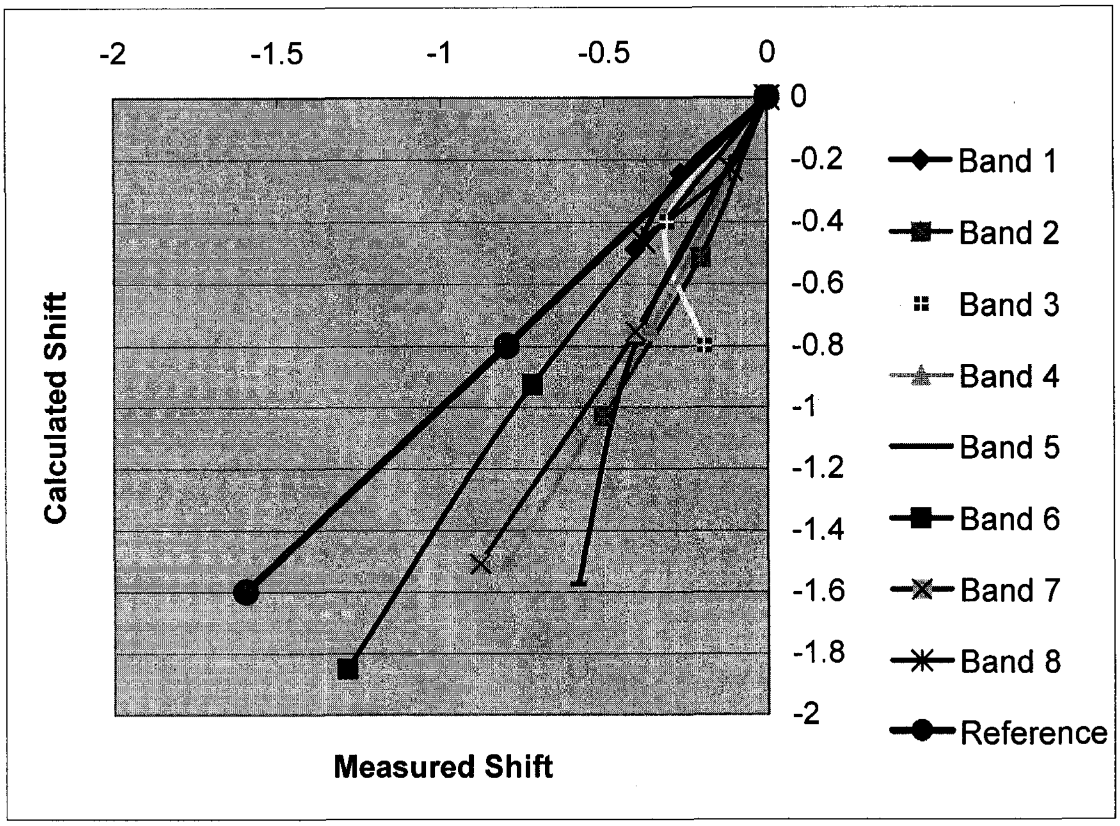

Figure 4.20. This Figure shows, for vertical shifting of the electron beam, that the measured shift of the electron beam is not as good as that for the measurement of the horizontal shifting of the electron beam.

Table 4.4. Measurement of the shift of the Kikuchi bands

	Band 1	**Band 2**	**Band 3**	**Band 4**	**Band 5**	**Band 6**	**Band 7**	**Band 8**
Center θ	***15***	***33***	***25***	***52.5***	***56.5***	***101.5***	***127***	***166***
Pattern 1b	*0.094*	*0.077*	*0.003*	*-0.070*	*-0.007*	*0.014*	*-0.065*	*0.038*
Pattern 2a	0.345	0.283	0.222	0.068	0.159	-0.065	-0.272	-0.425
Pattern 2b	0.348	0.318	0.193	0.062	0.110	-0.107	-0.408	-0.317
Pattern 3a	0.647	0.564	0.587	0.362	0.267	-0.126	-0.557	-0.616
Pattern 3b	0.709	0.547	0.745	0.265	0.284	-0.198	-0.565	-0.599
Pattern 4a	0.989	0.866	0.788	0.450	0.501	-0.305	-0.660	-0.921
Pattern 4b	1.006	1.036	0.939	0.614	0.516	-0.193	-0.668	-1.013
Pattern 5a	1.405	1.228	1.251	0.761	0.827	-0.276	-0.907	-1.284
Pattern 5b	1.412	1.251	1.335	0.871	0.882	-0.209	-0.838	-1.257

All of the Units in this table are in pixels. From point 1 to point 5, the beam shift distance is about 44μ, which corresponds to 1.38 pixels according to our measurement. So the effective pixel size is about 32μ.

Table 4.5. Comparison of the measurement and calculation for the shift of the Kikuchi bands (horizontal shifts)

	Band 1	Band 2	Band 3	Band 4	Band 5	Band 6	Band 7	Band 8
Pattern 2(C)	0.334	0.290	0.313	0.211	0.191	-0.069	-0.208	-0.336
Pattern 2(M)	***0.346***	***0.301***	***0.207***	***0.066***	***0.134***	***-0.086***	***-0.340***	***-0.371***
Pattern 3(C)	0.668	0.581	0.627	0.421	0.382	-0.138	-0.417	-0.672
Pattern 3(M)	***0.678***	***0.555***	***0.666***	***0.313***	***0.276***	***-0.162***	***-0.561***	***-0.608***
Pattern 4(C)	1.003	0.871	0.940	0.632	0.573	-0.207	-0.625	-1.007
Pattern 4(M)	***0.998***	***0.951***	***0.864***	***0.532***	***0.509***	***-0.249***	***-0.664***	***-0.967***
Pattern 5(C)	1.337	1.161	1.254	0.844	0.765	-0.275	-0.833	-1.342
Pattern 5(M)	***1.408***	***1.239***	***1.293***	***0.816***	***0.855***	***-0.243***	***-0.872***	***-1.271***

(C): Calculated shifts of the Kikuchi bands using the shift of the beam and the θ value of the Kikuchi band.
(M): Measured shifts of the Kikuchi band using our image processing routine. The results are the average over two measurements from two different EBSD patterns from the same point.

3) The error associated with the inaccuracy of the beam shifting has a larger effect (a factor of 3) on vertical points than horizontal points, since the sample is highly tilted (70°).

For both the shifting of the electron beam horizontally and vertically, errors can also be brought in by the effect of charging and beam shift, since long pattern capturing time is used in this experiment.

The aim and function of each experimental step is explained below:

Gaussian Filtering: The aim of this step is to remove the residual background from the diffraction pattern and eliminate the uneven grayness scale in the Hough transform. In our early work, we used the Gaussian Blur function of Photoshop®, and chose an appropriate radius value (about 20-30, depending on the quality of the pattern). This heavily blurs the diffraction pattern until no details can be seen. Then we subtract this image from the original image. Sometimes we need to cut the top 20-40 pixels. These two functions can be done in one step, as High pass filtering in Photoshop®. Later, we wrote a program ourselves to do this filtering.

Experiment shows this step is not necessary for most cases. With no pre-filtering of the EBSD pattern, we can save calculation time and decrease the effect of the noise. However, the calculation can be slightly affected by the residual background.

Hough transform: Since we are interested only in a small shift of the peaks in Hough space, we do the initial Hough transform using a binned image. We then recalculate the Hough transform without binning, just for those areas surrounding the peaks, which correspond to Kikuchi bands in image space. In this way, we can greatly decrease calculation time.

Our aim is to detect the shift of the peak to a sub-pixel level; so, our revised Hough transform should use small sampling intervals (high sampling frequency). A step size of $\Delta\theta = 1/8$ degrees and $\Delta\rho = 1$ pixel is a reasonable choice for the calculations in our revised Hough transform.

Cross correlation coefficient: The Cross Correlation (coefficient) can be calculated through a Fourier transform. This approach is fast for a large dataset. It can also be calculated directly, which is easy to understand. In this research, we implemented both methods and our calculation shows there is no big difference between the calculations. Specifically, when we choose the direct method, Figure 4.21, the template window is the dataset calculated from the reference pattern shown above. Move this template window one pixel by one pixel in a somewhat larger area in the Hough space of the target pattern, as shown in Figure 4.22. This frame in Figure 4.22a shifts one unit by one unit in Figure 4.22b, which is part of the Hough transform of the target pattern. At each position, the cross correlation coefficient is calculated and saved. Since there is no rotation and skewing involved in Hough space, our implementing algorithm is comparatively simple. Under most conditions, the position where we get the largest cross correlation coefficient corresponds to the shift of the "template window" in the Hough space of the target pattern. That is, the shift of Kikuchi bands approximately.

Curve fitting: The aim of this step is to interpolate the calculated data to the sub-pixel scale. First, we find the position where the largest cross correlation coefficient appears.

Then, we suppose a smooth curve connecting this point to its four nearest points along the ρ direction. In our preliminary work, we further assume this curve is a parabola. By using a minimum least square fitting method, we can find the exact form of this parabola. Next, by interpolating, we calculate the position where we get the maximum value of cross correlation coefficient. This value is assumed to correspond to the shift of the peak in the Hough space of the target pattern, i.e. the shift of the Kikuchi band of the target pattern with respect to the same band in the reference pattern. This part of calculation is implemented under the framework of the OIM Data Collection system. The main interface is shown in Figure 4.23. This not only works for single patterns, this program can also be used to map the shift of the Kikuchi bands.

We expect that a precision of about a fifth of a pixel could be achieved by these methods. This corresponds to a change of orientation of the planes (at the same location) of 0.15 mrad. Similar results are also acquired from Noran's Phase ID system installed on a Field Emission gun SEM, JSM 6300 (JEOL). This EBSD system uses a slow scan CCD camera with a pixel size about 25μ. 20kV and 40s collection time were used.

Table 4.6. Measurement of the shift of the Kikuchi bands for the vertical shifts

	Band 1	**Band 2**	**Band 3**	**Band 4**	**Band 5**	**Band 6**	**Band 7**	**Band 8**
Center θ	***15***	***33***	***25***	***52.5***	***56.5***	***101.5***	***127***	***166***
Pattern 3b	0.074	0.004	0.13	-0.088	0.0278	-0.072	0.002	0.002
Pattern 7a	-0.234	-0.226	-0.325	-0.393	-0.414	-0.695	-0.381	-0.176
Pattern 7b	-0.300	-0.190	-0.294	-0.327	-0.393	-0.747	-0.43	-0.054
Pattern 8a	-0.355	-0.393	-0.149	-0.671	-0.441	-1.241	-0.773	-0.496
Pattern 8b	-0.461	-0.614	-0.245	-0.916	-0.724	-1.339	-0.992	-0.273

Table 4.7. Comparison of the measurement and calculation for the shift of the Kikuchi bands (vertical points)

	Band 1	**Band 2**	**Band 3**	**Band 4**	**Band 5**	**Band 6**	**Band 7**	**Band 8**
Pattern 3	0	0	0	0	0	0	0	0
Pattern 7(C)	-0.244	-0.514	-0.399	-0.749	-0.788	-0.925	-0.754	-0.228
Pattern 7(M)	**-0.267**	**-0.208**	**-0.310**	**-0.360**	**-0.404**	**-0.721**	**-0.406**	**-0.115**
Pattern 8(C)	-0.488	-1.028	-0.798	-1.499	-1.575	-1.851	-1.509	-0.457
Pattern 8(M)	**-0.408**	**-0.504**	**-0.197**	**-0.794**	**-0.583**	**-1.290**	**-0.883**	**-0.385**

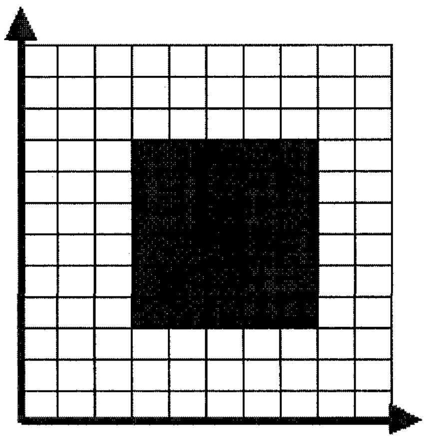

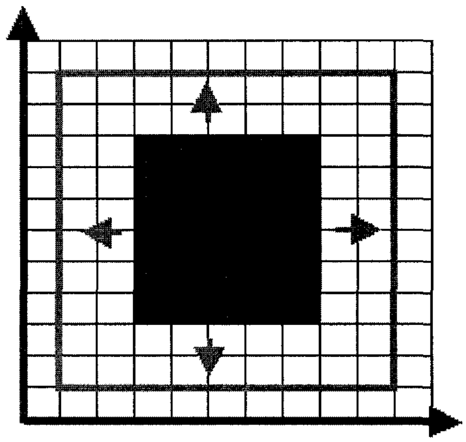

Figure 4.21. Illustration of the process of template window fitting. The solid rectangle in the left Figure has the same size as that in the right Figure. It is moved one pixel by one pixel inside the open square. At each position, the cross correlation coefficient is calculated.

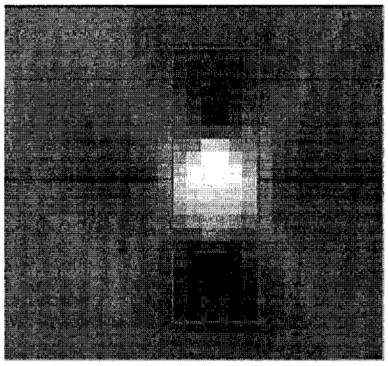

Figure 4.22a.

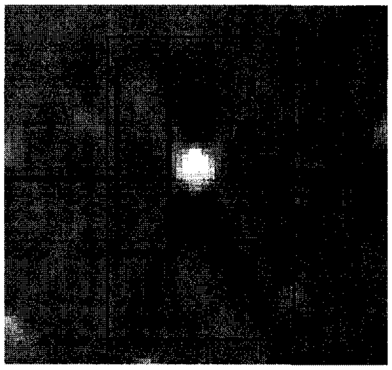

Figure 4.22b

Figure 4.22. Calculating the cross correlation.

The bright blobs in the center of these two Figures are the Hough transform of the Band 2 in Figure 4.11. The frame in Figure 4.22a corresponds to the inner frame in Figure 4.22b. Shift this rectangle area one pixel by one pixel in the larger rectangle area framed by the outer frame in Figure 4.22b. This is the direct calculation of the cross correlation coefficient. The cross correlation coefficient can also be calculated using a Fourier transform.

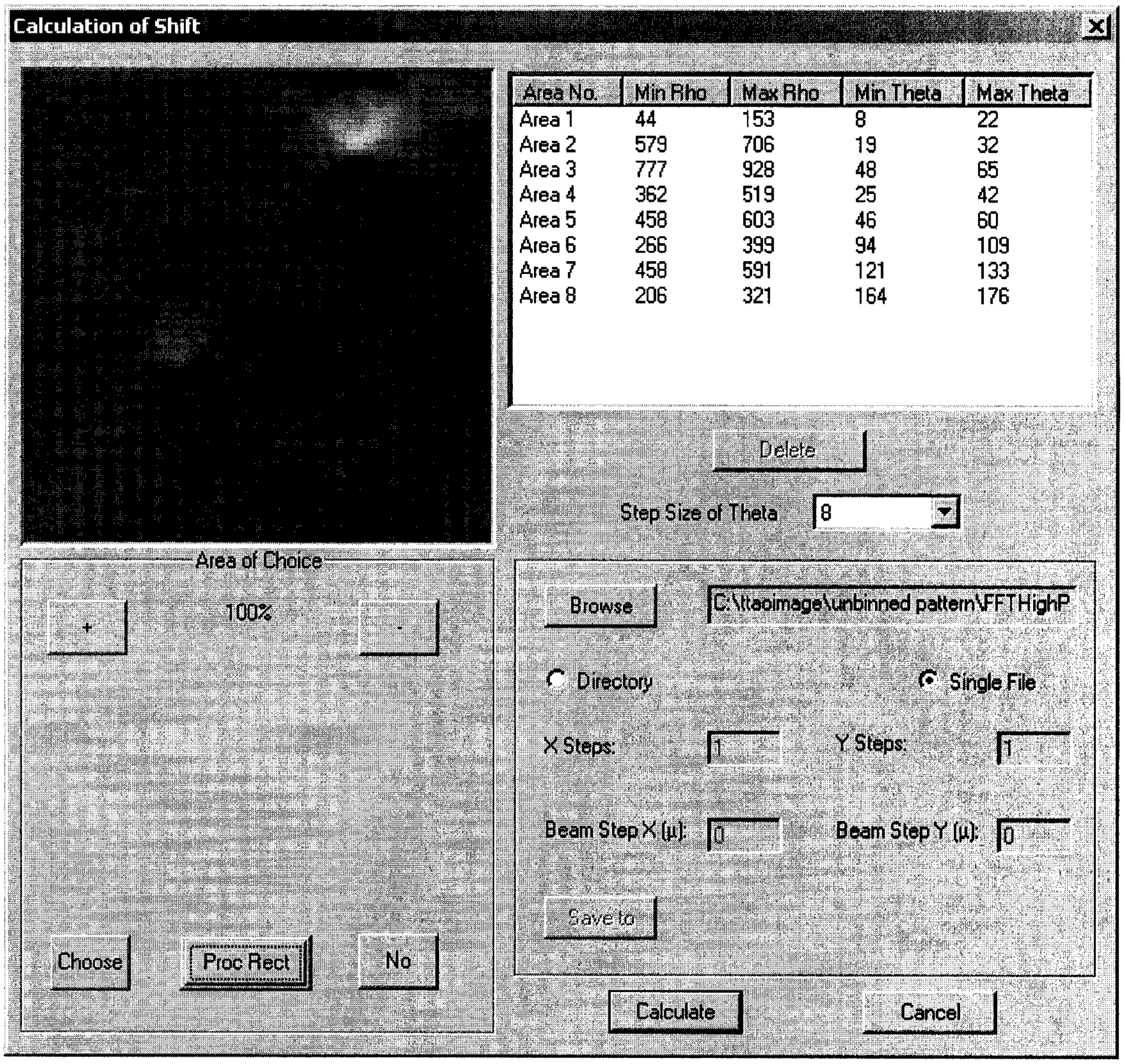

Figure 4.23. Main interface for our revised program on calculating the cross correlation coefficient.

4.3.3. Comparison of the Measurement in Image Space and Hough Space

Our results showed that measuring the small shift of Kikuchi bands in Hough space is more advantageous than measuring the shift of the zone axis in image space for normal EBSD. There are several reasons for this:

1). The former method gave a high cross correlation coefficient value and thus the interpolation is more accurate and meaningful. Figure 4.15 shows the cross correlation coefficient from the calculation of the shift of a zone axis, while Figure 4.24 shows the cross correlation coefficient from the calculation of the shift of a Kikuchi band. For most of the experiments in our research, the largest cross correlation coefficient is less than 0.7 when we started detecting the shift of the zone axis. In most cases, it is less than 0.5. However, the largest cross correlation coefficient for detecting the shift of the Kikuchi band is larger, in most cases, it is larger than 0.9.

2). The Hough transform can be understood as an accumulation process, so the effect of noise is suppressed and the effect of "residual background" is minimized since the cross correlation coefficient is calculated on only the peak of the Hough transform corresponding to the Kikuchi band. Figure 4.25 and 4.26 show the intensity distribution of the Kikuchi band 2 in Figure 4.11 at the place A-A' and B-B separately. Although this Figure does show the general shape of the curve, there is a lot of noise. However, if we measure the intensity distribution of band A in Hough space, the effect of noise is suppressed, as shown in Figure 4.27 Even for a very noisy EBSD pattern as Figure 4.28, the intensity distribution of a Kikuchi band (marked by arrow) is very smooth if measured in Hough space, shown in Figure 4.29.

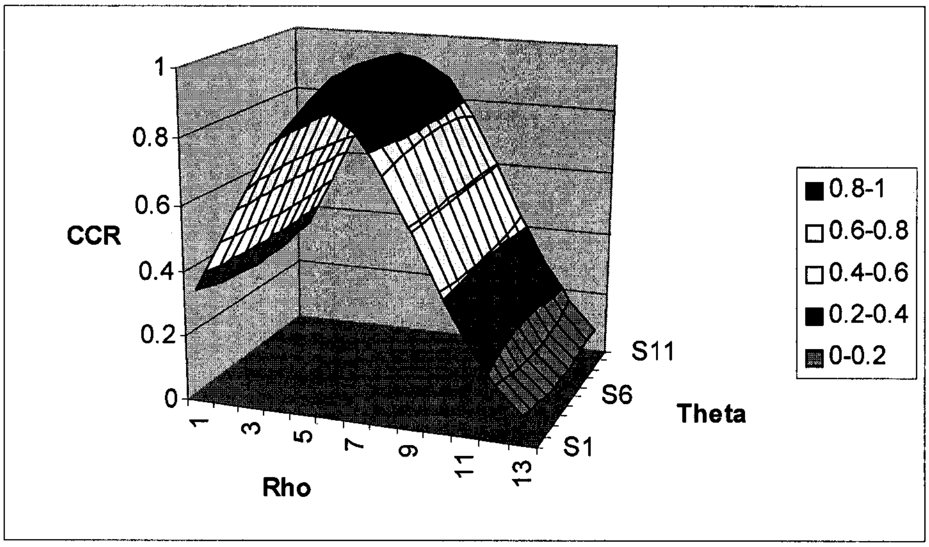

Figure 4.24. Measurement of the shift of a Kikuchi band in Hough space. The curve is smooth along the Rho (ρ) direction. Around the peak area the cross correlation coefficient is large (>0.9).

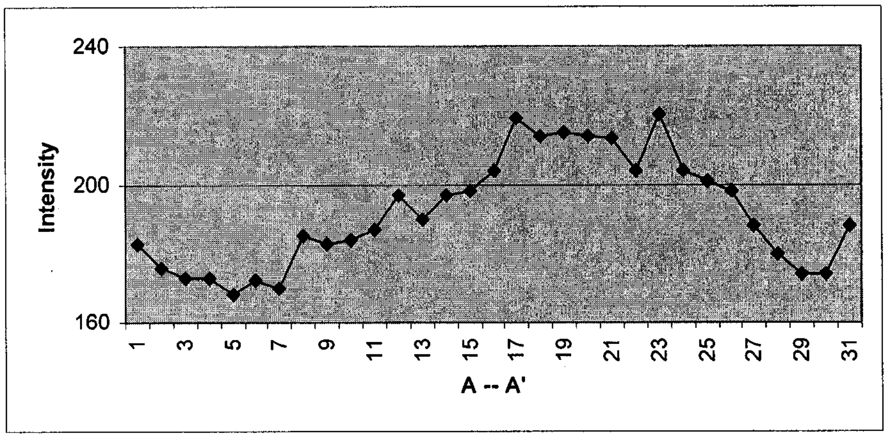

Figure 4.25. Intensity distribution of the Kikuchi band 2 in Figure 4.11, at the place A-A'.

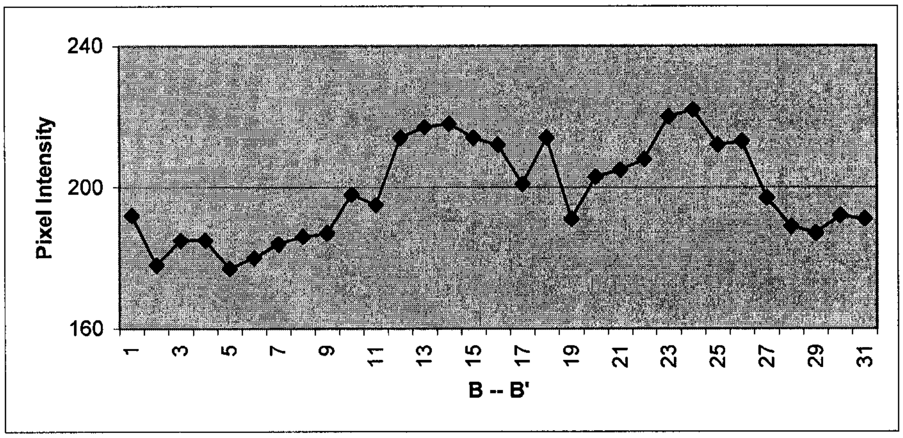

Figure 4.26. Intensity distribution of the Kikuchi band 2 in Figure 4.11, at the place B-B'.

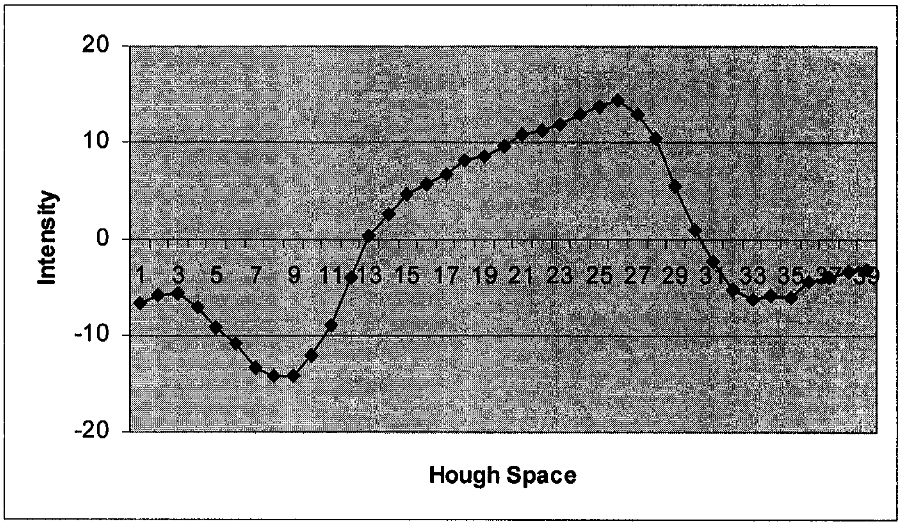

Figure 4.27. Intensity distribution of the Kikuchi band 2 in Figure 4.11, Measured in Hough space. Compare this Figure with figure 4.25, and figure 4.26.

3). Measuring the shift in Hough space doesn't require any change of the experimental settings, and a much shorter exposure time is needed. Thus mapping is feasible. Besides, the shift of several bands can be measured at the same time when choosing to use the band detection method. By contrast, Wilkinson's work on detection of axis shift required moving the EBSD system, long exposure times and could acquire the data only at selected points and the EBSD patterns covered a very small solid angle, as a result only a few zone axes are useful. However, these are not true for measuring the shift of the zone axis. The Kikuchi band in Hough space gave a larger cross correlation coefficient value than measuring the shift of the zone axis.

4). Pre-filtering is not necessary for measuring the shift of the Kikuchi bands in Hough space, while it is necessary for the measurement of the zone axis in image space, according to Wilkinson. Through skipping this step, we can decrease calculation time noticeably.

Measuring the shift of the Kikuchi bands can reach sub-pixel accuracy. This fact can be utilized to do a "high precision" orientation mapping. The conventional method of orientation mapping relies on indexing the EBSD pattern and then measuring the absolute orientation of the sample. Inevitably, this method suffers from low precision.

As a complement, we propose a way to do it differently. This method is based on the fact that detecting the relative change of the orientation is more accurate than measuring the absolute value. So, high precision orientation mapping can be done this way: First, we perform a conventional orientation mapping (or just map the standard deviation), then we choose a reference point from each grain, and measure the relative orientation change of all other points in this grain from this reference point. The orientation changes can be easily calculated using measured shifts of several Kikuchi bands. Finally, using the orientation index of the reference points and the measured orientation shift for other points, we can re-build an orientation map, at a higher precision.

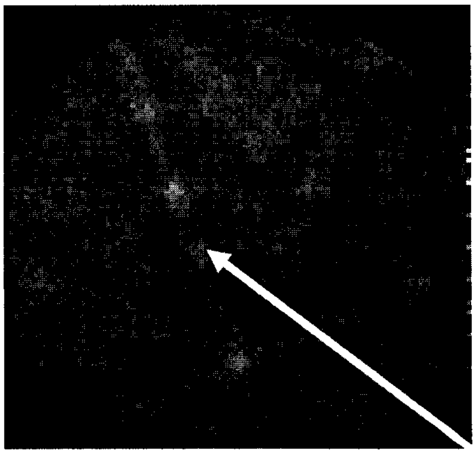

Figure 4.28. A noisy EBSD pattern, captured from polycrystalline Ni. 0.26s pattern integration time.

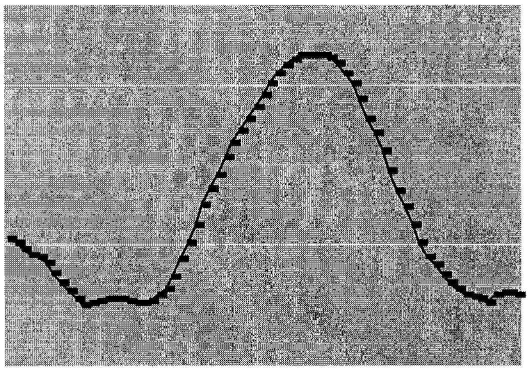

Figure 4.29. Intensity Distribution across band A in figure 4.28, averaged and measured in Hough space.

4.3.4. Summary of This Section

In this section (Ch4.3), we showed and compared two image processing methods.

We designed an image processing procedure, which can enable us to detect the shift of Kikuchi bands to its limit, and this function is added to the OIM orientation program. This shift detection procedure is done in Hough space (using our revised Hough transform, "weighting the points" form) and the cross correlation coefficient is used as the criterion. In addition, we used interpolation to reach sub-pixel accuracy. Experiments using an artificial image show there is no problem with the calculation. Trial experiments using single crystal silicon wafer and moving the electron beam to known distances show this method can reach 0.2 pixel resolution.

We also wrote a program to detect the shift of zone axes of the EBSD pattern. Both the cross correlation and phase correlation are used as criteria. Experiments using an artificial image show there is no major problem with the calculation. However, a trial experiment shows this method failed to detect the small shift of the zone axis. Experiment shows there is a relative high zero shift peak, which affects the accuracy of the shift detection of the zone axis.

Comparisons between these two shift detection methods are given. We found detecting the shift of Kikuchi bands in Hough space has advantages over detecting the shift of zone axes in image space. Besides, suggestions are also given on making a "high precision" orientation map.

4.4. INTENSITY MAPPING

4.4.1. IQ, Mean, Standard deviation and Entropy

There is value to assessing the quality of EBSD patterns. A better pattern gives a more reliable determination of the sample orientation. A map of image quality, therefore, can reveal areas in which the orientation data is suspect. Commercial software evaluates a parameter designated “IQ” (Image quality) or PQ (pattern quality), which is used to make such a map. The IQ parameter uses the intensity information of the EBSD pattern indirectly; it is calculated from the height of the peaks in the Hough transform. However, the value of IQ is somewhat arbitrary. We recommend using the intensity information of the EBSD patterns directly. That is we treat the combination of CCD camera and phosphor screen as a special BSE detector, this BSE detector may not be as effective as a semiconductor BSE detector, but it covers a large solid angle and we can use long exposure time to compensate the possible low detector efficiency. It is also well known that this special BSE detector is sensitive to low loss BSEs, which seems favorable to our aims. Besides, if using a CCD camera as a BSE detector, we can monitor the intensity distribution specifically for one band, one zone axis or any kind of combination of them. Since the strain field of dislocations not only shifts the Kikuchi bands in EBSD patterns, but also changes the intensity distribution of the diffraction bands, as in the case of electron channeling patterns [3]. Thus, the intensity distribution inside or around one or more bands contains information about the dislocations and strain fields. So we defined several factors, such as the mean of the band (zone axis) and standard deviation of the band (zone axis). In order to minimize the effect of the topographic contrast and hydro-carbon contamination, we also defined the other factors, such as the mean of the band (zone axis) divided the mean of the pattern and the standard deviation of the band (zone axis) divided the standard deviation of the pattern. In order to simplify the programming process, we chose Kikuchi bands or zone axis in the reference pattern only. This means the selected areas, which correspond to certain zone axes or Kikuchi bands on the reference pattern, could be areas, which do not match any Kikuchi bands or zone axis on other patterns, especially for a polycrystalline sample.

Finally, we used large scanning step size, medium step size and small step size and different samples to test the intensity mapping method separately.

Experiment 1. Large Scanning Step size. A Polycrystalline Ni sample was used for this experiment. A FEI XL30 ESEM with a W filament was used. The EBSD system was a TSL OIM system installed with a SIT Camera. A large scanning step size (0.5μ) was used. The pattern capturing time was about 0.26s/point: One set of EBSD patterns (121×141) are recorded and analyzed offline. Each pattern has 480 × 480 pixels.

Figure 4.30a is a secondary electron (SE) image of the polycrystalline Nickel sample; the foreshortening along the vertical direction is corrected through using digital image-processing. Most of the features in this image are dirt. Figures 4.30b, 4.31a and 4.31b are the images formed by the mapping of the mean, standard deviation and entropy respectively. Figure 4.31c is the IQ map and Figure 4.32 is the inverse pole figure map. Even though the secondary electron image, Figure 4.30a, and the map of the mean, Figure 4.30b, are different in the shadowing direction of the dirt, both of them show topographic contrast and similar details of the specimen. The map of the entropy, Figures 4.31a, and the map of the standard deviation, Figure 4.31b, show the grain boundaries clearly and weak diffraction contrast between grains.

Typically, the histogram of a background corrected EBSD pattern is bell shaped, see Figure 4.33. If we further assume a Gaussian distribution, then the standard deviation and the entropy are related. This explains the similarity of these two maps. The similarity between the IQ map and the maps of entropy and standard deviation suggests that the IQ map is doing nothing more than providing a measure of the spread of intensities across the pattern (with background normalization) at least for a large step size as this experiment. The calculation of the Hough transform and the summation of the peaks is a more elaborate calculation than is necessary. This experiment suggests: 1) The mean of the diffraction pattern gives good topographic contrast. 2) The entropy and the standard deviation of the EBSD pattern are sensitive to grain boundaries. 3) In low noise patterns, for large scanning step sizes at least, the entropy and standard deviation maps are similar to the IQ maps, but with less noise.

A Similar operation can also be done on an area corresponding to a Kikuchi band on one EBSD pattern, as shown in Figure 4.35. Figure 4.37a shows the map formed by the mean of the chosen area, which corresponds to a Kikuchi band on the reference pattern. This image displays a blend of diffraction contrast with topographic contrast. The map formed by the mean of the chosen area (corresponding to one Kikuchi band in the reference pattern) divided by the mean of the pattern (Figure 4.37b) showed diffraction contrast mostly. Figure 4.37c is the map formed by the standard deviation of the chosen area (Kikuchi band on the reference pattern, Figure 4.35) and Figure 4.37d is the map formed by the standard deviation of the chosen area (Kikuchi band on the reference pattern, Figure 4.35) divided by the standard deviation of the pattern. These two maps are similar to the IQ map; both of them show grain boundaries and weak diffraction contrast.

We can also choose a zone axis from the reference pattern and use the intensity information of the chosen area (pixels inside the frame in Figure 4.36) to form maps; these maps are shown in Figure 4.34.

Experiment 2. Medium Scanning Step size. A 304 Stainless steel sample was used for the experiment. A FEI XL30 ESEM with a W filament was used. The EBSD system was a TSL OIM system installed with a CCD Camera. A Medium step size (45nm along the horizontal direction and 90nm along the slope direction) was used. The SEM accelerating voltage was 25 kV and the beam dwell time was about 1.2 second for each point. One set of (107×118) EBSD patterns were recorded and analyzed offline. Each pattern has 232 × 232 pixels.

Figure 4.38a, 4.38b and Figure 4.38c are maps formed by the mean, standard deviation and entropy of the EBSD patterns. Figure 4.39 is the inverse pole figure map. All of them show good diffraction contrast and have less noise than the IQ map, Figure 4.40. Some details, like the micro-twins and scratches on the samples are missed in the IQ maps, but are recognizable in the maps of the mean, standard deviation and entropy, marked by arrows in Figure 4.38. Other details (shown in the Figures), which could relate to small topography changes or strain levels in the sample are also missed in the IQ maps. These small details, whether caused by the topography or by the strain in the sample, have caused a change of the intensity distribution of the EBSD patterns. These small changes are detected using the intensity information directly, in the maps formed by the mean and the standard deviation, but are missed by the IQ map, which used the intensity information indirectly. In addition, an IQ map relies on the detection of Kikuchi bands, and thus it can be easily influenced by the detection of false peaks. As a result an IQ map correlates strongly with a map of CI (the measure of the confidence associated with the indexing). Mapping parameters, like the binning ratio and the size of the convolution mask, and sampling errors discussed above can also have some effects on it. However, maps of the mean, the standard deviation and entropy of the EBSD patterns don't change with the indexing parameters and have a weak correlation with confidence index.

All of these facts suggest that using the intensity information of the EBSD pattern directly, by forming maps of the mean or the standard deviation, has some advantages over using the intensity information indirectly in IQ maps. They provided better resolution and rich details.

Just like IQ mapping, the mapping of the mean and standard deviation suffers from the fact that the quality of the patterns deteriorated with time in some experiments, when the step size is less than or near to the size of the beam. This is caused by hydrocarbon contamination. We chose to normalize the generated maps, if the pattern deterioration phenomenon was not very severe. The normalization process is quite crude; we simply assume the sum of all the pixels in one row in one map should be constant. Even though this assumption is not quite true, it works well to provide effective normalization.

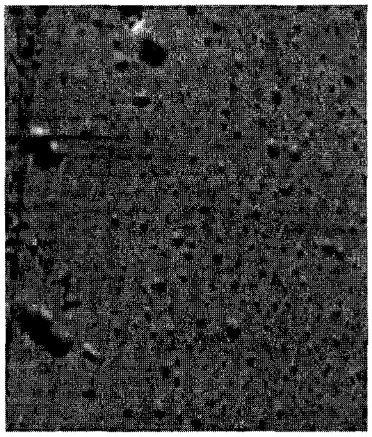

Figure 4.30a

←

Secondary electron Image with the distortion corrected.

Figure 4.30b

→

Image formed by the mean of the diffraction pattern.

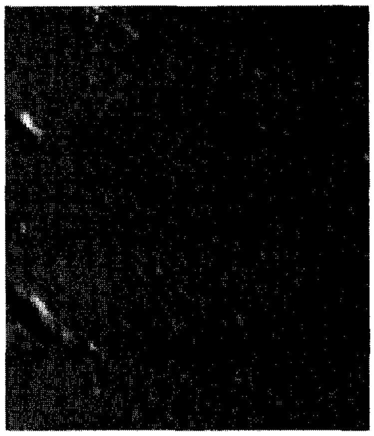

——— 20μ

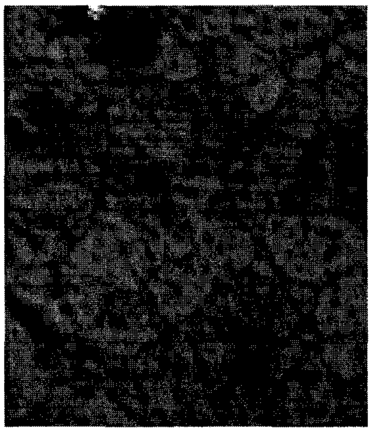

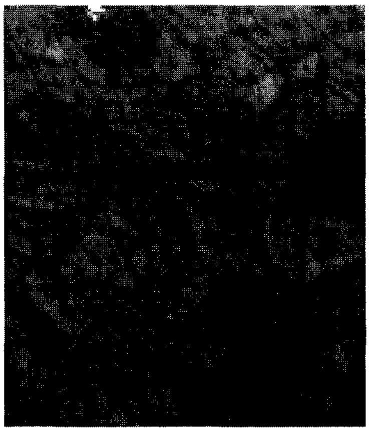

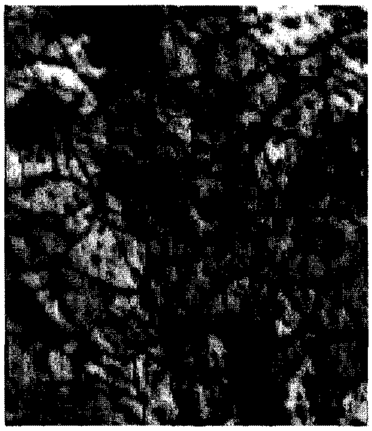

Figure 4.31a. Map of the Entropy of the EBSD pattern.

Figure 4.31b. Map of the Standard deviation of the EBSD pattern.

Figure 4.31c. IQ map.

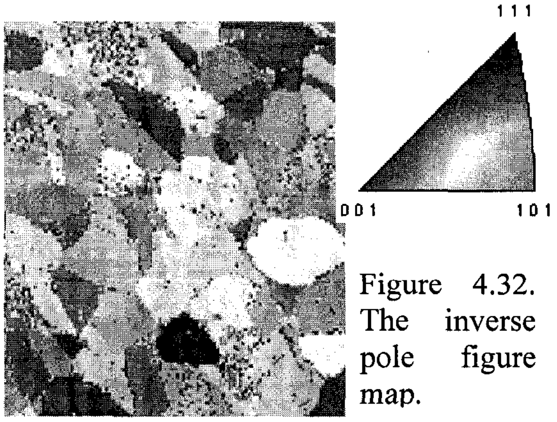

Figure 4.32. The inverse pole figure map.

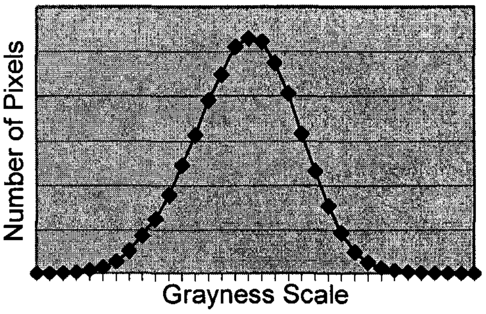

Figure 4.33. Typical histogram of an EBSD pattern.

Figure 4.34a

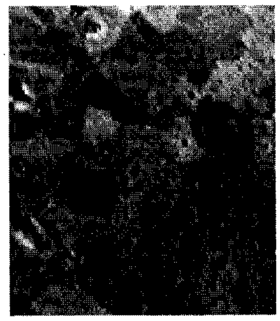

Figure 4.34b

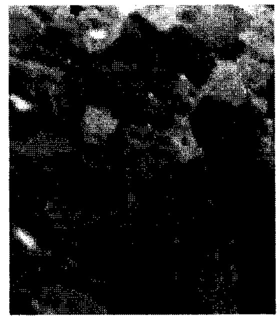

Figure 4.34c

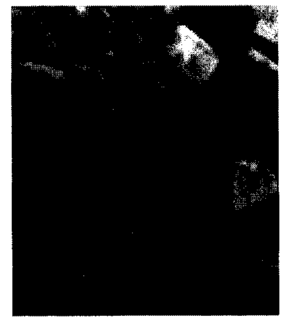

Figure 4.34d

30μ

Figure 4.34a. Map formed by the mean of the intensity of one Kikuchi band divided by the mean of the intensity of the pattern.

Figure 4.34b. Map formed by the mean of the intensity of one box area ($\bar{1}01$ zone axis on the reference pattern, Figure 4.35). This map has a blend of diffraction contrast and topographic contrast.

Figure 4.34c. Map formed by the mean of the box area ($\bar{1}01$ zone axis on the reference pattern) divided by the mean of the pattern. Most of the contrast comes from diffraction contrast.

Figure 4.34d. Map formed by the mean of a box area, which corresponds to the 101 zone axis on a reference pattern divided by the mean of the pattern.

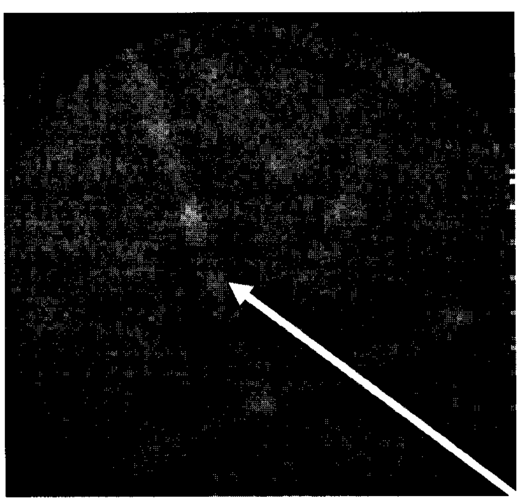

Band A

100 band

Figure 4.35. A noisy EBSD pattern, captured from a polycrystalline Ni sample. 0.26s pattern integration time, OIM system.

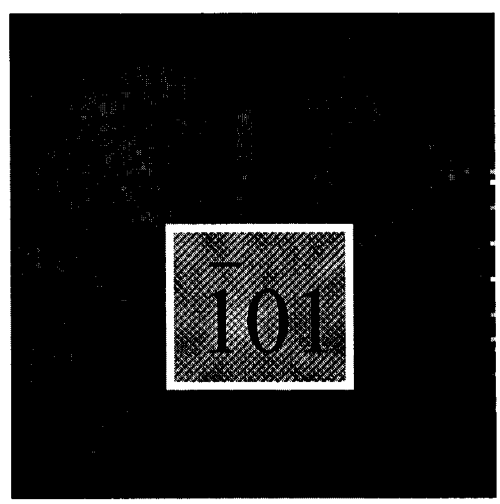

Figure 4.36. The $\bar{1}01$ zone axis. This zone axis is used to form maps in Figure 4.34 b and Figure 4.34c

Figure 4.37a. Map formed by the mean of band A shown in figure 4.35.

Figure 4.37b. Map formed by the mean of band A shown in figure 4.35 divided by the intensity of the pattern. The topographic contrast is eliminated.

20μ

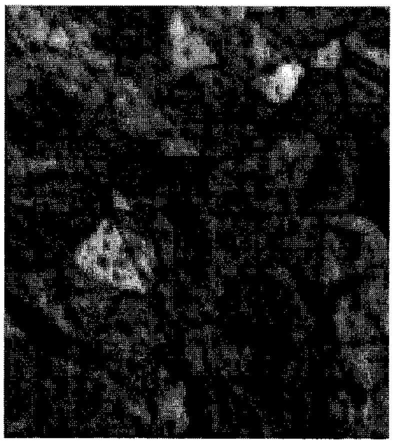

Figure 4.37c. Map formed by the standard deviation of band A shown in figure 4.35. First five rows are chopped off to enhance contrast.

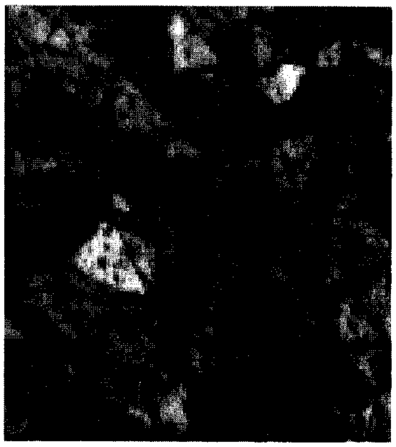

Figure 4.37d. Map formed by the standard deviation of band A shown in figure 4.35, divided by the standard deviation of the pattern. First five rows are chopped off to enhance contrast.

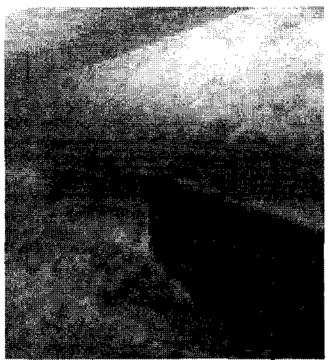

Figure 4.38a

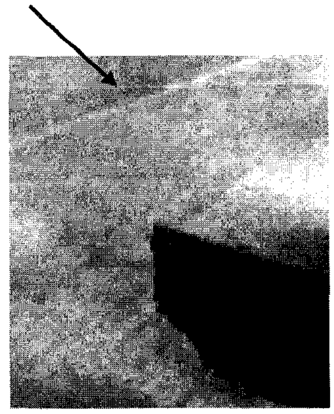

Figure 4.38b

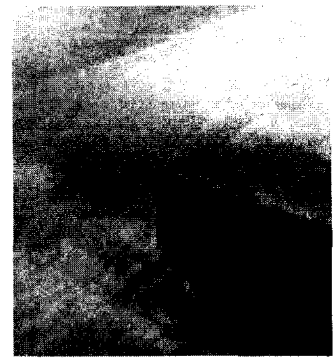

Figure 4.38c

Figure 4.38a. A map formed from the "mean" of the EBSD patterns. The details at the bottom left could be small topographic features. The intensity difference between the bottom left and the top right could be caused by a strain difference or a difference in topography. Arrows show the position of .micro twins.
Figure 4.38b. A map formed from the "standard deviation" of the patterns. The arrow shows fine details, which could result from a scratch.
Figure 4.38c. A map formed from the "entropy" of the EBSD patterns.
In all of these three Figures, details can be seen within the small grains, which have many twins.

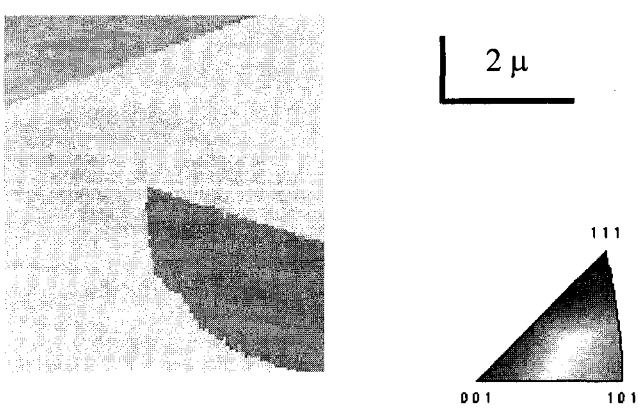

Figure 4.39. Inverse pole figure map, indexed with patterns binned 2:1 (116×116).

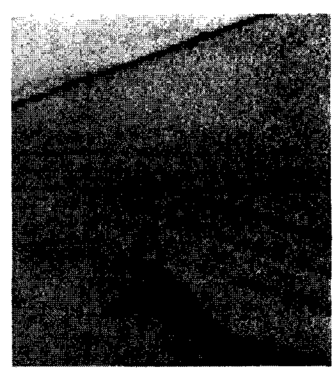

Figure 4.40. IQ map.

Experiment 3. Small Scanning Step Size. A GaN/Al_2O_3 structure was used for this test. Nominally, this is a single crystal sample. A FEI XL30 ESEM with a Schottkey field emission gun was used. The EBSD system was a TSL OIM3.5 installed with a DigiView CCD Camera. A small step size (30nm along the horizontal direction and 50nm along the slope direction) was used. Beam dwell time was about 0.92s for each point. One set of (100×104) EBSD patterns were recorded and analyzed. Each pattern has 456 × 456 pixels.

Figure 4.41a and Figure 4.41b are the maps formed by the mean and standard deviation of the EBSD patterns. These images can show some details of the sample, however, they are very blurry. This could be caused by the hydro-carbon contamination. When the beam size is comparable to the scanning step size and where a relatively long pattern capturing time is used, the hydro-carbon contamination can seriously degrade the pattern quality and decrease the sharpness of the Kikuchi bands. Figure 4.42 is the first pattern in the dataset, and Figure 4.43 is the last pattern in the captured pattern batch. The difference of these two Figures is evident as a result of the hydro-carbon contamination. After normalizing the generated maps (.dan file, not the image file), the effect of the contamination can be suppressed to a large extent. Figure 4.44a is the normalized map of mean, which looks much sharper than Figure 4.41a. However, some details can be seen better on the invert of this image, Figure 4.44b. Figure 4.45a is the normalized standard deviation map (Figure 4.41b) and Figure 4.45b is the invert of Figure 4.45a.

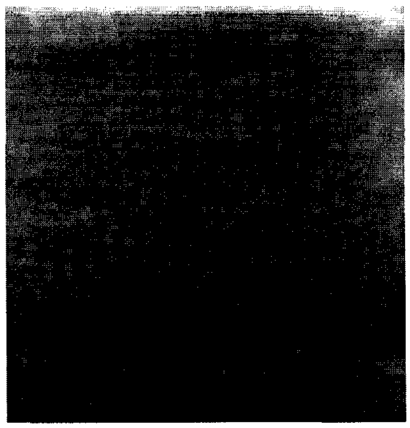

Figure 4.41a. Map formed by the mean of the pattern.

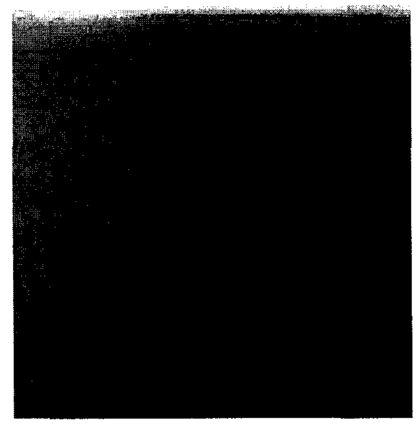

Figure 4.41b. Map formed by the standard deviation of the EBSD pattern.

1μ

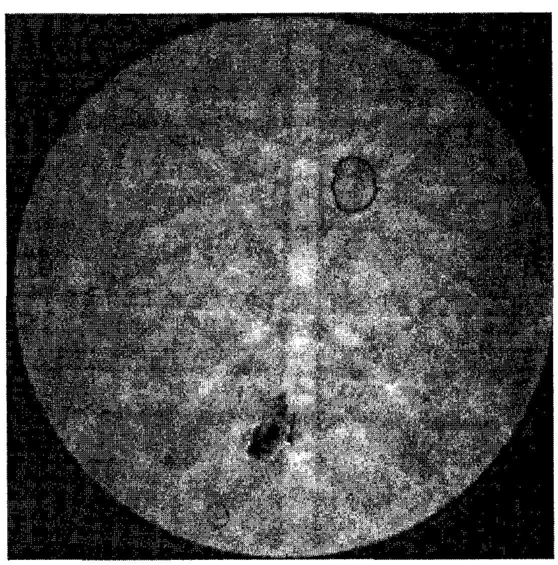

Figure 4.42. First EBSD pattern in the whole captured dataset.

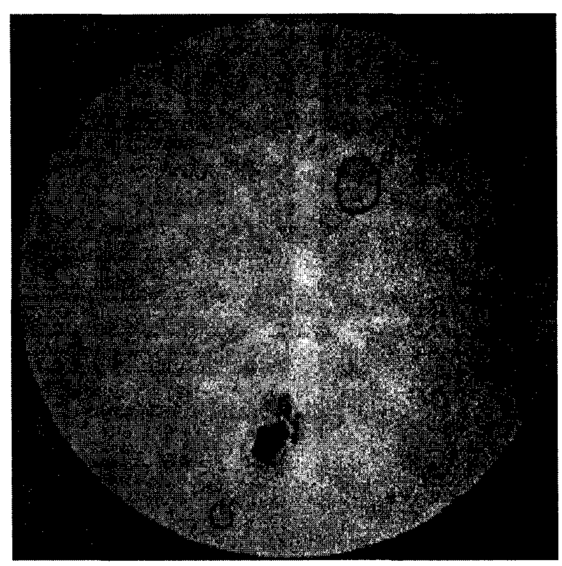

Figure 4.43. Last EBSD pattern in the whole captured dataset. This pattern is similar to Figure 4.42. However, it is heavily blurred as an effect of hydrocarbon contamination.

The features showed in those maps could not be found in the corresponding SE (secondary electron) image, Figure 4.46. However, it is still possible that those features showed in the image could also be caused by the topography of the surface, such as the trace of the growth. It is also possible that the dot-like features on the Figure 4.44 and Figure 4.45 could be related to the pits caused by the threading dislocations on the surface of the sample [58]. However, we cannot prove it at this moment. Figure 4.47 is the IQ map, which cannot reveal these small features either.

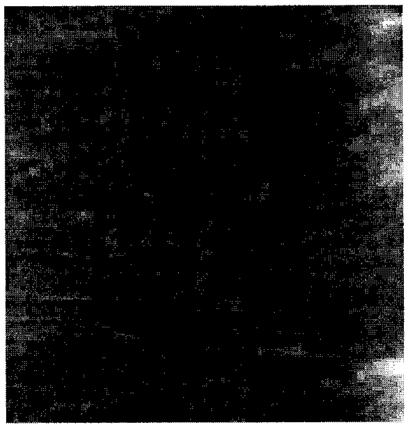

Figure 4.44a. Map of the mean, normalized.

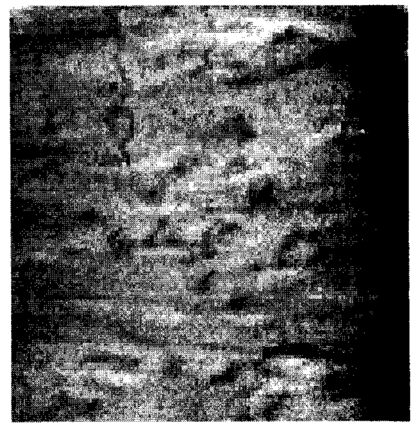

Figure 4.44b. Map of the mean, normalized, inverted.

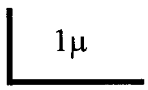

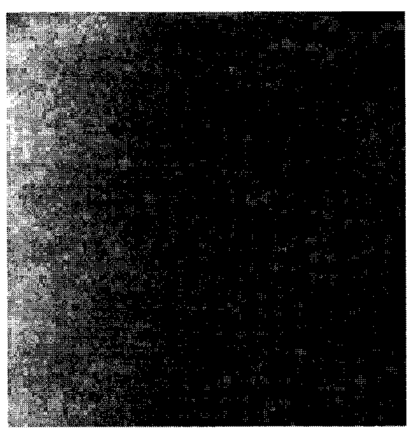

Figure 4.45a. Map of the standard deviation, normalized.

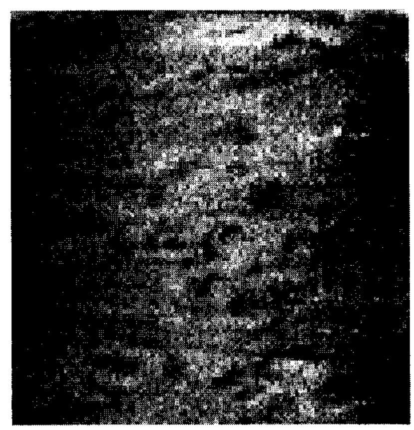

Figure 4.45b Map of the standard deviation, normalized and inverted.

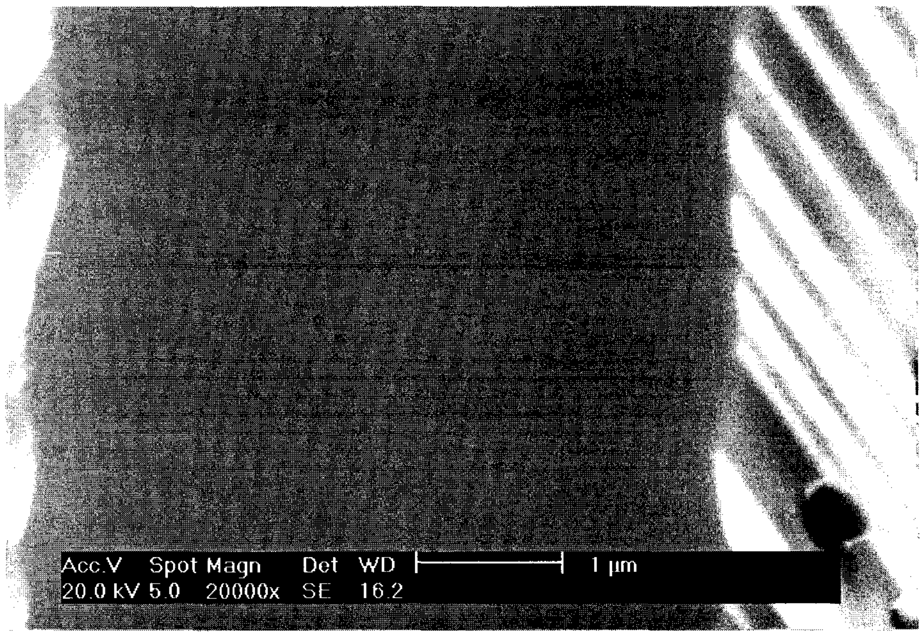

Figure 4.46. Secondary electron image, which failed to reveal any features on the surface of the sample.

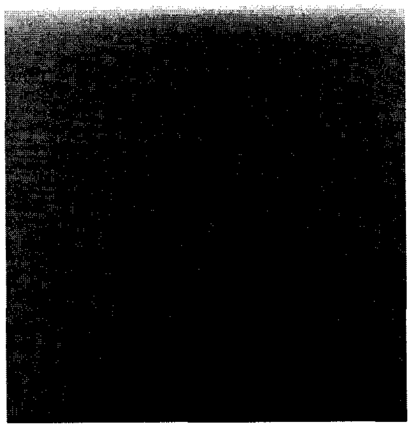

Figure 4.47a. IQ (Image quality) map. (2:1) Binning ratio.
The horizontal stripes are caused by the hydrocarbon contamination.

1μ

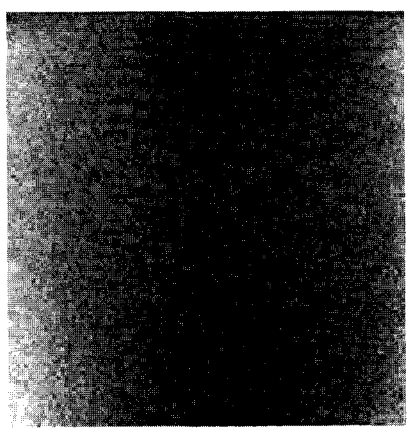

Figure 4.47b. Normalized IQ (Image Quality) map.
(2:1) Binning ratio.

4.4.2. Summary of This Section

In this section (Ch 4.4), we showed that using the intensity information of the EBSD patterns directly has some advantages over using the intensity information indirectly, like IQ (image quality) mapping.

Specifically, for large scanning step sizes when the scanned areas cover many grains, the map of the mean mainly shows topographic contrast and weak diffraction contrast. The map of standard deviation and entropy are similar to the IQ map and all of them show grain boundaries clearly, however, the map of standard deviation and entropy are less noisy.

If smaller step sizes are used and the scanning area is limited to several grains, the maps of mean, standard deviation and entropy show good diffraction contrast and reveal many details which can not be seen on the IQ map. However, as the scanning step size was further decreased, the hydrocarbon contamination began to play an important role. If the contamination is not too bad, we can minimize its effect through filtering.

The intensity information of a chosen area on the EBSD pattern can also be used to do mapping. These maps can also display good diffraction contrast. We choose to select Kikuchi bands or zone axes in a reference pattern and use the intensity information of the chosen area to do mapping (same areas and pixels for all other patterns). Typical mapping factors include mean of the band, mean of the band divided by the mean of the pattern, standard deviation of the band, and standard deviation of the band divided by the standard deviation of the pattern.

4.5. SHIFT MAPPING AND INTENSITY MAPPING

4.5.1. Application on ELO GaN/Sapphire Structure

In this research, we did a series of experiments to characterize GaN/Sapphire structure using both the intensity mapping method and band shift mapping method we described before. At first, the sample was cleaned carefully using TCE/methanol/IPA for about 1.5 hours followed by de-ionized water rinsing, then we used a plasma cleaner to clean it for about thirty minutes before it was moved to Drexel University and put into the SEM chamber. The EBSD system was a TSL OIM 3.5 with a DigiView CCD camera and the SEM was a XL30 Schottkey Field emission ESEM (FEI).

Experiment 4.5 A. The scanning step size was about 40nm along the X direction and 60nm along the slope and the beam dwell time was 0.93s. One set of EBSD patterns (91×72) patterns were recorded and analyzed offline. Each pattern has 456×456 pixels. Figure 4.48 shows the first pattern and Figure 4.49 shows the last pattern of this batch. Obviously, the hydro-carbon contamination blurred the EBSD patterns heavily.

Figure 4.50a, 4.50b and 4.50c are the maps formed by the mean, standard deviation and entropy of the EBSD patterns from the GaN/Sapphire structure. The horizontal stripes on these images and the intensity varying background (trend) on the maps of the standard deviation (Figure 4.50a) and entropy (Figure 4.50c) are caused by the hydrocarbon contamination. In order to minimize the effect of contamination and increase contrast, these maps are normalized, as shown in Figure 4.51a, 4.51b and 4.51c. The reverse of Figure 4.51a, 4.51b and 4.51c are shown in Figure 4.52a, 4.52b and 4.52c.

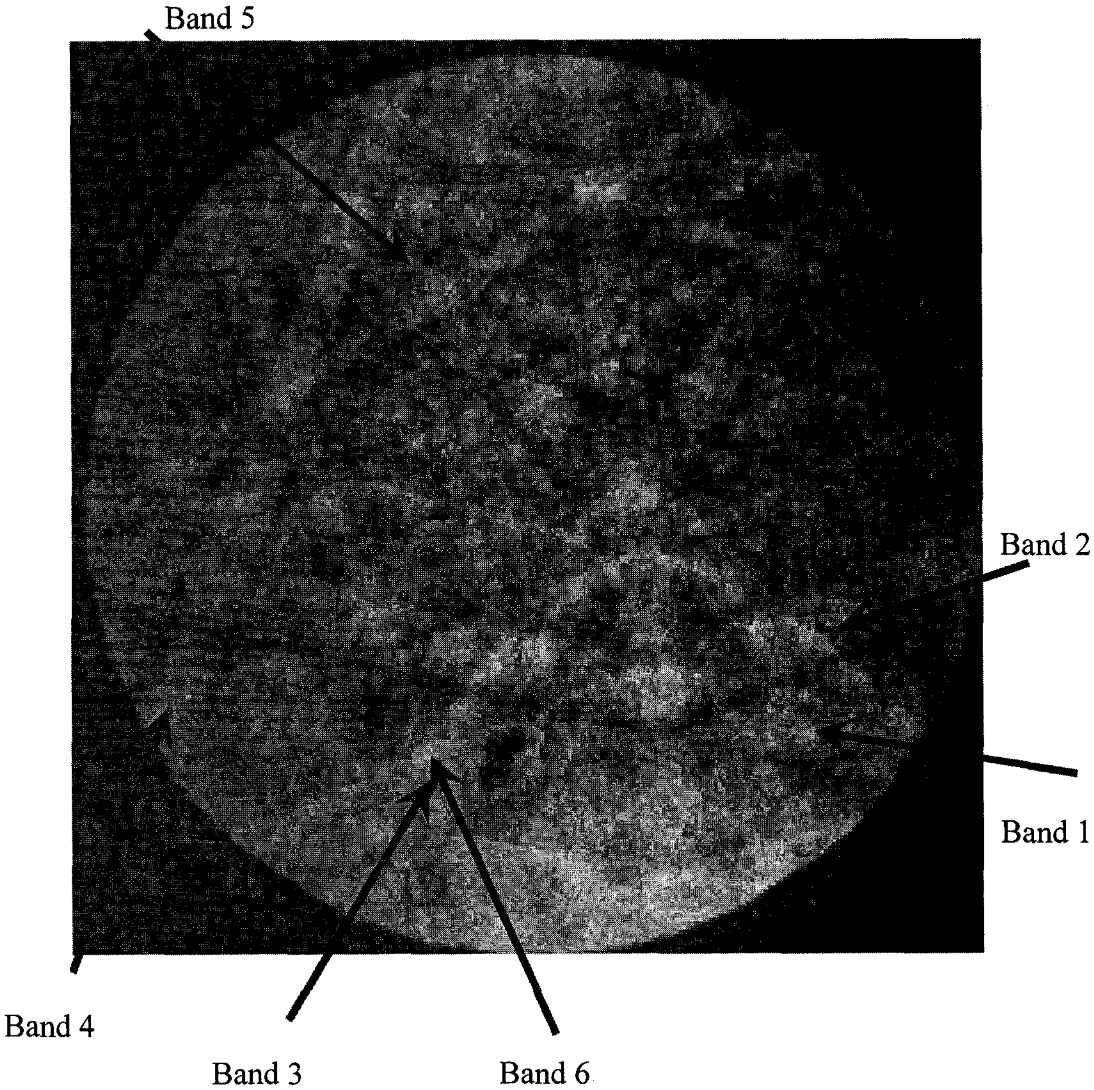

Figure 4.48. An EBSD pattern captured from GaN/Sapphire heterostructure. This is the first pattern of the batch. The shift and intensity of the four bands marked by the arrows are mapped.

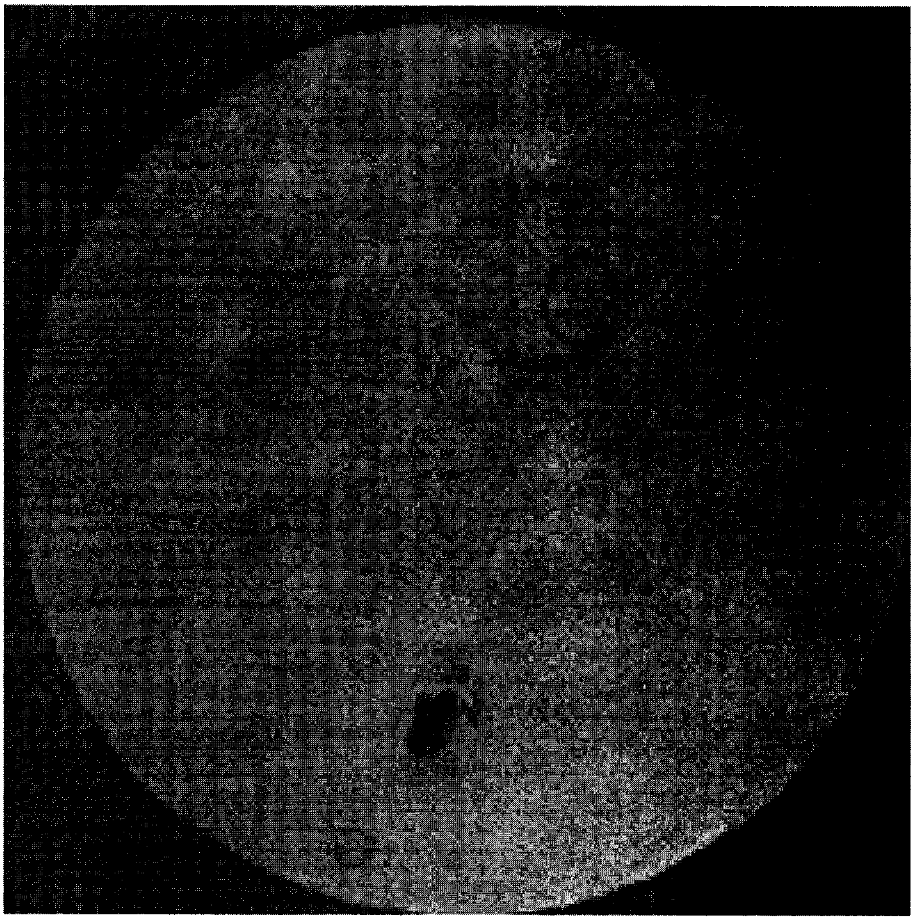

Figure 4.49. An EBSD pattern captured from GaN/Sapphire structure. The last pattern of the whole batch. This pattern is blurry as a result of hydrocarbon contamination.

Figure 4.50a. Map formed by the mean of the EBSD pattern.

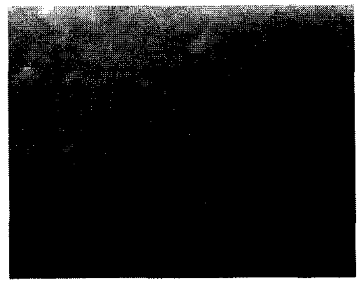

Figure 4.50b. Map formed by the standard deviation of the EBSD pattern.

Figure 4.50c. Map formed by the entropy of the EBSD pattern.

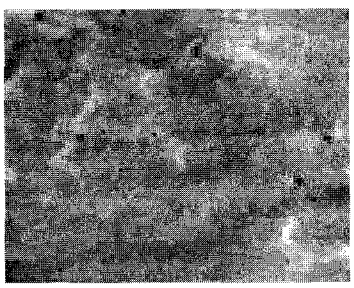

Figure 4.51a. Map formed by the mean of the EBSD pattern, normalized.

Figure 4.51b. Map formed by the standard deviation of the EBSD pattern, normalized.

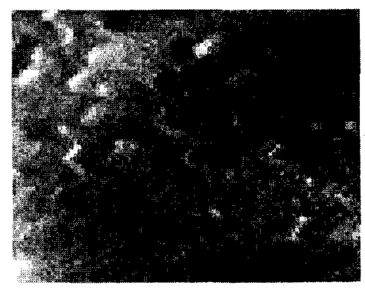

Figure 4.51c. Map formed by the entropy of the EBSD pattern, normalized.

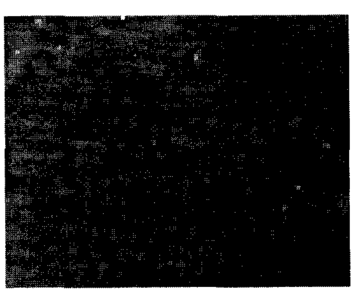

Figure 4.52a. Invert of figure 4.51a.

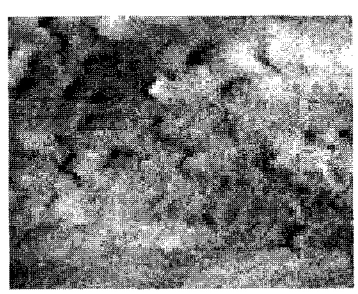

Figure 4.52b. Invert of figure 4.51b.

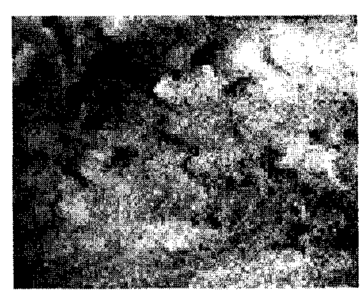

Figure 4.52c. Invert of figure 4.51c.

2μ

There are two kinds of features shown in Figure 4.52 and 4.53, the chevron shapes and dot-like features. The secondary electron image **cannot** show any details and neither can the IQ map, Figure 4.53. At this stage of research, we are not sure of the contrast mechanism of these features. They could be caused by a topographic difference or an orientation difference at the surface of the sample.

Through using a Schottkey field emission SEM (or STEM), a relatively high accelerating voltage and very high vacuum (10^{-10} torr), some research shows it is possible to image the growth trace on the surface of the GaN/Sapphire structure (LEO) using a specially designed secondary electron detector [58]. This technique can image monolayer growth steps on the surface of the material [60]. However, the strict requirements on the instrument for this method can not be easily satisfied and baking the testing materials is often needed to remove the adsorption on the surface. In order to increase the signal to noise ratio, the testing sample is usually highly tilted, as a result this technique is usually categorized into the category of SREM (Scanning Reflection Electron Microscopy) [61].

Since secondary electrons come from a depth less than 5nm, they are more sensitive to the surface than low loss BSEs, which are supposed to come from a depth around 20-30nm. Thus, the image formed by the low loss BSEs, such as the map of the mean, is less sensitive to the adsorption effect on the surface and could have a less strict requirement on the vacuum. As a result, the chevron shapes shown on the intensity maps (Figure 4.51 and Figure 4.52) could be the images of subtle topographic changes on the surface of the GaN/Sapphire structure. On the other hand, it is also possible that these chevron shapes are caused by diffraction contrast. They could also be images of sub-grain boundaries. The dot-like features shown in Figure 4.51 and Figure 4.52 could be the images of the pits caused by the threading dislocations. Unfortunately, we can not prove this either.

Using the intensity distribution of selected areas, such as the area corresponding to one Kikuchi band in the reference pattern, we can also image small features on the sample as discussed in chapter 4.4. We specially chose six bands on a reference pattern, marked by the arrows in Figure 4.48, and use the intensity information of the chosen areas to form maps. The normalized maps of the mean, formed this way, are shown from Figure 4.54a to Figure 4.54e. Most of them show at least some of the chevron shapes, if not all of them. Interestingly, the contrast of the chevron shapes changed or even disappeared when using different Kikuchi bands to form maps.

Figures 4.55a-4.55e are the maps formed by the shift of the Kikuchi bands marked by the arrows in Figure 4.48. These figures showed that there is small orientation fluctuation on the surface of the nominally single crystal sample. The first pattern of the dataset is used as the reference and several Kikuchi bands are chosen from this pattern (Figure 4.48), the shifts of these Kikuchi bands along the ρ direction are mapped.

Since the shift is measured in Hough space, this technique does better at measuring the shift of the Kikuchi band along the direction perpendicular to this band (ρ direction) than measuring the rotation of the band, which could not be detected very accurately. We choose not to include the detection of the rotation in this research. Figure 4.24 shows that the curve of cross correlation coefficient is very flat in the θ direction but it is relative abrupt in ρ direction. So, shift along the θ direction could be more easily affected by noise and the interpolation is prone to error. In fact, from the shift of two non-parallel bands, we can also calculate the rotation of the bands. We didn't implement this in our research.

During the pattern capturing process, for the first twenty to thirty rows of points, the sample had not been exposed to the electron beam for a relatively long time, so the hydrocarbon contamination was not too serious, and the shift measurement was relatively accurate and less noisy. Later on, the hydro-contamination blurred the EBSD patterns and the Kikuchi bands also became blurry. As a result, the shift measurement for the later captured EBSD patterns became less accurate, and the corresponding pixels on the shift maps became noisy, especially for the pixels on the lower rows of the shift maps (Figure 4.49). Nevertheless, our measurement shows the difference between the maximum and the minimum in these maps is less than 3 to 4 pixels. Considering the geometry of the setup, Figure 4.56, the distance between the sample and the camera is about 4.6cm and the effective pixel size is about 80μ. Thus, the measured largest orientation difference among those regions whose orientations are slightly different is less than 0.5° (usually less than this). However, we failed to image a single threading dislocation through mapping the shift of the Kikuchi bands. The major problems are the large effective pixel size we used and low pattern quality caused by the hydrocarbon contamination. A single dislocation can distort an atomic plane at the scale of 10^{-4}rad, which corresponds to less than 10μ shift of a Kikuchi band at most. For noisy EBSD patterns like Figure 4.42 and Figure 4.43, this value is too good to reach.

Another interesting phenomenon is that on the shift maps, the edges of these small regions, whose orientations differ from each other, correspond to the place where the "chevron shapes" appeared on the intensity maps, as was clearly showed in the next experiment.

Experiment 4.5 B. The same sample and configuration as EXP 4.5A were used in this experiment. The scanning step size is about 40nm along X direction and 60nm along the slope. The pattern capturing time was 0.85s/point. Unfortunately, we only succeeded in capturing one small batch of patterns (90×32). Each pattern has 454 × 454 pixels

The maps formed by the mean, standard deviation and entropy of the captured patterns batch, Figure 4.57a-4.57c were very small as a result of the limitation of the size of the dataset. The features shown in these maps, especially the chevron shapes, are similar to those shown on the intensity maps generated in Experiment 4.5 A, like Figure 4.51 and Figure 4.52.

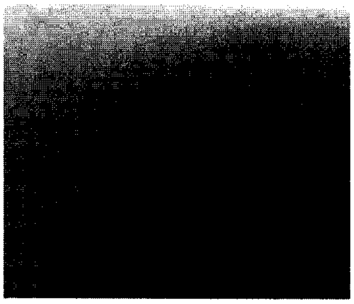

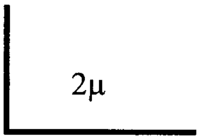

Figure 4.53. IQ map
(2:1) binning ratio.

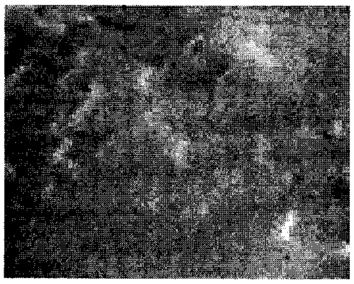

Figure 4.54a. Map formed by the mean of band 1. Normalized.

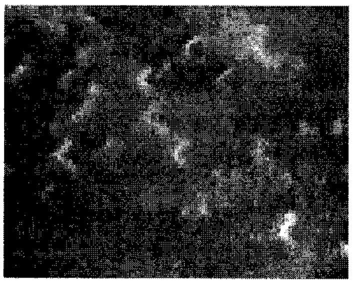

Figure 4.54b. Map formed by the mean of band 2. Normalized.

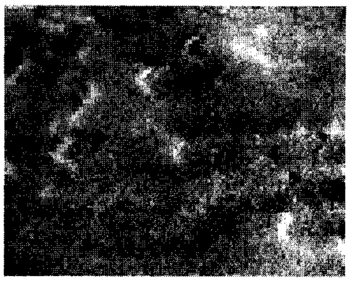

Figure 4.54c. Map formed by the mean of band 3. Normalized.

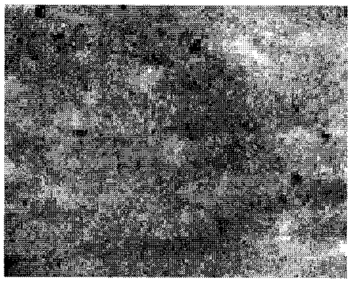

Figure 4.54d. Map formed by the mean of band 4. Normalized.

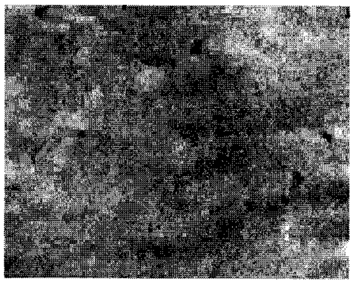

Figure 4.54e. Map formed by the mean of band 5. Normalized.

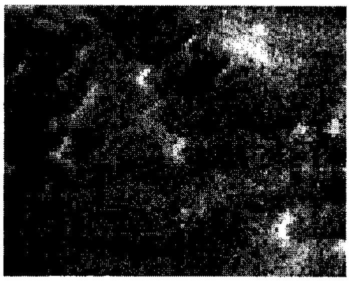

Figure 4.54f. Map formed by the mean of band 6. Normalized.

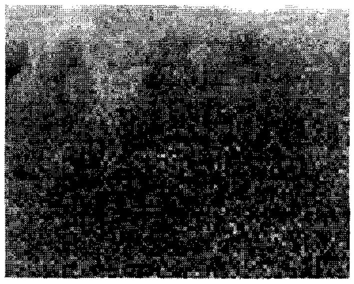

Figure 4.55a. Map formed by the shift of the Kikuchi band 1 on figure 4.48 for experiment 4.5A.

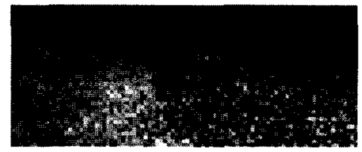

Figure 4.55b. Top part of the map formed by the shift of the Kikuchi band 2 on figure 4.48 for experiment 4.5A.

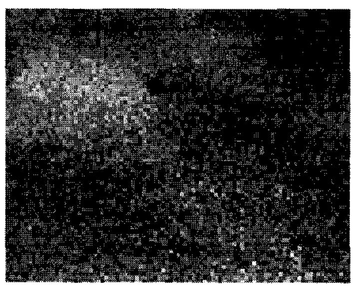

Figure 4.55c. Map formed by the shift of the Kikuchi band 3 on figure 4.48 for experiment 4.5A.

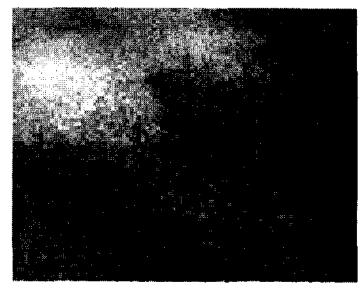

Figure 4.55d. Map formed by the shift of the Kikuchi band 4 on figure 4.48 for experiment 4.5A.

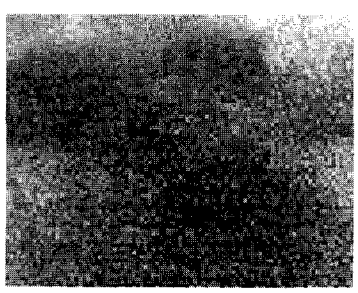

Figure 4.55e. Map formed by the shift of the Kikuchi band 5 on figure 4.48 for experiment 4.5A.

Figure 4.55f. Map formed by the shift of the Kikuchi band 6 on figure 4.48 for experiment 4.5A.

2μ

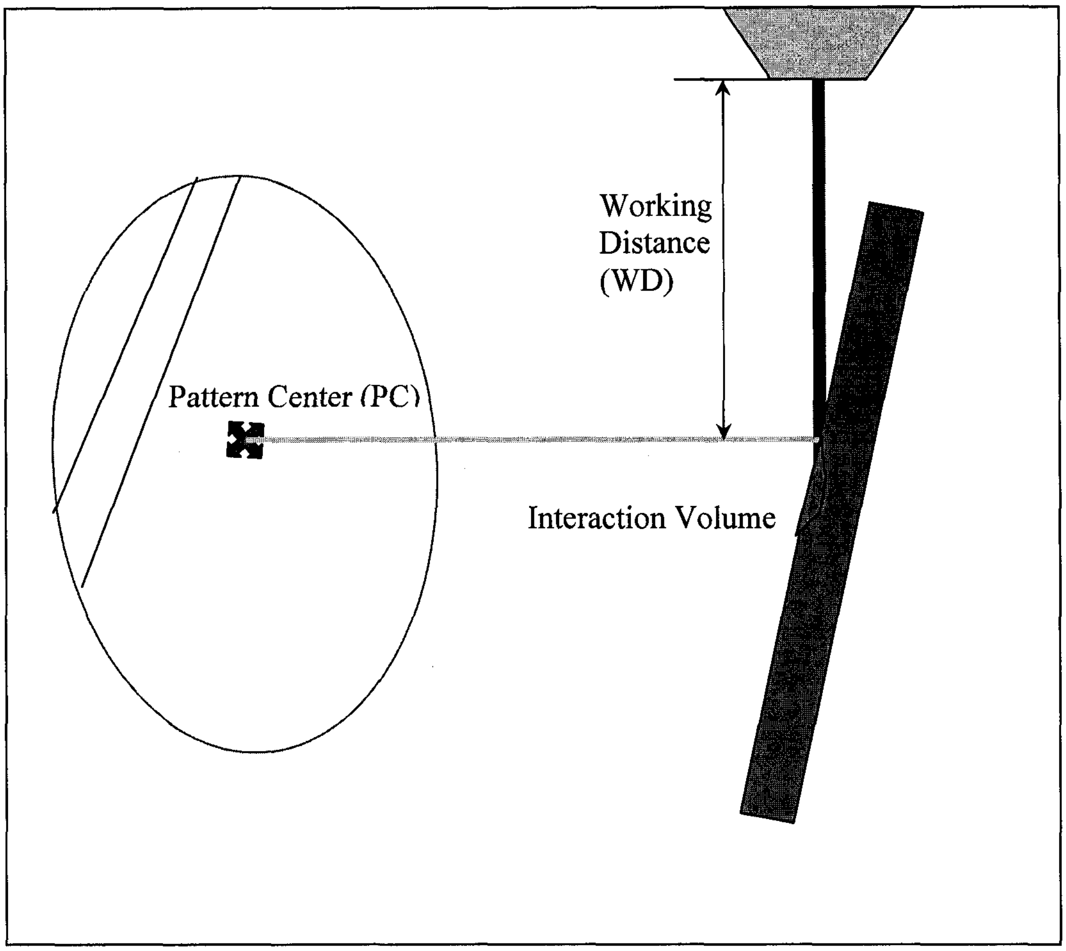

Figure 4.56. In the setup for mapping the small features on the GaN/Sapphire structure. The distance between the camera and the sample is about 40mm. The working distance is about 16mm. The effective pixel size is about 80μ.

Similarly to Experiment 4.5 A, we chose three Kikuchi bands from the reference pattern (first pattern in the dataset), which are marked by arrow heads in Figure 4.58, to form shift maps. The shift maps are shown in Figure 4.59a to 4.59d. These Figures are less noisy than those generated in Experiment 4.5 A, since the dataset is small, the sample exposure time to the electron beam was short and the effect of contamination was less serious. Shift maps, Figure 4.59a to 4.59d, showed there were some small regions, whose orientation differs slightly from each other, on the surface of the sample. Since the shift map relies on the shift of the position of the Kikuchi bands, which are rigidly connected with the atomic planes, the shift maps should be sensitive to the orientation change of the samples. This suggested that there could be some small sub-grains at the surface of this GaN/Sapphire structure. More interestingly, if we compare the maps of intensity, Figure 4.57, and the maps of shift, Figure 4.59, we can find that on the shift maps, the edges of those regions, whose orientations are different, correspond to the place where chevron shapes appeared on the intensity maps. In the shift maps, the difference of the maximum and minimum value of the shift of the band is less than 3 to 4 pixels. So, the largest orientation difference among these small regions is less than 0.4°.

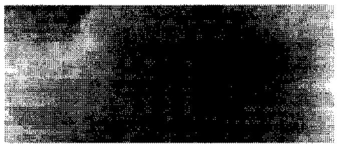

Figure 4.57a. Map formed by the mean of the EBSD patterns for GaN/Sapphire structure. Experiment 4.5B.

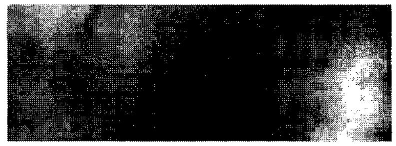

Figure 4.57b. Map formed by the standard deviation of the EBSD patterns for GaN/Sapphire structure. Experiment 4.5B.

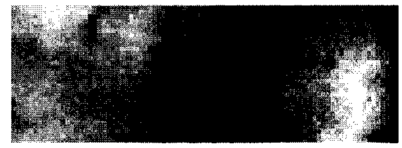

Figure 4.57c. Map formed by the standard deviation of the EBSD patterns for GaN/Sapphire structure. Experiment 4.5B.

2μ

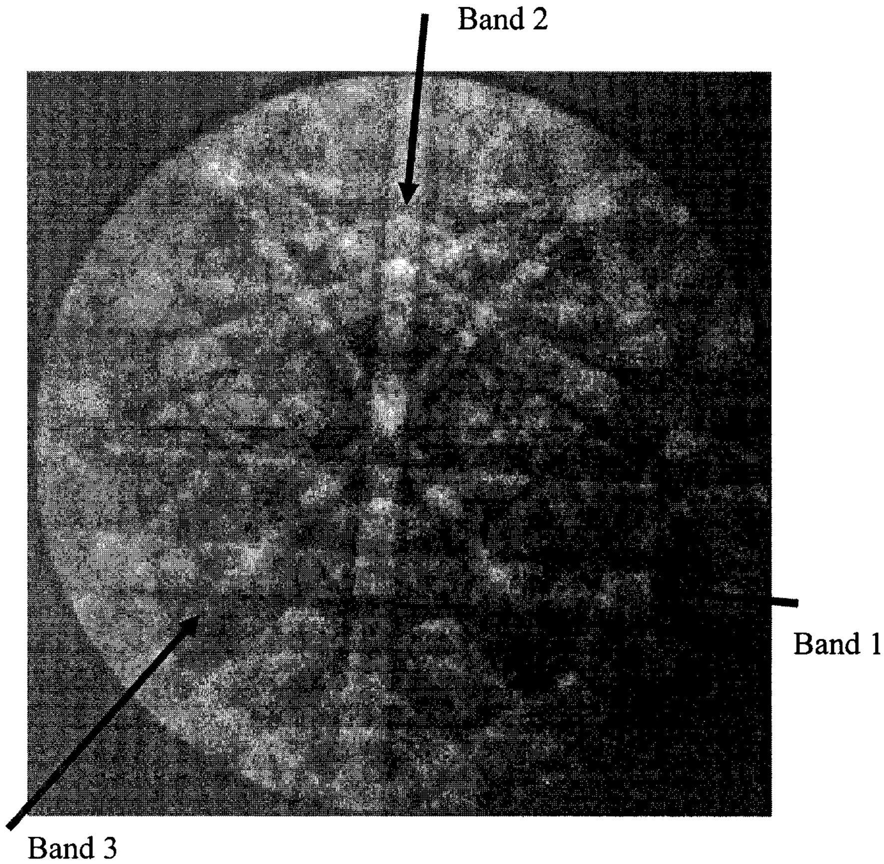

Figure 4.58. An EBSD pattern captured from GaN/Sapphire structure. This pattern works as a reference and the shift of the Kikuchi bands marked by the arrow are used to form maps (Figure 4.51). Experiment 4.5B.

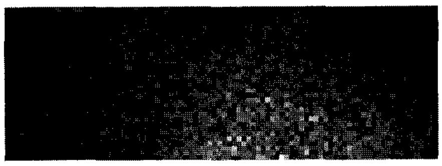

Figure 4.59a. Map formed by the shift of the Kikuchi band 1 on figure 4.50 for experiment 4.5B.

Figure 4.59b. Top part of Figure 4.51a. The contrast is enhanced to show details.

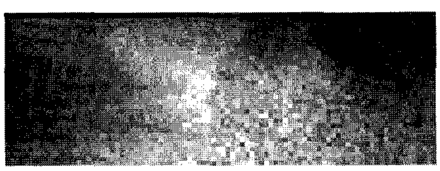

Figure 4.59c. Map formed by the shift of the Kikuchi band 2 on figure 4.58 for experiment 4.5B.

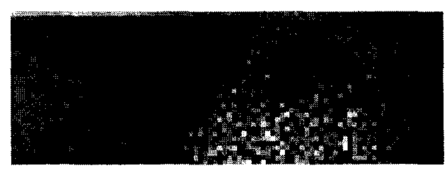

Figure 4.59d. Map formed by the shift of the Kikuchi band 3 on figure 4.58 for experiment 4.5B.

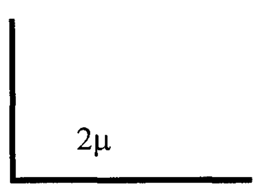

4.5.2. Summary of this Section

We studied the GaN/Sapphire structure through incorporating the method of detecting the shift of Kikuchi bands and the method of mapping the intensity information of the EBSD pattern or Kikuchi bands.

Experiments showed some small features, like chevron shapes and dot-like features, which can be revealed through intensity mapping, are missed in the IQ maps and secondary electron images.

Experiments on mapping the shift of the Kikuchi bands showed there is some orientation fluctuation on the surface of the GaN/Sapphire heterostructure (single crystal). The orientation difference among those small regions is less than 0.5° when measured using our shift measurement method. For some regions at least, their edges correspond to the chevron shapes in the maps of the intensity.

We failed to image single dislocations using the intensity mapping methods. Possible reasons could include relatively large beam size used in the experiment and hydrocarbon contamination. These two factors could be the limitation of this technique.

4.6. OTHER PRACTICAL PROBLEMS

This part of the experiment was done on FEI XL30 with a W filament and TSL's OIM Data Collection system (in-chip CCD camera). The SEM acceleration voltage was 25 kv. Each EBSD pattern has 232×232 pixels. The scanning step size was 45nm in the X direction and 90nm in the Y direction. The beam size was estimated to be about 40nm and the beam dwell time was set as 1.2 second for each point. The stainless steel sample was carefully cleaned in order to minimize the effect of hydrocarbon contamination.

4.6.1. Sampling ratio

Figure 4.60, Figure 4.61 and Figure 4.62 are the generated inverse pole figures using the same batch of EBSD patterns but with different binning ratios. All the other parameters used for the automatic indexing are the same, like medium butterfly mask (9×9), peak symmetry parameter, and bands numbers. Figure 4.63, 4.64 and Figure 4.65 are the IQ maps corresponding to Figure 4.60, 4.61 and 4.62. Through checking the original EBSD patterns with the overlaid indexing, we find that Figure 4.61 has the most reliable result, thus the 2:1 binning ratio shows the best performance in this experiment.

Binning ratios can have a complex effect on the practical indexing results. On one hand, binning patterns can suppress noise to some extent. On the other hand, it also increases the sampling interval. These two factors have contradictory effects. As a result, there exists a best binning ratio for the automatic indexing. In addition, as we change the binning ratio, we still used the same butterfly mask, which could have different responses to different binning ratios.

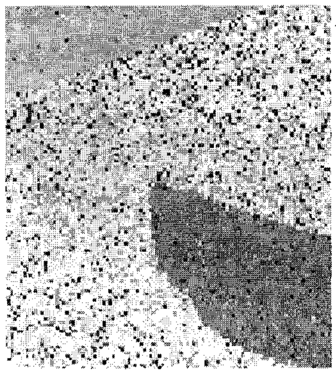

Figure 4.60. Inverse pole figure map of a 304 stainless steel sample indexed with unbinned patterns (232×232).

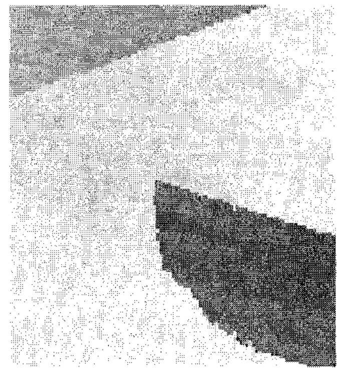

Figure 4.61. Inverse pole figure map, indexed with patterns binned 2:1 (116×116). This map gives the best result.

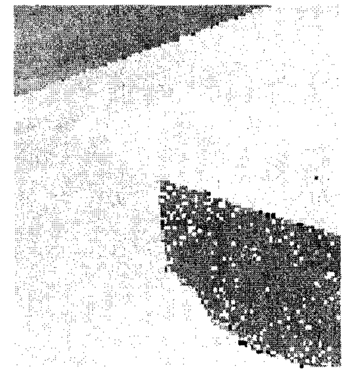

Figure 4.62. Inverse pole figure map of 304 stainless steel, (binning ratio 3:1).

Figure 4.63

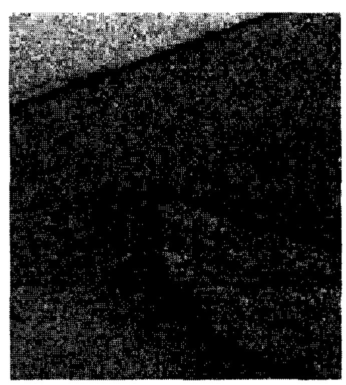

Figure 4.64

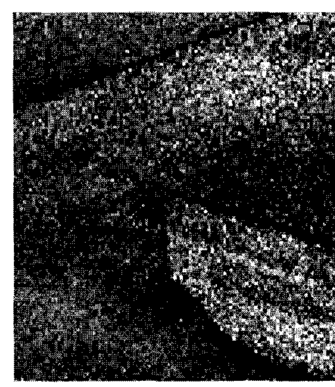

Figure 4.65

Figures 4.63, 4.64 and 4.65 are IQ maps corresponding to figures 4.60, 4.61 and 4.62. Figure 4.64 is less noisy than figure 4.63 or figure 4.65.

3μ

4.6.2. Pattern Filtering

In order to test the effect of the Gaussian filter on the indexing accuracy, we first filtered all of the EBSD patterns with a radius of 12 pixels and saved all of the patterns to one directory in the local hard drive. Then, we used our revised OIM Data Collection program to do the offline scan (generate a data file). Finally, we used the OIM Data Analysis program to analyze this data file. Experiments showed there is no big difference between preprocessing the batch patterns with or without the Gaussian filtering if using an appropriate butterfly mask. However, if we choose not to use any convolution mask, pre-filtering EBSD patterns with a Gaussian filter, Figure 4.66, gives much better result than using no filter, Figure 4.67. Their difference is significant. Since using a large radius Gaussian filtering mask to pre-process the EBSD patterns can suppress the uneven background in the Hough transform, it has the potential to replace the butterfly convolution step in the Hough space. In this experiment, we still used the standard Hough transform.

For both of the methods to do Gaussian filtering, the calculation time is irrelevant to the mask size. There is no big difference between the two methods. However, using the recursive filtering method is significantly faster than using the Fourier transform method. For a pattern of 480×480 pixels, our test shows the processing time for the recursive filter method is typically less than 1/10 seconds, while the calculation time for the Fourier transform method is around 0.4 seconds in our computer. Considering the fact that most EBSD systems use binning (could be done on hardware, software, or both hardware and software) to reduce the size of the image, Gaussian filtering can be done effectively in real time and without noticeable delay.

This experiment also suggested that a Gaussian filter could be an effective alternative to the butterfly mask.

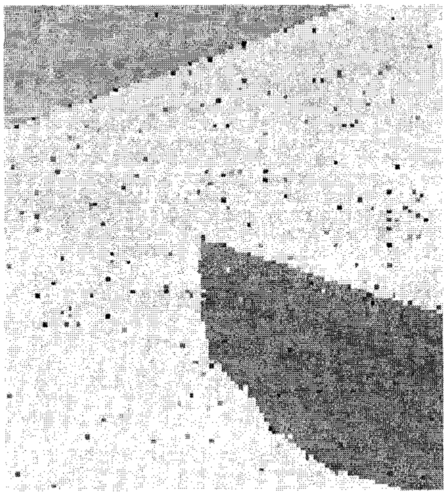

Figure 4.66. Inverse Pole Figure map formed from Gaussian-filtered EBSD patterns. No convolution mask was used. Binned Pattern size: 116 (2:1).

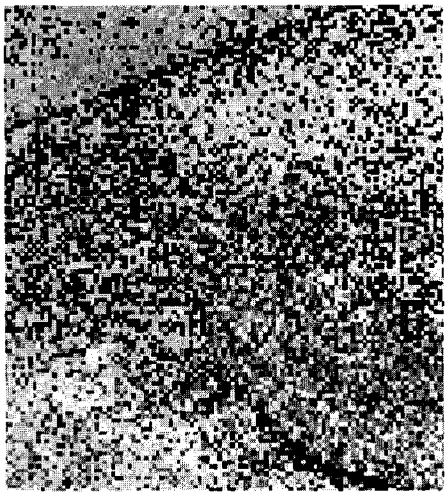

Figure 4.67. Inverse pole figure map, formed from EBSD patterns that are *not* filtered. No convolution mask was used. Binned Pattern size: 116 (2:1).

3μ

4.6.3. Data Storage

"Saving all of the Data" seems a cure for everybody and everything. In making a successful map from an EBSD scan there are many parameters to set. The great advantage of storing all the EBSD patterns is that the parameters can be optimized off-line. The data is not ruined by making a poor choice of parameters before the experiment starts.

Moreover the size of the storage problem is not as bad as it might seem. A typical EBSD pattern, in a fast scan, is usually binned to 120×120 or 240×240 pixels. For most image formats, an 8 bit gray scale (pixel depth) is standard and it works well for most applications. Thus, the size of one uncompressed pattern ranges from 10k-50k bytes. A typical map involves around 10k patterns. As a result, all of the raw data used (or discarded, more precisely) is only between 100Mb and 600Mb. This size can be further decreased if we choose to use video format or to compress the raw patterns. On the other hand, a hard disk of 300G byte is not something new nowadays.

The advantage of saving all the diffraction patterns is manifest in many other areas, such as testing the integrity of the data, correcting wrongly-labeled phases and correcting the calibration. New software to take advantage of these possibilities should be developed.

4.6.4. Hydro-Carbon contamination, the practical limiting factor

One major concern of this research was to image and characterize single dislocations. However, until this stage of research, we didn't achieve this goal.

In order to reach the level of characterizing dislocations, we need to reduce the scanning step size to the level of tens of nm at least. Since EBSD patterns are usually noisy, a long pattern integration time is needed. This produces the hydro-carbon contamination, which proved to be the major difficulty for this research.

When the electron beam bombards the sample, the adsorbed hydrocarbon molecules on the surface of the specimen are damaged and a layer of carbon-rich, polymerized film is formed on the surface [59]. The contaminating hydrocarbon molecules could come from the sample preparation, vacuum oil from the rotary or diffusion pumps and atmospheric deposition [59].

According to Reimer [59], for TEM samples at least, there are three types of irradiation conditions corresponding to different contamination situations. As a result, different pre-caution schemes are used to minimize the contamination.

1) Uniform contamination layer. This kind of contamination is formed when a large beam and uniform irradiation is used. The hydrocarbon layer is flat and the contamination rate is slow. This form of contamination is relatively easy to cope with and seems not a large challenge to our experiment.

2) Annular contamination layer. This is caused by the uniform irradiation of a small area (on the scale of microns). The contamination rate is relatively fast

3) Needle shape contamination layer. When the illumination area is further decreased to less than 0.1 μm, the diameter of the annular zone (above) begin to decrease and a needle shaped contamination layer begins to form.

Since we were using an SEM with relatively low chamber vacuum (ESEM, 10^{-5} Torr) most of the time, careful attention was paid to clean the samples thoroughly. However, under most of our experimental conditions, we can still see the formation of the annular contamination layer, shown in Figure 4.68. For our research, usually after half hour of scanning, the EBSD patterns began to degrade and even totally disappear. For the generated intensity maps, like the map of the mean, standard deviation and the entropy, the map shows changing background intensity (Figure 4.50b) and/or stripes (Figure 4.50a) as an effect of the contamination. Sometimes, the stripes can also be seen on the SE image of the contamination patch left on the surface of the sample.

If the contamination is not too bad and the Kikuchi bands on most of the EBSD patterns still can be seen, the intensity maps can still be meaningful. Its effect can be removed to some extent through software. In this research, we choose to normalize the intensity maps using a very "rude" filtering method and it works most of the time, even if the principle of this method is flawed. We simply suppose the sum of the intensity of all pixels on any row in the map should be equal. This normalization is not done on the image file directly; rather it is done on the mapping data file directly (.dan).

Several things could be done separately or together to alleviate the effect of the hydro-carbon contamination and further improve the accuracy and precision for EBSD, such as:

1). Baking or cooling the testing sample. These methods can effectively reduce the adsorption of the sample surface, however, a special sample stage must be designed and heating the sample could lead to a change of the microstructures.

2). Using a high performance SEM, which has a high vacuum chamber and can deliver more current to the diffraction volume. A better candidate is an in-lens thermal FEG SEM [23].

3). Using of new kinds of CCD cameras, such as a "Lens-on-chip" CCD camera, which has higher sensitivity and thus needs less pattern integration time, could be advantageous too

4). Using a dual beam FIB (Focused Ion Beam) also has some advantages over conventional SEM in several ways. First, the hydrocarbon contamination generated during the scanning process can be removed by quickly scanning the surface using a low dose ion beam. Second, a FIB is also equipped with several gas inlets. Through blowing in a small amount of O_2 during the scanning process, the hydrocarbon contamination can also be effectively controlled.

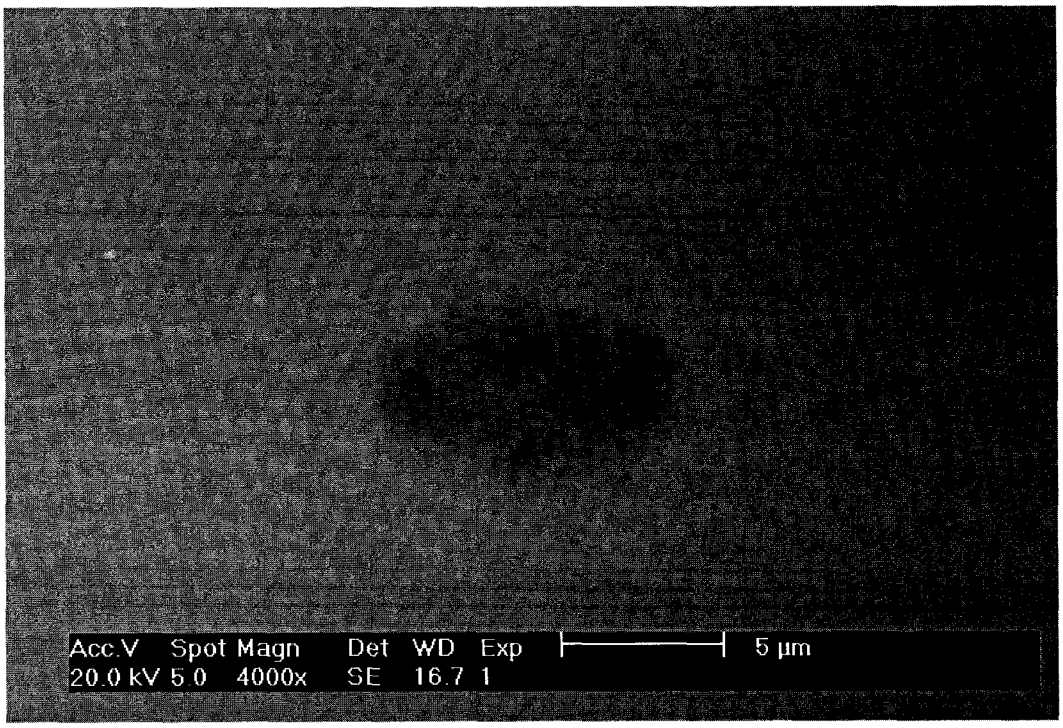

Figure 4.68. Contamination formed on the surface of the sample after electron beam illuminating one point for 20 minutes.

4.6.5. Summary of This Section

This section mainly discussed several practical issues regarding the EBSD mapping.

First, we showed there exists a best binning ratio for EBSD orientation mapping. Under-binning of the EBSD pattern is not enough to suppress the noise and Over-binning can lead to information lost.

Second, we implemented a large radius Gaussian filter using two different approaches: recursive filtering and through a Fourier transform. Both of the methods are reasonably fast and have the potential to be used in real time. Using a Gaussian filter has several advantages over an average filter. It also has the potential to replace the convolution mask.

Third, we also showed it is practical to save all of the diffraction patterns for the scanning process. This approach has some advantages.

Finally, we found that hydrocarbon contamination is a major limitation for EBSD mapping, especially when using a small scanning step size (comparable to beam size) and long pattern capture time. The hydrocarbon contamination can bring in artifacts and also can make orientation mapping meaningless. Besides, some suggestions are made or done on controlling or avoiding hydrocarbon contamination.

5. CONCLUSIONS AND FUTURE RESEARCH

5.1. OUTLINE

The aim of this research was to find a way to characterize single dislocations using the EBSD technique. In order to realize this purpose, we did a series of studies on the EBSD technique itself and the instrumentation. Conveniently, the conclusions made from this research can be divided into two related but different parts.

Part A is the results from the systematic study of the EBSD technique, as listed in section 5.2. We discussed the interaction volume of the EBSD technique, studied the characteristics of the Hough transform for Kikuchi bands, discussed the errors associated with the Hough algorithm and gave remedies to remove them. We also showed that there exists a best binning ratio for automatic indexing, and suggested Gaussian filter could be a possible way to circumvent the butterfly convolution.

Part B is mainly concerned with extending the applications of the EBSD technique, even though we failed in the aim of characterizing threading dislocations. The conclusions are listed in section 5.3. We designed an image processing routine, which can enable us to measure the shift of Kikuchi bands to sub-pixel accuracy and successfully applied it to map small details on the GaN/Sapphire structure. We compared this routine with another method, detecting the shift of zone axes in image space. The comparison shows our proposed method has advantages over the latter one. Based on this routine, we suggested a method to do "high precision" orientation mapping. We also did some research on using the intensity of the pixels from selected areas to do mapping. These maps can also show some details, which are missed by conventional methods. The specific conclusions are listed in section 5.2 and section 5.3.

Finally, some discussions are made on the future development of EBSD technique, including the further extension and application of this research and some personal opinions on what can be done to improve this technique.

5.2. CONCLUSIONS ON SYSTEMATIC STUDY OF EBSD

5.2.1. Monte-Carlo simulation

1. The standard way of using Monte-Carlo simulation tends to overestimate the size of the interaction volume and the spatial resolution of EBSD, since standard way on using Monte-Carlo simulation used the projection of the trajectories.
2. The interaction volume of EBSD has a strange shape. The BSEs form a wedge shaped region on the surface of the sample. The lower part has higher gradient than the upper part. The center of the wedge is away from the impinging point. If looking from side, the interaction volume has a triangle shape.

5.2.2. Hough Transform

1. The Hough transform of a Kikuchi band has certain peculiarities.
2. The standard Hough transform introduces artifacts.
3. We provided two methods to remove the artifacts.
   A. "Nearest to the line" method. This method is slightly slower than the standard Hough transform used in the OIM mapping, and can be used to replace it.
   B. "Weighting the points" method. This method is adopted to detect small shifts of the Kikuchi bands.

5.2.3. Binning ratio

There exists a best binning ratio for EBSD automatic indexing.

5.2.4. Gaussian Filter

1. A Gaussian filter can be implemented in real time to remove residual background.
2. A Gaussian filter has the potential to replace the convolution mask.

5.3. CONCLUSIONS ON MEASURING SMALL CHANGES OF ORIENTATION

5.3.1. Detect the shift of the Kikuchi bands and Zone Axes

1. We wrote programs, which enable us to detect the shift of a Kikuchi zone axis in image space and Kikuchi bands in Hough space, the cross correlation coefficient and phase correlation are used as criteria.
2. For normal working conditions of EBSD, detecting the shift of a zone axis in image space can be affected by a (0,0) peak. This peak is difficult to get rid of and it affects the accuracy of the peak detection.
3. We built an image processing routine to detect the shift of the Kikuchi bands in Hough space (revised Hough transform 1). This method can reach sub-pixel accuracy and it has advantages over the method of detecting the shift in image space.
4. The mapping function is available for the shift detection method.

5.3.2. Intensity Mapping and Shift Mapping

1. We introduced maps of mean, standard deviation and entropy to replace IQ (Image Quality) mapping. Those maps provide much richer information than conventional IQ mapping.
2. Mapping the shift of the Kikuchi bands was implemented
3. Direct mapping of the intensity information of selected Areas (like zone axes, Kikuchi bands) was also implemented

5.3.3. Application to GaN/Sapphire structure

1. Two Kinds of features were observed on the maps of the mean, standard deviation and entropy when studying the GaN/Sapphire structure: 1) Chevron shapes. 2) Point-like features. These features cannot be observed in Secondary Electron Imaging in conventional SEM and they are also not seen in conventional EBSD analysis.
2. The maps of the Kikuchi band shifting show that the orientation is not constant on the surface. The orientation difference among different regions is less than 0.2°-0.4°. The edges of the regions correspond to the chevron shapes in some cases.
3. Selected area mapping (using a special zone axis, Kikuchi bands) also shows there are some features on the sample.
4. Hydro-carbon contamination is the practical limitation of the EBSD mapping when going to high spatial resolution.
5. At the present stage, we do not have proof that our methods can detect single dislocations. The limiting reason could come from the relatively large beam size when used in the conventional EBSD system, since long working distance has to be used in most cases.

5.4. FUTURE RESEARCH

EBSD experienced rapid development in recent years. Its versatile usage has been widely accepted by materials scientists and engineers. However, most of the present research is focused on the application of this technique. There are still many questions, to which the answers are unknown or unclear to people, even for the basic physics related to this technique. These questions include (but are not limited to): the spatial resolution, the angular resolution, the information depth, and the energy range of the "information carrier". Still there isn't one quantitative model, which can solve these problems. Much experimental research tried to give answers to some of these questions. Unfortunately, most of their approaches are flawed.

On the other hand, since this technique is new, there are still a lot of things that should be done on the instrumentation and extending the applications of EBSD. Considering different user requirements, different applications targeting different users seems a good choice. We also would like to describe a new "unconventional EBSD system" as a complement to the conventional ones.

5.4.1. A "Dummy" EBSD system

The typical EBSD system can be divided into the collection system and the analysis software. The collection system captures and indexes the EBSD patterns in real time. For each EBSD pattern, it records the orientation information, IQ value, CI parameter and some other factors. The collection system needs to synchronize the operations of hardware, like camera, frame grabber, and even the EDS controls, to access the beam and stage control of the SEM and do some heavy calculation. Since the collection system needs to work fast, the time permitted for calculation is limited. As a result, the collection system can calculate only limited factors; much of the information is just thrown away. The analysis software analyzes the captured data from the collection software. In previous chapters, we proposed to (and did) collect all of the diffraction patterns and use them to the maximum. We are going to elaborate and extend this idea here.

We would like to transfer most of the calculation (Hough transform, convolution, indexing and something else) from the collection system to the analysis software. This "dummy" EBSD system still has a collection system and analysis software. However, the Data collection system can be very simple and the Data analysis software should be more complex than at present.

Since no calculation or very light calculation is needed on the collection software (except the compression process), with very little revision, the present collection system works well enough. It only needs to add one module to compress the raw EBSD patterns to one or several files and save it (them) to the hard drive. In fact, the collection system can be made remote controlled and even web-based.

Contrary to the collection software, the analysis software doesn't need to be fast, it needs to be accurate and convenient for users. Personally, I would like the interface of the analysis software look like that of Visual Studio. Each project is located inside one directory. All of the EBSD patterns are compressed into several to dozens of data files. Since the whole set of EBSD patterns are recorded, the Hough transform and indexing can be conveniently done offline. For each project, users can choose to generate all conventional EBSD maps and some other maps; all the methods proposed in this research can be conveniently implemented. In addition, whenever the user clicks on one pixel in the maps, the original EBSD pattern, the orientation, the index overlaid pattern, the Hough transform, and even the EDS spectrum will pop up. Users can use the naked eye to judge whether and when something is wrong.

If the index of a point is wrongly labeled, as often happens, users are able to change it. The analysis software should also expose some functions and allow users to use some script languages to do a little programming, in order to finish some batch work, like changing the index for some special grains, performing mappings using specially defined factors and testing new filters.

This "unconventional" EBSD instrument has many advantages over the traditional one. Firstly, users will save much precious SEM time, if they selected the wrong phase and not ideal indexing factors, since all of the factors can be readjusted. Even for the same scan set, these factors can also be different for different phases or grains. Secondly, suspected bad points on the orientation maps can be double-checked or re-adjusted. Users can even retrieve the original EBSD patterns to discriminate the reasons for the generation of bad points. Thirdly, users can extend the function of EBSD easily, thus the EBSD technique can be more flexible.

However, there are still some problems, which need careful consideration. First, for many applications at least, this approach is not practical at the present stage. Second, this approach involves large data transfer to and from the hard drive, usually at the level of

Giga bytes. The bottleneck of a personal computer is the relatively slow speed of input and output, as a result, reading and writing data needs considerable time (still it is far less than calculation time). So, a SCSI hard drive should be preferred to an IDE hard drive, however, the latter is more popular. Third, this approach needs a good compression algorithm, which is fast and effective. The large dataset can also bring some troubles to users, especially to those who don't copy and delete files in time. Finally, users need training to fully utilize this "unconventional" EBSD instrument, such as learning a "script" language, which could be different from manufacturer to manufacturer.

5.4.2. Some Other thoughts

- *Utilizing "Weighting the point" Hough transform.*

As mentioned in the previous chapters, the convolution process following the Hough transform has some shortcomings. It forced the Kikuchi bands to have a similar angular width. This fact doesn't affect the orientation mapping a lot, however, it has a larger impact on the accuracy of Phase Identification function, since the width of the Kikuchi band is inversely proportional to the d-spacing. Our research shows that the intensity distribution of Kikuchi bands in Hough space is relatively smooth, with less effect of noise. So, we suggested adding a "High Precision" Hough transform for Phase Identification, using our revised Hough transform. The width of the band can be measured to a high precision in the Hough space, if interpolation is used.

- *EBSD.VS. ECCI*

With appropriate settings, it is also worthwhile to compare the results from ECCI (electron channeling contrast imaging) with EBSD mapping.

- *Plastic Strain Mapping:*

IQ maps were expected to give qualitative descriptions of the strain level inside the materials. However, for polycrystalline samples, in most of the cases, the diffraction contrast between the grains dominated the image and makes the strain estimation very difficult and nearly impossible. Some other maps, like the first moment of the power spectrum of the Fourier transform [62], the second moment of the power spectrum of the Fourier transform, standard deviation, and entropy face the same problem as the IQ maps. Maps using factors characterizing the "sharpness" of several Kikuchi bands, which can be found in the EBSD patterns of several nearby grains, seems a solution to this problem.

- *Extending Present Research*

Even though we failed to image single dislocations in this research, there are still hopes that this method could work. Since the largest obstacle comes from hydro-carbon contamination. So, a high vacuum, high performance SEM is needed. More efficient CCD cameras, like the "Lens-on-chip" CCD camera could also be a good idea. Another alternative is using a Schottkey field emission SEM equipped with a FIB (focused ion beam). First, a normal EBSD scan can be performed quickly to find some interesting areas, then using the ion beam to remove the generated hydrocarbon layer on the surface, followed by a small step long pattern integration time scan. The hydrocarbon film deposited on the sample surface during the scan process can be removed by small dose of ion beam or oxygen gas blown through a gas inlet.

Some research can also be done on the combination and comparison of EBSD with SREM (Scanning Reflection Electron Microscopy).

In theory, the methods used in this research can also be done in real time. This could involve parallel programming.

Appendix 1. Hough Transform

Principle:

A straight line can be expressed by its polar form (Figure 2.10a and 2.10b): $\rho = x\cos\theta + y\sin\theta$, $\theta \in [0, \pi]$. The Hough space is then defined by a Cartesian coordinate system (θ, ρ). The intensity of any point in Hough space, $H(\theta i, \rho i)$ is the sum of the intensities along the line $\rho i = x\cos\theta i + y\sin\theta i$ in the image space. Each point in the image space contributes to points along a sinusoidal curve in Hough space. Psuedo code is shown below.

Standard Hough Transform:

```
//Step1. For each pixel in the image, calculate its ρ for each degree in the range of [0,180°)
  for( Theta =0; Theta<180; Theta++)
  for(i =0; i<ImageSizeX; i++)
   for(j=0; j<ImageSizeY; j++)
     RHO[Theta][i][j] = cos(Theta)*i + Sin(Theta)*j; //RHO[i][j][Theta] is a float number
          //The order in the dimension of the array is important to the calculation speed
//Step 2. Doing Hough Transform!
        for(i =0; i<ImageSizeX; I++)
             for(j=0; j<ImageSizeY; j++)
                  for( Theta =0; Theta<180; Theta++) { //Theta is an integer
                   Rho =(int) RHO[Theta][i][j]; // Rho is rounded from a float  to an integer
                   Hough[Theta][Rho] = Hough[Theta][Rho] + Image[j][i];  } // Errors !
```

Correction Method 1:

```
//Step 1. The same as Standard Hough Transform
//Step 2. Revised Form

for( Theta =0; Theta<180; Theta++)
{
        if(Theta>=45 && Theta<=135 )
        {
          for(i=0; i<ImageSizeX; i++)
          for(j=0; j<ImageSizeY; j++)
          {
                int Rho1 = (int) (RHO[Theta][i][j]+0.5);
                int Rho2 =(int) (RHO[i+1][j][Theta]+0.5) ;
                if(Rho1== Rho2)
                {
    ++i;  //For illustration only.  You can add your method here
                }
                Hough[Theta][Rho1] += Image[j][i-1];
          }
        if(Theta<45 ||(Theta>&&Theta<180))
        {
                //similar as above, but comparing columns instead of rows
        }
}

//Comment: Organizing data carefully so you can gain speed.  Our experiment shows if well
designed, the speed of this method is slightly slower than the standard method (around 30%-
40%).
```

Correction Method 2:

```
// Step 1. The same as Standard Hough transform

//Step 2. The Averaged Hough Transform
        for(i =0; i<ImageSizeX; i++)
        for(j=0; j<ImageSizeY; j++)
        for( Theta =0; Theta<180; Theta++) {
            Rho = (int) RHO[Theta][i][j] ;
           float temp1 = RHO[Theta][i][j] - Rho;
           float  temp2 = 1- temp1;
           Hough[Theta][Rho] += temp2*Image[j][i];
          Hough[Theta][Rho+1] += temp1*Image[j][i];
          HoughCoeff[Theta][Rho] += temp2;
                 /* Two-dimension  array HoughCoeff, float number */
          HoughCoeff[Theta][Rho+1]+= temp1;
        }

//Step 3. Normalization
        Hough[i][j] = Hough[i][j]/(HoughCoeff[i][j]+0.5);//in case divided by "0".
```

Appendix 2. Image Formats, Video Standards and Firewire

If you are not from a physics or electrical engineering department and you worked sometimes in the EBSD field, you could be confused and "cheated" by some terms and formats regarding to image and video standards. This is a brief introduction.

Image Formats:

BMP (Bitmap), TIF and JPEG are the most common files we met for EBSD patterns.

BMP (Bitmap) is the most basic image format for PC (Personal Computer). In most cases, for most application software run on a PC, all other still image formats are changed directly or indirectly to this format before it is displayed.

Generally speaking, there are two kinds of BMP files, device dependent and device independent bitmaps. Nearly all of the BMP files we used and met are device independent. For a device independent BMP file, its bit depth can be 2,4,8, 16, 24 and 32. The 16 bits BMP is also called high color, and the 24 bits and 32 bits BMP are sometimes called true color. 8 bits, 24 bits and 32bits BMP files are the most common bitmap files. For a grayness image, it can have at most 256 grayness scales ($=2^8$). However, most of the digital cameras claim an image depth more than 12. This means in most conditions, this is just a fib (the display on a PC is only 32 bits!). This also means, saving a grayness BMP file to 8 bits makes no difference from saving it to 24 bits and 32 bits BMP files, if the program you used is reasonably programmed. On the other hand, if software is well designed, changing a 32 bits grayness BMP file to 8 bits should not lead to information loss. However, in practice, this must be done very carefully, even Microsoft can make simple mistakes (You can check the Paint Program on your PC).

To make things worse, there are Windows BMP and OS2 BMP. Both of them have the same extension name; unfortunately, some application software can handle only one of them. BMP files can also be compressed or non-compressed.

Tif or Tiff (tagged image file format) is a popular digital image format. Tiff is designed to be a "superset" of all existing graphics or image formats. However, this design made Tiff very complex and reading, writing, and displaying of Tiff files are relatively slow. Tiff can be compressed or non-compressed, and its compression type can also be flexible. The most commonly used Tiff file is compressed using LZW method, which is a loss-less data compression type. A Tiff file can be extended to cover more than 8 bits grayness scale and some EBSD manufacture did so (maybe they gave up now). However, this extension cannot be recognized by most commercial image processing software and it doesn't make any difference on display. My personal experience is saving EBSD pattern to .Tif file doesn't save hard disk space comparing to .BMP (8 bits grayness scale). However, this could also means the EBSD manufactures didn't use compression.

JPG or JPEG. JPEG stands for Joint Photographic Experts Group. JPEG is designed for human vision. Since our eyes are not sensitive to high frequency signals, JPG file format is lossy. However, JPEG file can be extremely small which is convenient for using on Internet. The compression algorithm of the JPEG relies on Discrete Cosine Transform, which is closely related to Fourier transform. A new JPEG format, JPEG

2000, is based on a new compression method, the Discrete Wavelet Transform, which gave even higher compression ratio.

Do you know? Some image processing software is so considerate to let you choose the compression ratio.

Video Standard:

The hardware of an EBSD system includes a frame grabber, which captures video signals transferred from the camera. So, the operation of a frame grabber must be synchronized with that of camera and the video standard puts a limitation on your pattern quality and the number of patterns you can analyzed every second.

In the past, you are assumed to make a choice among NTSC, PAL and other formats (listed below). However, this is not true nowadays. With the rapid development of the digital technology, digital CCD camera and frame grabber manufactures developed new video standards, which fully utilize the fast data transfer speed provided by the PC and also allows more scanning lines per frame. Typical standard includes RS 422 and LVDS. Both of them allow pixel by pixel transfer and users don't need to worry about the effect of interlaced scan. As a result, you can capture more than 60 EBSD patterns every second.

Some Video Formats:

- Monochrome video standard:

  USA:

  RS-170: CCD array as an optical sensor. Reads out frames in two fields. Even frame for even numbered lines and odd frame for odd numbered lines. For "progressive" scan mode, the sensor reads out the entire frame. Other characteristics include:

  Composite signal (containing both timing and video signal), 1 volt video signal amplitude (-0.286, 0.714), 2:1 interlaced scan, 525 line, 30F/S and 4:3 aspect ratio.

  RS-330:

  RS-343: 675-1023 lines per frame.

  Europe:

  CCIR

- *Color Video standard:*

  NTSC (US): 525 lines, 60F/S, 2:1 interlaced system and YIQ color space.

  PAL (Europe): 625 lines, 50F/S, 2:1 interlaced system and YIQ color space. It is a modification of the NTSC.

  SECAM (France, Russia): 625 lines, 50F/S, 2:1 interlaced system and YIQ color space.

  *YIQ color space has advantage over RGB space over reduction of redundancy.

- *Nonstandard:*

  RS 422 and LVDS.

Computer Ports

At first, there were only a parallel port and two serial ports on a PC. Usually, a printer was connected to the PC through a parallel port and a keyboard was connected to the PC through a serial port.

With the rapid development of peripheral hardware, there was the USB (universal serial bus) port. USB ports are for the convenience of installation of some special hardware (you don't need to open the case of your computer). Some models of zip drive, CD burner and digital camera are connected to the PC through a USB port. USB port is a fast serial port.

With the wide usage of the digital cameras mostly, there is the so called ***Firewire*** Port. Like USB, it is also a serial port, however, it allows much faster data transfer speed than a USB port. Firewire Port is also named IEEE1394 port and iLink port (For Sony only. Large companies always show contempt on standard!).

FireWire is a cross-platform, high-speed serial data bus -- defined by IEEE Standard 1394-1995.

*IEEE1394A: 100 to 400 Mbps data transfer

*IEEE1394B: 800 to 3200 Mbps data transfer

Appendix 3. List of Programs Written for This Research, Revision Made on TSL's Data Collection Softwrae and Dan (.dan) Format

OIM(Data Collection System). For the convenience of programming, I made two different versions of this program, OIM3.exe and OIMLehigh.exe, revised them differently and added different functions to them.

OIMLehigh.exe is used to capture the whole set of EBSD patterns and do offline analysis. After my revision, the scanning size along X and Y directions can be different, and the scanning direction can also be reversed. The captured patterns are saved to hard drive into 8 bit Bitmap files (BMP); all of the patterns are named sequentially according to the place they are captured. For example, the file at Xth column and Yth row is named as MyPatternaXbY.bmp.

For OIM3.exe, I made several changes and added several functions.

1) Revised Hough transform (form 1 and form 2).
2) Implemented methods to calculate the shift of Kikuchi bands to sub-pixel using cross correlation coefficient, which can be chosen to be calculated directly or through a Fourier transform.
3) Mapping the shift of Kikuchi bands for a whole batch of EBSD patterns (generate .Dan file).

4) Mapping the intensity information (standard deviation and mean) for certain Kikuchi bands (generate .Dan file).

DataAnalyzer: This SDI program is used to display and tweak the .Dan files and save them to bitmap files. Since the standard image formats lack flexibility and lose information for mapping, I designed a special mapping format (.dan) for this research only; all of the offline mapping processes written for this research generated .Dan (DataAnlayze) files. The structure of .Dan is very simple, the first 4 bytes (integer) are the total columns of the map and the next 4 bytes record the total rows of the corresponding map. The following bytes of this file record the value of each pixel, row by row. Each pixel is described by 4 bytes (float).

GaussianBlur: This MDI program implemented two ways to do large radius Gaussian blur and de-blur function (recursive filtering and through a Fourier transform). It also supports high pass filtering. The De-blur function is equivalent to blurring the original pattern and then subtracting the blurred pattern from original one.

GaussianMapping: This Dialog based program can do large radius Gaussian blur and deblur function for batches of EBSD patterns that are saved in one directory. The user can choose to use recursive filtering or through a Fourier transform.

DataMapping: This Dialog based program maps the mean, standard deviation, entropy of the selected area in the EBSD pattern (usually around a zone axis) or the whole pattern for the batch of captured EBSD pattern.

FFTMapping: This Dialog based program maps the first moment and second moment of the power spectrum of the selected area in the EBSD pattern (usually around a zone axis) or the whole pattern for the batch of captured EBSD patterns.

ShiftDetector: This MDI based program can detect the shift of a chosen area in the target EBSD pattern against the same area in a reference pattern. The cross correlation coefficient and the phase correlation can be chosen as criteria. Users can choose to calculate the cross correlation coefficient directly or through a Fourier transform. Using OpenGL, the calculation results can be displayed in 3d.

SurfaceMonitor and DataDisplay: These two programs work together. The former one is a special Monte Carlo simulation program. This program calculates the last position of the BSEs the moment they left the sample surface. The users can choose tilting angle, cutoff energy and the numbers of BSEs you want to detect. This program also allows the user to record the last positions of those electrons which experienced exactly one scattering event.

The latter one is used to display the calculated data generated by the former one.

In fact, I should put these two programs together. In order to save programming time, I used this ugly solution. Anyway, I am not a professional programmer.

PCAnalyzer: This is an "explorer style" program. This program does a Principle component analysis for some EBSD patterns (I gave up this idea later, similar programs including a Wavelet analysis program).

SpeViewer: Noran's Phase ID system had used .spe file format. This is a special format, which can support 32 bits float and integer (32 bits) pixel value. In order to fully utilize the contained information, I wrote several programs to view, calculate, and format transformation for this file format. However, Noran later changed the software (A total change without supporting the old format!) and this program became useless.

Some other programs, which are not directly related to this topic, are not covered.

References

1). P.M. Mooney (1996) Strain relaxation and dislocations in SiGe/Si structures

Materials Science and Engineering, ***R17****, 105-146*

2). http://www.sp.phy.cam.ac.uk/~dp109/strain.html

3). Julia W.P. Hsu(2001) Near-field scanning optical microscopy studies of electronic and photonic materials and devices

Materials Science and Engineering, ***33****, P1-50*

4). J. I. Goldstein, D.E. Newbury, P. Echlin, D.C. Joy, CE. Fiori, and E.Lifshin

Scanning Electron Microscopy and X-Ray Microanalysis, 2nd Edition

Plenum Press, New York, 1992

5). D.C. Joy, D.E. Newbury, and D.L.Davidson(1992) Review: Electron Channeling Patterns in the Scanning Electron Microscope

Journal of Applied Physics, ***53****, No.8, P81-118*

6). P.Morin, M.Pitaval, E.Vicario, and G.Fontaine (1979) Scanning Electron Microscope Observation of Single Defects in Solid Crystalline Materials

Scanning, ***2****, P217-224*

7). J.T. Czernuszka, N.J.Long and P.B. Hirsh (1990) Imaging of dislocations using backscattered electrons in Scanning electron microscope
*Phil. Mag. Lett, **63**, P227-232*

8). B.C. Ng, B.A.Simikin, M.A. Crimp (1997) Electron Channeling Contrast Imaging of Dislocation Structures in Deformed Stoichiometric NiAl
*Materials Science and Engineering A, **239-240**, P150-156*

9). D.J.Dingley, The development of Automated Diffraction Scanning and Transmission Electron Microscopy
Electron Backscatter Diffraction in Materials Science
Editors: Adam J.Schwartz, Mukul Kuzmar, and Brent L. Adams
Klumer Academic/Plenum Publishers, New York, *2000*

10). J.A.Eades(1999) Choosing an Electron backscattering Pattern(EBSP) system.
*Microscopy and Microanalysis, **5**, (Sppl 2), P250-251*

11). http://www.hkltechnology.com

12).www.tsl-oim.com

13). D.J.Dingley, K.Z.Baba-Kishi, V.Randle Atlas of Backscattering Kikuchi Diffraction Patterns

Institutes of Physics Publishing, Bristol, U.K, 1995

14). J.R. Michael, and J.A. Eades (2000) Use of reciprocal lattice layer spacing in electron backscatter diffraction pattern analysis

*Ultramicroscopy, **81**, P 67-81*

15). R.A. Schwarzer (1997) Advances in Crystal Orientation Mapping with the SEM and TEM

*Ultramicroscopy, **67**, P19-24*

16). F.J.Humphreys, Y.Huang, I.Brough, and C. Harris (1999) Electron backscatter diffraction of grain and subgrain structures – resolution considerations

*Journal of Microscopy, **195**, Pt3, P212-216*

17). D.J. Dingley, V.Randle(1992) Review: Microtexture determination by electron back-scatter diffraction

*Journal of Materials Science, **27**, P4545-4566*

18). F.Cosandey, Orientation determination of epitaxial Au Particles on TiO_2 by Electron Backscatter Diffraction.

www.leo-em.co.uk

19). T. C.Isabell, V.P.Dravid (1997) Resolution and sensitivity of electron backscattered diffraction in a cold field emission gun SEM

*Ultramicroscopy, **67**, P59-68*

20). S.X.Ren, E.A.Kenik, K.B.Alexander, and A.Goyal(1998), Exploring Spatial Resolution in Electron back-Scattered Diffraction Experiments via Monte Carlo Simulation

*Microscopy and Microanalysis, **4**, P15-22*

21). O.C.Wells (1999) Comparison of different models for the generation of electron backscattering patterns in the Scanning Electron Microscope

*Scanning, **21**, P368-371*

22). D.P.Field (1997) Recent advances in the application of Orientation Imaging

*Ultramicroscopy, **67**,P1-9*

23). M.Mita, T,Nokuo, T.Yanagihara, M.Iwatsuki, and K.Date (2001) The latest Analytical Method and Future Potential with In-lens Thermal FEG

*JEOL News, **36**, NO.1, P32-35*

24). Opal Reference

Oxford Instrument Company

25). V. Randle(1996) Electron Backscattering Diffraction

http://www.oxinst.com/mag/education/ebsd.htm, 1996 (Oxford Instruments)

26). Baba-Kishi KZ and Dingley D J (1989) Backscatter Kikuchi diffraction in the SEM for identification of crystallographic point groups.

*Scanning, **11**, P305-312*

27). Gignac et al(2002) A Comparison of Grain Size Measurements in Al-Cu Thin Films: Imaging Vs. Diffraction Techniques.

Microscopy Today, Nov., 2002, P5-8

28). A.J. Wilkinson (1996) Measurement of elastic strains and small lattice rotation using electron back scatter diffraction

*Ultramicroscopy, **62**, P 237-247*

29). K.Z. Troost, P.van der Sluis, and D.J. Gravesteijn Microscale(1993) Elastic strain determination by backscatter Kikuchi difftaction in the scanning electron microscope

*Applied Physics Letter, **62(10)**, P1110-1112*

30). A.J. Wilkinson (2000) Advances in SEM-based diffraction studies of defects and strains in semiconductors

*Journal of Electron Microscopy, **49(2)**, P299-311*

31). E.M.Lehockey, Y.Lin, and O.E. Lepik, Mapping Residual Plastic Strain in Materials Using Electron Backscatter Diffraction

Electron Backscatter Diffraction in Materials Science

Editors: Adam J.Schwartz, Mukul Kuzmar, and Brent L. Adams

Klumer Academic/Plenum Publishers, New York, *2000*

32). OIM (Orientation Imaging Microscope) manual

TSL company.

33).N.C.Krieger Lassen, D.Juul Jensen and K.Conradsen (1992) Image Processing Procedures for analysis of electron Back scattering Patterns

*Scanning Microscopy, **6(1)**, P115-121*

34). P.V.C. Hough (1962) Method and Means for recognizing complex patterns

US Patent 3,069,654

35) M. Sonka, V. Hlavac, R. Boyle. *Image Processing, Analysis, and Machine Vision, Second Edition.*

PWS publishing, Boston, 1999

36). S.I. Wright, B.L.Adams,(1992) Automatic Analysis of Electron Backscattering Patterns

*Met. Trans. A, **23**, P759-767*

37). N.C.Krieger Lassen (1998) Automatic high-Precision measurements of the location and width of Kikuchi bands in electron backscatter diffraction patterns

*Journal of Microscopy, **190**, pt 3, PP375-391*

38). Valerie Randle, Theoretical Framework for Electron Backscatter Diffraction, Electron Backscatter Diffraction in Materials Science

Editors: Adam J.Schwartz, Mukul Kumar and Brent L.Adams.

Kluwer Academic/Plenum Publishers, New York, 2000.

39). Stuart Wright, Fundamentals of Automated EBSD,

Electron Backscatter Diffraction in Materials Science, P51-P61.

Editors: Adam J.Schwartz, Mukul Kumar and Brent L.Adams

Kluwer Academic/Plenum Publishers, New York, 2000.

40). OIM Data Analysis Manual

TSL Company

41). F.J.Humphteys, P.S.Bate abd P.J.Hurley, Orientation averaging of electron backscattered diffraction data.
*Journal of Microscopy, **201** ,pt, P50-58.*

42). L. Reimer, U. Heilers and G. Saliger (1986) Kikuchi Band Contrast in Diffraction Patterns Recorded by Transmitted and Backscattered Electrons
*Scanning, **8**, P101-118*

43). D.G. Coates (1967) Kikuchi-like reflection patterns obtained with the scanning electron microscope.
*Phil. Mag, **16**, P1179-1184*

44). G.R.Booker, A.M.B. Shaw, M.J. Whelan, and P.B. Hirsch(1967) Some comments on the interpretation of the Kikuchi-like patterns observed by scanning electron Microscopy.
*Phil. Mag,**16**, P1185-1191*

45). A.J.Wilkinson and P.B.Hirsh (1995) The effects of surface stress relaxation on electron channeling contrast images of dislocations
*Phil. Mag. A, **72**, P81-103*

46). E.M.Schulson (1977) Review: Electron channeling patterns in Scanning Electron Microscopy

*Journal of Materials Science, **12**, P1071-1087*

47). K.Castleman(1996) *Digital Image Processing*

Prentice Hall Press, New York

48). http://www.ee.surrey.ac.uk/Personal/L.Hill/pc.html

49). H.Foroosh, J.Zerubia and M.Berthord, Extension of Phase Correlation to Sub-Pixel Resolution

IEEE TRANSACTIONS ON IMAGE PROCESSING, EDICS:2-ANAL, 2-MOTD 1

50). A.Averbuch, Y.Keller. A unified approach to FFT based image registration??

IEEE TRANSACTIONS ON IMAGE PROCESSING, EDICS:2-ANAL, 2-MOTD 1

51). S.Kraemer and J.Mayer(1999) Using the Hough transform for HOLZ line identification in Convergent Beam Electron Diffraction

*Journal of Microscopy, **194**, pt 1, P 2-11*

52). Phase ID Manual

Thermo Noran Company

53). David C. Joy. Monte-Carlo Modeling for Electron Microscopy and Microanalysis Oxford University Press, New York, 1995

54). **Casino 2.0** " A Monte-Carlo" Simulation program
Raynald Gauvin, Universite de Sherbrooke
http://www.gel.usherb.ca/casio

55). Oliver C.Wells, Scanning Electron Microscopy.
McGraw-Hill Book Company, New York

56). George Marsaglia and Arif Zaman (1987) Toward a Universal Random Generator, Florida State University Report: FSU-SCRI-87-50.

57). www.fftw.org

58). Akira Sakai, Haruo Sunakawa, Akitaka Kimura and Akira Usui (2000) Dislocation propagation in GaN films formed by epitaxial lateral overgrowth.
*Journal of Electron Microscopy, **49**(2)*, P323-330

59). Ludwig Reimer. Transmission Electron Microscopy, 4th edition, Springer-Verlag Press, Berlin, 1997

60). Jeff Drucker, Mohan Krishnamurthy and Gary Hembree(1991) Biased Secondary electron imaging of monatomic surface steps on vicinal Si(100) in a UHV STEM.
*Ultramicroscopy, **35**, P323-328*

61). J.Liu and J.M.Cowley (1993) Scanning reflection electron microscopy and associated techniques for surface studies.
*Ultramicroscopy, **48**, P381-416*

62). A.J.Wilkinson and D.J.Dingley (1991) Quantitative Deformation Studies using Electron Back Scatter Patterns,
*Acta Metallurgica et Materilia, **39**, P3047-3055*

In my own program, I used or revised following open codes:

63). David J. Kruglinski's ***CDib class***
Programming Microsoft Visual C++ Fifth Edition, 1998, Microsoft Press

64). Mihai Filimon ***CfolderDialog***
http://www.codeguru.com/dialog/folder_dialog.shtml

65). B.Manivannan. ***Real Time 2D Graph*** Program http://codeguru.earthweb.com/bitmap/Graph.html

66). J.R.Parker's source code on ***Foruier Transform***

Algorithms for Image Processing and Computer Vision, 1996, JohnWiley & Sons, Inc

67). FFTW library, Open Source free ware

www.fftw.org

68). Keith Rule's source code on CMemDC

www.codeguru.com

69). Some suggestions and code snippets from www.codeguru.com

70). Some suggestions and code snippets from www.codeproject.com

Vita

Xiaodong Tao was born to Mr. Yuelu Tao and Mrs. Guifen Zhang on April 30, 1972, in Rushan, Shandong Province, P.R.China. In the fall of 1989, he entered Xi'an Jiaotong University and graduated with high honors in July, 1993 with a bachelor of engineering degree in Materials Science and Engineering department. At the same year, he entered Shanghai Jiaotong University and graduated with high honors in Feb, 1996 with a master of engineering degree in Materials Science and Engineering department.

He then worked for Volkswagen Automotive company (Shanghai, P.R.China) until June, 1998, two months before he came to United States and became a graduate student of Lehigh University.